University of Nevada, Reno

In situ and Remote Sensing Characterization of California Wildfires and Nevada Desert Dust

A dissertation submitted in partial fulfillment of
the requirements for the degree of Doctor of
Philosophy in Physics

By

Dambar S. Air

William P. Arnott, Ph.D./Dissertation Advisor

May, 2014

THE GRADUATE SCHOOL

We recommend that the dissertation
prepared under our supervision by

DAMBAR S AIR

entitled

In situ and Remote Sensing Characterization of California Wildfires and Nevada Desert Dust

be accepted in partial fulfillment of the
requirements for the degree of

DOCTOR OF PHILOSOPHY

William P. Arnott, Ph. D., Advisor

James C Barnard, Ph. D., Committee Member

Yasuhiko Sentoku Ph. D., Committee Member

Bernhard Bach Ph. D., Committee Member

Sean Casey Ph. D., Graduate School Representative

Marsha H. Read, Ph. D., Dean, Graduate School

May, 2014

Abstract

Atmospheric aerosols exert significant influence on the climate and cause problems in human health and ecosystem. This dissertation reports aerosol physical and optical properties obtained from ground based remote sensing instruments, the Multifilter Rotating Shadowband Radiometer (MFRSR) and Cimel sun photometer, and in-situ measurements from photoacoustic (PA) instruments. The measurements were performed during California Rim fire of 2013, desert storm of 2013, and clear sky days. A 2-stream radiation transfer model and Mie theory were used to calculate the retrieved values of solar irradiances and aerosol optical properties. The ground based measurements were also compared with the satellite (Terra MODIS, Aqua MODIS and Deep Blue) measurements.

The aerosol optical properties retrieved with the MFRSR show excellent agreement with those obtained with a co-located Cimel sun photometer. However, the comparison with the satellite measurements indicates significant departure from the ground based measurements. The values of the aerosol optical depth (*AOD*) and Ångström exponent (*AE*) during the Rim fire event remained higher than clear sky days due to the presence of smoke particles in the atmosphere. However, the values of *AOD* during the dust storm were higher but the *AE* become lower than the clear sky days due to the presence of large particles in the atmosphere. The concentration of the fine mode (diameter less than 1 µm) dominates over the coarse mode (diameter greater than 1 µm) particles during the Rim fire, while coarse particles were more prevalent during dust storm.

Back trajectory analysis during the Rim fire indicated that the southerly wind brought the plumes of smoke which originated at California Rim fire toward Reno. Similarly,

the back trajectory analysis during the dust storm suggested that the dust was generated from the Humboldt sink and traveled towards Reno.

The single scattering albedo (*SSA*) was found to decrease with wavelength due to the absorption of solar radiation by the small black carbon particles present in the wild fire smoke. However, the *SSA* during the dust storm increases with wavelengths, which is due to significantly lower absorption of the dust aerosols at longer wavelengths (675-1020 nm) compared to biomass burning aerosols. It was interesting to note that the *SSA* values from in situ photoacoustic measurements and from the MFRSR retrievals were of very similar values during the Rim fire, suggesting that the smoke was well mixed in the atmospheric boundary layer. These novel measurements are reported here for the first time.

It was found that the radiative forcing at the top of the atmosphere (*TOA*) varied between $-38\ \mathrm{W/m^2}$ to $-65\ \mathrm{W/m^2}$ from MFRSR and Cimel during the Rim fire, suggesting a massive cooling effect due to scattering of solar radiation by the high aerosol loading. By comparison, the radiative forcing at the *TOA* ranged between $-0.5\ \mathrm{W/m^2}$ to $-1.8\ \mathrm{W/m^2}$ during clear-sky days.

Acknowledgements

I would like to thank my principal advisor, Dr. William P. Arnott for his wise guidance, patience, and endless encouragement throughout my study. I would never have been success to finish my dissertation without his scientific advice and insightful suggestions. I also extend my utmost thanks to my co-advisor, Dr. James C Barnard for his continuous guidance during the instrument setup, data analysis and dissertation writing. Thank you, Dr. James C Barnard for providing me your guidance and valuable time. A special thanks to my other committee members, Dr. Yasuhiko Sentoku, Dr. Bernhard Bach, and Dr. Sean Casey, for solidifying this work through their advice and assistance.

My sincere thanks also goes to department of Physics, for offering me the Teaching Assistantship during my Ph.D. study and research. My special thanks go to Dr. Madhu Gyawali, for his help in photoacoustic data analysis and writing my dissertation. I would like to extend thanks to all of my friends at UNR for providing support and friendship that I needed.

Lastly, I want to acknowledge my dad, mom, brothers, sisters and other family members for their constant encouragement and love. I would like to thank my wonderful wife Sujata. She always encouraging me up and stood through the good and bad times. Thank you for your love, patience and support.

Table of Contents

Abstract……………………………………………………………..…………………**i**

Acknowledgements……………………………………………………………………**iii**

Table of Contents……………………………………………………………………**iv**

List of Tables……………………………………………………………………**vii**

List of Figures……………………………………………………………………**viii**

Chapter 1 Introduction.. 1

1.1 Atmospheric Aerosol.. 1

1.2 Effects of the Atmospheric Aerosol.. 1

1.2.1 Effects on Climate 1

1.2.2 Effects on Human Health 3

1.3 Description of the Study 3

1.4 Outline of Dissertation... 6

1.5 Reference of Chapter 1 7

Chapter 2 Instrument Description 9

2.1 Multi-Filter Rotating Shadow-band Radiometer (MFRSRS) 9

2.1.1 Instrument Description and Operation 9

2.1.2 Dark Offset Correction……………………………………………………12

2.1.3 Cosine Response Correction……………………………………...…………13

2.1.4 Langley Regression Retrieval Algorithm……………………………… ………17

2.2 Cimel Sun Photometer…………………………………………………… …..……24

2.2.1 Instrumentation and Data Collection…………………………………………24

2.2.2 Cimel Data Processing and Products………………………………..……………27

2.3 Photoacoustic Instruments and Operation……………………………………..33

2.4 MODIS Satellite Measurement……………………………………………….....39

2.5 References for Chapter 2…………………………………………………………44

Chapter 3 Aerosol Optical and Physical Properties Retrieval and Radiative forcing…47

3.1 Introduction (Aerosol Size Distributions, Single Scattering Albedo and Asymmetry Parameter)…………………………………………………………………...47

3.2 MFRSR size distribution retrieval……………………………………………..49

3.3 MFRSR Single Scattering Albedo (*SSA*) and Asymmetry Parameter (g) retrieval…...53
3.4 Two Stream Radiative Transfer Model……………………………………………….….55
3.5 Direct Aerosol Radiative Forcing……………………………………………………..59
3.6 References of Chapter 3……………………………………………………………….61

Chapter 4 Aerosol Optical Depth (*AOD*), Ångström Exponent (*AE*) and Volume Size Distribution Case Studies……………………………………………………………………. 63

4.1 Introduction……………………………………………………………………………63
4.2 California Rim Fire on August - September, 2013 ……………………...…………... 64
4.2.1 Aerosol Optical Depth (*AOD*) and Ångström Exponent (*AE*) …………………... 66
4.2.2 Aerosol Volume Size Distribution ……………………………………………… 75
4.2.3 Back Trajectories Analysis ……………………………………………………….77
4.3 Dust Storm on 24 April, 2013 in Reno ……………………………………………….80
4.3.1 Aerosol Optical Depth and Ångström Exponent ………………………………….81
4.3.2 Aerosol Volume Size Distribution ………………………………………………..86
4.3.3 Back Trajectories Analysis ……………………………………………………….87
4.4 Clear Sky Days ………………………………………………………………………..90
4.4.1 Aerosol Optical Depth and Ångström Exponent ……………………...…….….90
4.4.2 Aerosol Volume Size Distribution ……………………………………………… 94
4.5 References for Chapter 4 …………………………………………………………….. 96

Chapter 5 Single Scattering Albedo (*SSA*), Asymmetry Parameter (*ASY*) and Radiative Forcing Case Studies ……………………………………………………………………… 98

5.1 Introduction ………………………………………………………………………….. 98
5.2 California Rim Fire, August-September 2013 ………………………………………. 99
5.2.1 Solar Irradiance Measurements ………………………………………………….. 99
5.2.2 Single Scattering albedo (*SSA*) …………………………………………………. 103
5.2.3 *SSA* Comparison between Photoacoustic (PA) and MFRSR measurements ……105
5.2.4 Asymmetry parameter and imaginary part of refractive index ………………….107
5.3 Dust Storm on April 24, 2013 in Reno …………………………………………….. 112
5.3.1 Solar Irradiance Measurements ………………………………………………… 112
5.3.2 Single Scattering albedo (*SSA*) ……………………………………………….… 114
5.3.3 Asymmetry parameter and imaginary part of refractive index ………………… 115

5.4 Clear Sky Days in Reno ………………………………………………………………. 117
  5.4.1 Solar Irradiance Measurements ………………………………………………… 117
  5.4.2 Single Scattering albedo (*SSA*) ………………………………………………. 112
  5.4.3 Asymmetry parameter and imaginary part of refractive index ………………… 123
5.5 Aerosol Radiative Forcing Comparison …………………………………………. 125
5.6 References for Chapter 5 ……………………………………………………………… 128
Chapter 6 Summary, Conclusion and Future Work ………………………………….. 130
6.1 Summary and Conclusion …………………………………………………………….. 130
6.2 Future Work ……………………………………………………………………………134
6.3 References of Chapter 6 ………………………………………………………………. 135

List of Tables:

Table 2.1 Ozone absorption coefficient for different wavelengths (from Koontz et al. 2013)………………………………………………………………………….…………….. 21

Table 4.1 MFRSR (673 nm), Cimel (673), and Terra MODIS dark target retrieval (660 nm) AODs and AEs for two cases (MFRSR and Cimel) during some selected days of the Rim fire 2013 ………………………………………………………………………...……………. 69

Table 4.2 MFRSR (673 nm), Cimel (673), Aqua MODIS dark-target retrieval algorithm (660 nm) and Deep Blue retrieval algorithm AODs (660 nm) during the selected days of the Rim fire 2013. ……………………………………………………………………………… 70

Table 4.3 MFRSR and Cimel average, (standard deviation in parentheses) of AOD at 673 nm wavelength and Terra MODIS dark-target, Aqua MODIS dark-target and Deep Blue retrieved AOD at 660 nm. ……………………………………………………………..……. 91

Table 5.1 Maximum diffuse, normal direct and total irradiances at 500 nm using MFRSR observed values during 12 selected days of Rim fire 2013. ……………………………… 102

Table 5.2 Maximum diffuse, normal direct and total irradiances at 500 nm using MFRSR observed values during 12 selected clear sky days. ………………………………………. 119

List of Figures

Figure 2.1 Basic geometry of a MFRSR (Hodges and Michalsky, 2011)……… 9

Figure 2.2 (a) The MFRSR in home position (nadir position), (b) First side measurement (fsb) at 9^{o} off the sun blocking direction, (c) Middle measurement with the sun blocked, (d) Second side measurement (ssb) at 9^{0} off the sun blocking direction (Muguel Bustamante, 2010). ……………………………………………………………………….………………10

Figure 2.3 MFRSR Spectral Band filters; at center is the silicon with a range of 415-940 nm (from http://uvb.nrel.colostate.edu/UVB/ins_vismfrsr.jsf). ……………….……………11

Figure 2.4 Example of daily solar plots from University of Nevada Reno site for February 15, 2013 using data from all channels……………………………………………………….. 16

Figure 2.5 Basic ideas about the solar zenith angle and airmass… 17

Figure 2.6 The natural logarithm of direct irradiance vs. airmass.…………………………..19

Figure 2.7 Time series of the V_0s (dots) from the UNR MFRSR for wavelengths 415, 500, 615, 673 and 870 nm. The daily corrected $V_{0,f}$ values are obtained by a smooth curve fit to these data for each wavelength. These smooth curves are shown by the solid lines. ………20

Figure 2.8 The top panel shows a time series of the AOD for five wavelengths and the lower panel displays the Ångström exponent using 500 nm and 870 nm channels. ………..……. 23

Figure 2.9 The CE 318 automatic sun tracking photometer has been designed and realized to be a very accurate sun photometer with all the qualities of a field instrument (http://fsf.nerc.ac.uk/instruments/cimel.shtml). …………………………………………. 25

Figure 2.10 Representations of the (a) Direct, (b) Almucantar and (c) Principal plane measurements. Almucantar and principal plane are done only at 440, 675, 870 and 1020 nm channels. Direct measurement is done at all wave lengths: 340, 380, 440, 500, 670, 870, 940, 500, 675, 870, 940, 1020, and 1640 nm (Muguel Bustamante, 2010). ……….……………… 26

Figure 2.11 Variation of the AOD (top panel); and size (volume) distribution (lower panel) from UNR Cimel for August 3, 2013. ……………………………………...……………. 31

Figure 2.12 Spectral variation of the single scattering albedo (top panel); and asymmetry parameter (lower panel) from UNR Cimel for August 3, 2013. ……………...……………. 32

Figure 2.13 Schematic of 532 nm wavelength photoacoustic instrument (K. A. Lewis 2007). ………………………………………………………………………………………. 33

Figure 2.14 Schematic of the standing wave with high-pressure antinodes exist at microphone, piezoelectric transducer and central cavity locations (K. A. Lewis 2007). ….. 34

Figure 2.15 Schematic of duel-wavelength photoacoustic instrument (K. A. Lewis 2007)…35

Figure 2.16 Time series of the absorption coefficient during the Rim Fire on August 23, 2013 using the photoacoustic instrument. ………………………………………………………37

Figure 2.17 Scattering coefficient for the same day at in Fig. 2.16. August 23, 2013 using photoacoustic instruments. ………………………………………………………………. 37

Figure 2.18 Time series of the SSA for August 23, 2013 using photoacoustic instrument. .. 38

Figure 2.19 Terra MODIS derived aerosol optical thickness at 550 nm of the Reno land on August 23, 2013 near 10:30 am local time. ……………………………………………….. 42

Figure 2.20 Aqua MODIS derived aerosol optical thickness at 550 nm of the Reno land on August 23, 2013 near 1:30 pm local time. ………………………………………………… 42

Figure 2.21 Deep Blue AOD at 550 nm of the Reno land on August 23, 2013 near 1:30 pm local time.……………………………………………………………………………... 43

Figure 3.1 Aerosol distributions over the height of the atmosphere. ……………………… 50

Figure 3.2 Illustration of volume distributions for a typical urban model aerosol (Seinfeld and Pandis 1998). ………………………………………………………………………….. 52

Figure 3.3 Schematics for the estimation of the single scattering albedo and asymmetry parameter (modified from Chelsea A. Corr and Science 2008). …………………………… 54

Figure 4.1 Map of the Rim fire: where the red line was the perimeter at 8 p.m., September 1, 2013. (http://wildfiretoday.com/2013/08/21/california-rim-fire-west-of-yosemite-np/).........64

Figure 4.2 NASA satellite image of the smoke from the Rim fire, spreading over Lake Tahoe, Reno, and beyond (http://aarondames.squarespace.com/nature/?currentPage=2). ………… 65

Figure 4.3 Time series comparison of MFRSR and Cimel aerosol optical depth for August 23, 2013 at UNR ……………………………………………………………………………… 67

Figure 4.4 Time series comparison of MFRSR aerosol optical depth for August 27, 2013 at UNR …………………………………………………………….……………………...67

Figure 4.5 Comparison of MFRSR and Cimel Ångström Exponent On August 23, 2013 ……………………………………………………………….…………………… 68

Figure 4.6 Comparison of MFRSR, Cimel, Terra MODIS dark-target, Aqua MODIS dark-target and Deep Blue retrieval AODs for August 23, 2013 at UNR. ………………………..71

Figure 4.7 Comparison of MFRSR, Cimel and Terra MODIS dark-target AODs for August 23, 2013 at 11:30 AM. ………………………………………………………………………72

Figure 4.8 Comparison of MFRSR and Cimel aerosol optical depth for 500 nm on August 23, 2013 at UNR ………………………………………...…………………………... 73

Figure 4.9 Comparison of MFRSR, Cimel and Terra MODIS dark-target AODs during the rim fire, August-September, 2013. ………………………………………………………73

Figure 4.10 Comparison of MFRSR, Cimel and Aqua MODIS dark-target AODs during the Rim fire, August-September, 2013. ………………………………………………………74

Figure 4.11 Comparison of MFRSR and Cimel aerosol optical depth for 500nm and 870 nm on August 2013. …………………………….……………………………………74

Figure 4.12 Comparison of MFRSR and Cimel aerosol optical depth for 500nm on August, 2013 at UNR. …………………………….…………………………………..... 75

Figure 4.13 (Top) Aerosol size distribution comparison derived from MFRSR and Cimel, and (bottom) the spectrally dependent AOD for selected cases derived from the MFRSR data and Mie calculation by using the derived aerosol size distribution and refractive index for August 23, 2013. …………………………..……………………………........76

Figure 4.14 48-hours back trajectory from NOAA- HYSPLIT on August 23, 2013 to Reno during the Rim fire. ……………………………………………………………… 78

Figure 4.15 48-hours back trajectory from NOAA- HYSPLIT on August 27, 2013 to Reno during the Rim fire. ……………………………………………………………… 79

Figure 4.16 Scattering of solar light radiation due to a dust storm on April 24, 2013 at UNR at local times 5:52 pm and 6:24 pm………………………………………………… 80

Figure 4.17 Time series of aerosol optical depth and Ångström Exponent for April 24, 2013 at UNR during the dust storm. …………………………………………………... 82

Figure 4.18 Time series comparison of MFRSR and Cimel aerosol optical depth for April 24, 2013 at UNR during the dust storm. ……………………………..…………………… 83

Figure 4.19 Comparison of MFRSR, Cimel and Terra MODIS dark-target AODs during the dust storm for April 24, 2013 at 12:55 PM. ……………………………………………... 85

Figure 4.20 Comparison of MFRSR, Cimel, Aqua MODIS dark target and aerosol and Deep Blue retrieval AODs during the dust storm for April 24, 2013 at 1:40 PM. ……………..…… 85

Figure 4.21 Aerosol size distributions during the dust storm using MFRSR for April 24, 2013. ………………………………………………………………………………….……….. 86

Figure 4.22 Comparison of measured and model aerosol optical depth from size distribution retrieval for April 24, 2013. …………………………………………………………….... 87

Figure 4.23 48-hours back trajectory from NOAA- HYSPLIT on April 24 (20:00 UTC), 2013 to Reno during the dust storm. …………………………………………………….. 88

Figure 4.24 48-hours back trajectory from NOAA- HYSPLIT on April 24 (22:00 UTC), 2013 to Reno during the dust storm. …………………………………….…………….… 89

Figure 4.25 Time series comparison of MFRSR and Cimel aerosol optical depth for August 1, 2013 at UNR during the clear sky at 500 nm and 673 nm channels. ……………………. 92

Figure 4.26 Time series comparison of MFRSR and Cimel aerosol optical depth for 2nd August and October 15, 2013 at UNR during the clear sky at 500 nm channel ..………………………………………………………………………….…………...92

Figure 4.27 Comparison of MFRSR, Cimel and Terra MODIS dark target retrieved aerosol optical depths for August 2, 2013 at 11:35 AM ………………………..…………………93

Figure 4.28 Comparison of MFRSR, Cimel, Aqua MODIS dark target and Deep Blue retrieved aerosol optical depths for August 2, 2013 at 1:15 PM. ………………………….. 93

Figure 4.29 Aerosol size distribution comparison derived from MFRSR and Cimel for August 2, 2013 during the clear sky cloud free day……………………………….…….. 94

Figure 4.30 Spectrally dependent AOD derived from the MFRSR data and Mie calculation by using the retrieved aerosol size distribution and refractive index for clear sky on August 2, 2013. ……………………………………………………………………………….... 95

Figure 5.1 Diffuse irradiance (top), normal direct irradiance (middle) and total irradiance (bottom) for 500 nm during the Rim fire on August 23, 2013 using MFRSR observed values and 2-stream model. ……………………………………………………………….… 100

Figure 5.2 Diffuse irradiance (top), normal direct irradiance (middle) and total irradiance (bottom) for 870 nm during the Rim fire on August 23, 2013 using MFRSR observed values and 2-stream model. ………………………………………………………………… 101

Figure 5.3 Variation of the SSA with wavelength using MFRSR and Cimel during the Rim fire on August 23, 2013. ……………………………………………………………….. 104
Figure 5.4 Comparison of the SSA using MFRSR at 415 nm and Photoacoustic measurements at 405 nm during the Rim fire on August 23, 2013 …………………….…106

Figure 5.5 Comparison of the SSA using MFRSR at 415 nm and photoacoustic at 405 nm during the clear sky day on October 24, 2013. …………………………………………… 107

Figure 5.6 Variation of the asymmetry parameter with wavelength using MFRSR and Cimel during the Rim fire on August 23, 2013. …………………………………………… 108

Figure 5.7 Asymmetry parameter for different channels (415, 500 and 870 nm) during the Rim fire on 23 August, 2013 retrieved from the MFRSR measurements. ……………….. 109

Figure 5.8 Variation of the imaginary part of refractive index with wavelength using MFRSR and Cimel during the Rim fire on August 23, 2013. ………………………...…………. 110

Figure 5.9 The imaginary part of the refractive index for different channels (415, 500 and 870 nm) during the Rim fire on August 23, 2013 using MFRSR…………………………..111

Figure 5.10 Diffuse irradiance (top), normal direct irradiance (middle) and total irradiance (bottom) for 500 nm during the dust storm on April 24, 2013 using MFRSR observed values and 2-stream model……………………………………………………………………....113

Figure 5.11 Variation of the SSA with wavelength using MFRSR during the dust storm on April 24, 2013. ………………………………………………………………………… 114

Figure 5.12 Variation of the asymmetry parameter with wavelength using MFRSR retrievals during the dust storm on April 24, 2013. …………………………………………………. 115

Figure 5.13 Variation of the imaginary part of refractive index with wavelength using MFRSR during the dust storm on April 24, 2013. ……………………………………….…116

Figure 5.14 Global solar irradiances during the cloud on May 27, 2013 (left panel) and on August 1, 2013 (right panel) ……………………………………………………………118

Figure 5.15 Diffuse irradiance (top), normal direct irradiance (middle) and total irradiance (bottom) for 500 nm during the clear sky on August 1, 2013 using MFRSR observed values and 2-stream model ………………………………………………………………………...120

Figure 5.16 Diffuse irradiance (top), normal direct irradiance (middle) and total irradiance (bottom) for 870 nm during the clear sky on August 1, 2013 using MFRSR observed values and 2-stream model. ……………………………………………………………………..121

Figure 5.17 Variation of the SSA with wavelength using MFRSR and Cimel during the clear sky on August 1, 2013. ……………………………………………………………..………122
Figure 5.18 Variation of the asymmetry parameter with wavelength using MFRSR and Cimel during the clear sky on August 1, 2013. ……………………………………………….…. 123

Figure 5.19 Variation of the imaginary part of refractive index with wavelength using MFRSR and Cimel during the clear sky on August 1, 2013. ………………………..…… 124

Figure 5.20 Aerosol radiative forcing at top of atmosphere during the Rim fire on August 23, 2013. ……………………………………………………………………………………. 126

Figure 5.21 Aerosol radiative forcing at top of atmosphere during the Dust storm on April 24, 2013…………………………………………………………………………………... 127

Figure 5.22 Aerosol radiative forcing at top of atmosphere during the clear sky on August 1, 2013. ……………………………………………………………………………………127

Chapter 1 Introduction

1.1 Atmospheric Aerosol

Atmospheric aerosols are fine solid or liquid particles suspended in a gas, which are emitted directly into the atmosphere by anthropogenic (e.g. fuel combustion, industrial processes, transportation) and biogenic (e.g. soil, volcanoes, mineral dust) sources or formed indirectly in the atmosphere by gas-to-particle conversion processes (Seinfeld and Pandis 2006). The aerosols which are directly emitted to the atmosphere are called primary aerosols, and those formed indirectly in the atmosphere are called secondary aerosols.

The concentrations, size and chemical compositions of atmospheric aerosols vary considerably in space and time, and consequently so do their effects on radiative properties. The sizes of the atmospheric aerosol particles are generally from a few nanometers (nm) to hundreds of micrometers (µm) in diameter (Pluschke, 2004). The fine aerosol particles (less than 1 µm diameter) originate mostly from condensation of the gases and incomplete combustion, and coarse aerosol particles (more than 1 µm diameter) are emitted due to re-suspension due to wind, and sea salt aerosols produced from breaking waves. Vehicle emissions and gas to particle conversion processes, including gaseous precursor emissions from vegetation such as pine forests are some of the sources for the fine mode aerosol in the atmosphere.

1.2 Effects of the Atmospheric Aerosol

1.2.1 Effects on Climate

Atmospheric aerosols have significant impacts on local and regional climate change (Chou et al. 2005). Human activities such as vehicle emissions, wood burning, and industrial processes are the local sources of urban air pollution (Mayer 1999). The atmospheric aerosols are organic and inorganic matter composed of fine and coarse particles that are suspended in the atmosphere and play an important role on the Earth‘s radiative forcing (Charlson et al. 1992). So-called “top of atmosphere” (*TOA*) radiative forcing is defined as the difference of solar radiation at the top of the atmosphere received by the Earth and energy reflected back to space.

Atmospheric aerosols affect the earth radiative balance in two ways. The first one is the direct radiative forcing effect, in which the absorption and scattering of solar radiation takes place by the atmospheric aerosols. During scattering, the sun light reflecting back to space has a cooling effect on the climate. The chemical composition of the aerosol determines how much solar radiation will be absorbed and scattered in the atmosphere. Sulfate, nitrate, and some organic aerosols scatter the solar radiation, providing a cooling effect (Dickerson et al. 1997). The black carbon and brown carbon absorb radiation giving a warming effect (Andreae and Gelencsér, 2006). The atmospheric aerosols from biomass burning and fuel burning processes can absorb and scatter solar radiation that convert the solar energy into heat energy and reflected light that produces a warming or cooling effect on climate, depending on the aerosol nature (Lohmann and Feichter, 2001).

The second way that aerosols impact climate is the indirect radiative forcing effect, which is further divided into two parts. The first indirect effect is associated with the cloud condensation nuclei role aerosols play in determining the number of cloud droplets, and the droplet size decreases for a fixed amount of liquid water, thereby increasing the cloud albedo (Twomey, 1974). The second indirect effect is when aerosols change the cloud lifetime, caused by modification of the cloud droplet fall speed and precipitation processes (Albrecht

1989). Both of these effects may cause an increase of the cloud reflectivity and give rise to a cooling effect on the atmosphere.

1.2.2 Effects on Human Health

Atmospheric aerosols have serious effects on human health, affecting a number of different systems and organs. The health effects of the aerosols are mainly due to impacts on respiratory function, and irritants to the eyes. The effects range from minor upper respiratory irritation to chronic respiratory, lung and heart disease (Kampa and Castanas, 2008). Some other effects are serious respiratory infections in children and chronic bronchitis in adults (Kampa and Castanas, 2008). Fine particles with a diameter below 1 μm transport harmful toxic chemicals into the human respiratory system (Siegmann, Scherrer, and Siegmann 1998) and are associated with lung cancer and cardiopulmonary mortality (Dockery et al. 1993, Pope et al. 2002).

1.3 Description of the Study

This study examines the optical and physical properties of aerosols, using three ground-based instruments and satellite measurements taken during the California Rim fire, desert dust, and clear-sky days. The ground-based measurements were obtained by using the Multi-Filter Rotating Shadowband (MFRSR), Cimel sun photometer, and photoacoustic instruments at the University of Nevada Reno (UNR). The satellite measurements provide the aerosol properties with nearly complete global coverage. The measurement strategies of the satellite are complicated due to different reflectance of various surfaces. It is difficult to separate the aerosol and surface contributions to the solar radiation received by satellite sensors. The ground-based remote sensing applications support evaluation and development of satellite retrievals protocols for determining aerosol properties.

The ground-based devices measure the down-welling solar radiation reaching the detector. The MFRSR measures the diffuse and total irradiances, from which the direct irradiances can be calculated, whereas the Cimel measures the direct radiance. The diffuse irradiance is the amount of the solar radiation received per unit area at the surface, coming from light scattered by molecules and particles in the atmosphere. The direct irradiance is the solar radiation received directly from the sun. Generally speaking, the contribution of scattering to the direct irradiance is very small. The measured direct irradiance is used to determine the spectrally resolved aerosol optical depth (*AOD*). The *AOD* is a basic optical measurement of aerosol loading in the atmosphere (K. H. Lee 2010). The optical activity of aerosols in the atmospheric column can be summarized by the wavelength dependence of the *AOD*.

Satellites provide wide spatial coverage but poor temporal sampling; some inherent difficulties and uncertainties cause errors in their retrieval accuracy (Li et al. 2009). The satellite MODIS dark-target retrieval can provide global coverage *AOD* values with estimated uncertainty errors of $\pm(0.03 + 0.05 * AOD)$ over the oceans and $\pm(0.05 + 0.2 * AOD)$ over land (Kaufman, Tanré, and Boucher, 2002), whereas the Deep Blue retrieved *AOD* values with estimated uncertainty errors of $\pm(0.04 + 0.1 * AOD)$ over bright surfaces like the Great Basin and the Saharan desert (Shi et al. 2012). The actual uncertainty of satellite retrievals is probably larger; therefore the satellite *AOD* observations with near global coverage are supplemented by the ground-based measurements. The ground-based instrument measured *AOD* can be obtained at much higher temporal resolutions and with more accuracy (K. H. Lee 2010). The ground based MFRSR and Cimel measurements can provide more accurate *AOD* values with uncertainty errors of ± 0.01 (Holben et al. 1998).

Particle size is an important parameter for characterizing the physical properties of atmospheric aerosols. Aerosol size distribution gives the relative concentrations of aerosol particles present in the atmosphere, arranged according to size (Queface, 2013). The size distribution of the aerosol particles in the atmosphere is often assumed to be a bimodal lognormal distribution that represents fine mode (diameter less than 1μm) and coarse mode (diameter greater than 1 μm) aerosols (Kassianov et al. 2007, Dubovik et al. 2002). The direct-to-diffuse ratio (*DDR*) is used to estimate the values of the single scattering albedo (*SSA*) and asymmetry parameter (*ASY*). The *SSA* is the fraction of the aerosol light extinction due to scattering and the *ASY* specifies the degree of scattering in the forward direction, varying from -1 (backward direction) to +1 (forward direction).

A 2-stream radiation transfer model and Mie theory are used to calculate the model values of *DDR* that are compared to the observed values of the *DDR* for the calculation of *SSA* and *ASY*. The photoacoustic instruments provide *SSA* values that may be compared to the *SSA* values found from the MFRSR retrievals. The estimated uncertainty error in MFRSR and Cimel derived values of *SSA* and *ASY* are about ±0.03 to 0.04 (Kassianov et al. 2007). The information about the aerosol properties such as *AOD*, *SSA* and *ASY* are used to calculate the all-important aerosol impact on solar radiative forcing at the top of the atmosphere.

1.4 Outline of Dissertation

The aim of this research is to study the optical and physical properties of aerosols, and direct radiative forcing of aerosols during the smoky, dusty and clear sky days. There are six chapters in this dissertation. The chapter 2 describes the working principle of the ground based MFRSR, Cimel and photoacoustic instruments. The brief descriptions of the Terra MODIS, Aqua MODIS and Deep Blue measurements are also presented in this chapter. The Langley regression retrieval algorithm is explained for the determination of the *AOD*.

Chapter 3 presents the retrieval algorithm for the aerosol properties (aerosol size distribution, *SSA*, *ASY*) and radiative forcing measurements. A 2-stream model for the determination of the *SSA* and *ASY* is also described in this chapter.

Chapter 4 describes the *AOD*, Angstrom exponent (*AE*) and aerosol size distribution during the Rim fire (August, September 2013), dust storm (April 24, 2013) and clear sky (May-October, 2013). The comparison of the ground-based and satellite measurements of *AOD* are also described in chapter 4.

In chapter 5, the measured solar irradiances (diffuse, direct and global) from MFRSR are compared with the retrieved solar irradiances from the 2-stream model. The retrieved *SSA* and *ASY* are obtained using MFRSR and Cimel during the Rim fire, dust storm and clear sky days. The comparison of the *SSA* from MFRSR and photoacoustic instruments is investigated for the Rim fire and for the clear sky days. The radiative forcing of the aerosol during the Rim fire and clear sky days are also compared in chapter 5. A summary of the dissertation and future outlook is given in Chapter 6.

1.5 Reference of Chapter 1

Albrecht, Bruce A. 1989. “Aerosols, Cloud Microphysics, and Fractional Cloudiness.” *Science* 245 (4923): 1227–30. doi:10.1126/science.245.4923.1227.

Andreae, M. O., and A. Gelencsér. 2006. “Black Carbon or Brown Carbon? The Nature of Light-Absorbing Carbonaceous Aerosols.” *Atmos. Chem. Phys.* 6 (10): 3131–48. doi:10.5194/acp-6-3131-2006.

Charlson, R. J., S. E. Schwartz, J. M. Hales, R. D. Cess, J. A. Coakley, J. E. Hansen, and D. J. Hofmann. 1992. “Climate Forcing by Anthropogenic Aerosols.” *Science* 255 (5043): 423–30. doi:10.1126/science.255.5043.423.

Chou, Chia, J. David Neelin, Ulrike Lohmann, and Johann Feichter. 2005. “Local and Remote Impacts of Aerosol Climate Forcing on Tropical Precipitation*.” *Journal of Climate* 18 (22): 4621–36. doi:10.1175/JCLI3554.1.

Dickerson, R. R., S. Kondragunta, G. Stenchikov, K. L. Civerolo, B. G. Doddridge, and B. N. Holben. 1997. “The Impact of Aerosols on Solar Ultraviolet Radiation and Photochemical Smog.” *Science* 278 (5339): 827–30. doi:10.1126/science.278.5339.827.

Dockery, Douglas W., C. Arden Pope, Xiping Xu, John D. Spengler, James H. Ware, Martha E. Fay, Benjamin G. Ferris, and Frank E. Speizer. 1993. “An Association between Air Pollution and Mortality in Six U.S. Cities.” *New England Journal of Medicine* 329 (24): 1753–59. doi:10.1056/NEJM199312093292401.

Dubovik, Oleg, Brent Holben, Thomas F. Eck, Alexander Smirnov, Yoram J. Kaufman, Michael D. King, Didier Tanré, and Ilya Slutsker. 2002. “Variability of Absorption and Optical Properties of Key Aerosol Types Observed in Worldwide Locations.” *Journal of the Atmospheric Sciences* 59 (3): 590–608. doi:10.1175/1520-0469(2002)059<0590:VOAAOP>2.0.CO;2.

Holben, B. N., T. F. Eck, I. Slutsker, D. Tanré, J. P. Buis, A. Setzer, E. Vermote, et al. 1998. “AERONET—A Federated Instrument Network and Data Archive for Aerosol Characterization.” *Remote Sensing of Environment* 66 (1): 1–16. doi:10.1016/S0034-4257(98)00031-5.

K. H. Lee, Z. Li. 2010. “Aerosol Optical Depth Measurements in Eastern China and a New Calibration Method.” *Journal of Geophysical Research* 115 (D00K11). doi:10.1029/2009JD012812, 2010.

Kampa, Marilena, and Elias Castanas. 2008. “Human Health Effects of Air Pollution.” *Environmental Pollution* 151 (2): 362–67. doi:10.1016/j.envpol.2007.06.012.

Kassianov, E. I., C. J. Flynn, T. P. Ackerman, and J. C. Barnard. 2007. “Aerosol Single-Scattering Albedo and Asymmetry Parameter from MFRSR Observations during the ARM Aerosol IOP 2003.” *Atmospheric Chemistry & Physics* 7 (June): 3341–51.

Kaufman, Yoram J., Didier Tanré, and Olivier Boucher. 2002. “A Satellite View of Aerosols in the Climate System.” *Nature* 419 (6903): 215–23. doi:10.1038/nature01091.

Li, Z., X. Zhao, R. Kahn, M. Mishchenko, L. Remer, K.-H. Lee, M. Wang, I. Laszlo, T. Nakajima, and H. Maring. 2009. “Uncertainties in Satellite Remote Sensing of Aerosols and Impact on Monitoring Its Long-Term Trend: A Review and Perspective.” *Annales Geophysicae* 27 (7): 2755–70. doi:10.5194/angeo-27-2755-2009.

Lohmann, Ulrike, and Johann Feichter. 2001. “Can the Direct and Semi-Direct Aerosol Effect Compete with the Indirect Effect on a Global Scale?” *Geophysical Research Letters* 28 (1): 159–61. doi:10.1029/2000GL012051.

Mayer, Helmut. 1999. “Air Pollution in Cities.” *Atmospheric Environment*, 4029–37. doi:10.1016/S1352-2310(99)00144-2.

Pluschke, Peter. 2004. *Indoor Air Pollution*. Springer.

Pope, C Arden, 3rd, Richard T Burnett, Michael J Thun, Eugenia E Calle, Daniel Krewski, Kazuhiko Ito, and George D Thurston. 2002. “Lung Cancer, Cardiopulmonary Mortality, and Long-Term Exposure to Fine Particulate Air Pollution.” *JAMA: The Journal of the American Medical Association* 287 (9): 1132–41.

Queface, Antonio Joaquim. 2013. “Direct Radiative Forcing by Aerosols over Southern Africa”. Thesis. http://wiredspace.wits.ac.za/handle/10539/13007.

Seinfeld, John H., and Spyros N. Pandis. 2006. *Atmospheric Chemistry and Physics: From Air Pollution to Climate Change*. Wiley.

Shi, Y., J. Zhang, J. S. Reid, E. J. Hyer, and N. C. Hsu. 2012. “Critical Evaluation of the MODIS Deep Blue Aerosol Optical Depth Product for Data Assimilation over North Africa.” *Atmos. Meas. Tech. Discuss.* 5 (5): 7815–65. doi:10.5194/amtd-5-7815-2012.

Siegmann, K., L. Scherrer, and H. C. Siegmann. 1998. “Physical and Chemical Properties of Airborne Nanoscale Particles and How to Measure the Impact on Human Health.” *Journal of Molecular Structure: THEOCHEM* 458 (1–2): 191–201. doi:10.1016/S0166-1280(98)00361-3.

Twomey, S. 1974. “Pollution and the Planetary Albedo.” *Atmospheric Environment (1967)* 8 (12): 1251–56. doi:10.1016/0004-6981(74)90004-3.

Chapter 2 Instrument Description

2.1 Multi-Filter Rotating Shadow-band Radiometer (MFRSRS)

2.1.1 Instrument Description and Operation

The MFRSR (Fig. 2.1) is a microprocessor controlled data acquisition instrument, which is used to collect spectral solar irradiance. It was developed by a team of scientists: L. Harrison, J. Michalsky and J. Bernt in a collaboration between the Atmospheric Science Research Center and the State University of New York and Battelle‘s Pacific Northwest Laboratory. The MFRSR is commercially manufactured by Yankee Scientific. The Multi-Filter successively passes different wavelengths of light; the Rotating Shadow-band is a motorized arm that periodically covers the sensor; and the Radiometer measures the intensity of passed solar radiation. It is environmentally sealed and thermally stabilized at around 40 ^{0}C temperature (Chen et al. 2013).

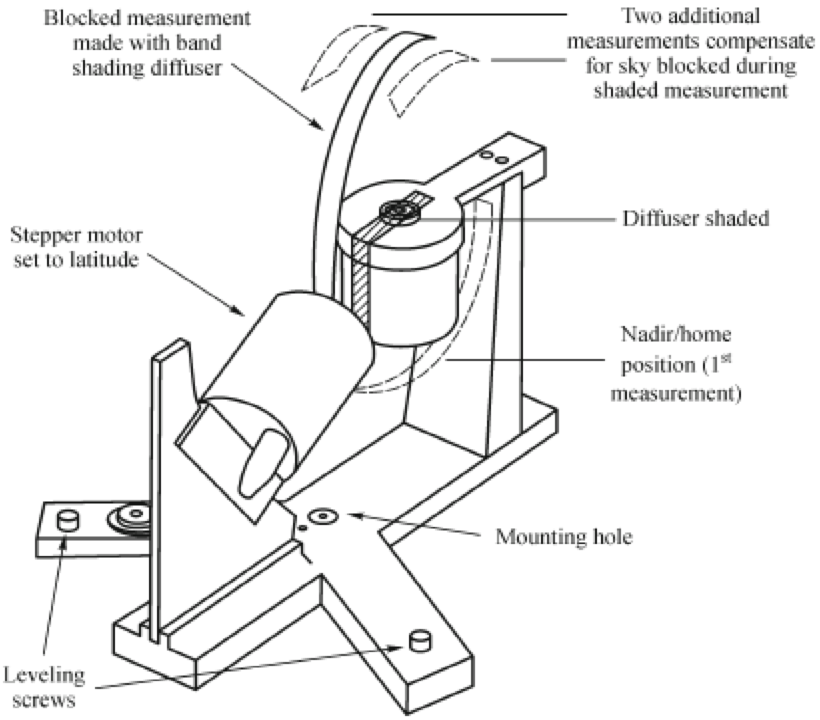

Figure: 2.1   Basic geometry of a MFRSR (Hodges and Michalsky, 2011).

The MFRSR is a field instrument that makes simultaneously spectral measurements of the horizontal solar irradiances at six nominal wavelengths: 415, 500, 615, 673, 870, and 940 nm.

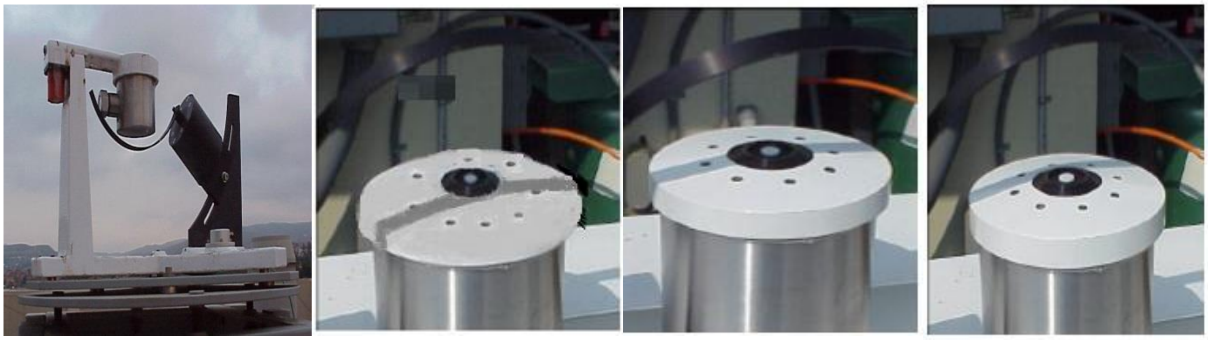

(a) (b) (c) (d)

Figure 2.2 (a) The MFRSR in home position (nadir position), (b) First side measurement (*fsb*) at 9^o off the sun blocking direction, (c) Middle measurement with the sun blocked, (d) Second side measurement (*ssb*) at 9^0 off the sun blocking direction (Muguel Bustamante, 2010).

The MFRSR makes independent measurements of the global and diffuse solar spectral irradiances. The global and diffuse irradiance measurements are used to calculate the direct normal irradiance. A single data record from the MFRSR is a set of four measurements (GB Hodges and Michalsky, 2011): (i) the initial horizontal measurement (total horizontal irradiance, tot_{hor}) is taken when the shadow band is in a home position (Fig. 2.2a, the nadir position); (ii) the first of the two side-band measurement (*fsb*) is taken when the shadow-band is 9^o off the sun blocking direction (Fig. 2.2b); (iii) the sun blocking measurement (*blk*) is taken when the shadow band blocked the sensor (Fig. 2.2c); and (iv) the second of the two side-band measurements (*ssb*) is taken when the shadow band is 9^o off the sun blocking direction (Fig. 2.2d). These measurements are executed when the curved metal strip (shadow band) rotates around the sensor shown in Fig. 2.2.

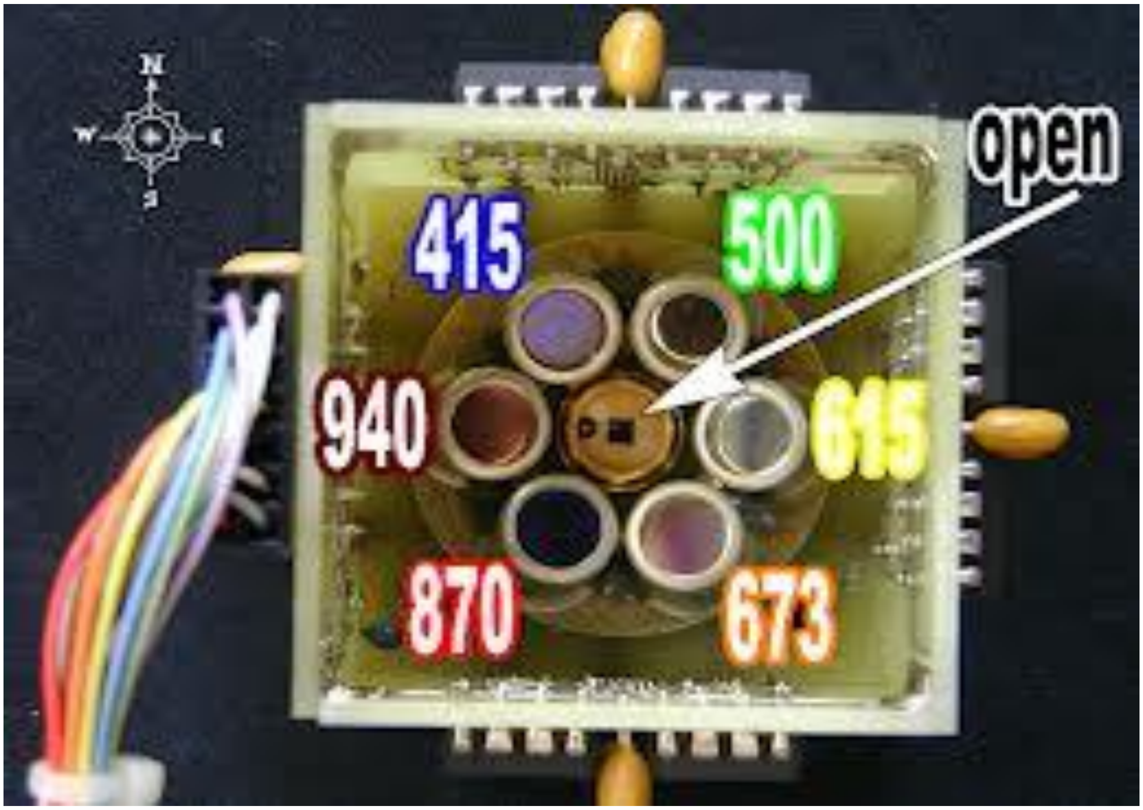

Figure 2.3 MFRSR Spectral Band filters; at center is the silicon with a range of 415-940 nm (from http://uvb.nrel.colostate.edu/UVB/ins_vismfrsr.jsf).

The MFRSR channels (Fig. 2.3 shows the sensors that measure each wavelength) are classified as the following: channels 415 nm, 500 nm, 673 nm, and 870 nm are mostly sensitive to aerosols; channel 615 nm is sensitive to ozone as well as aerosols; and channel 940 nm is sensitive to water vapor; this channel is excluded from this dissertation. The MFRSR is an important instrument in atmospheric research due to its automatic operation and its robustness (Muguel Bustamante, 2010).

2.1.2 Dark Offset Correction

Night-time data are averaged to calculate the dark offset (*offset)*, which is subtracted from all the measurements in the daytime before any further calculation. The diffuse *horizontal* irradiance is expressed by using the measurements obtained during the four measurements steps described in and below Fig. 2.2 (Chen et al. 2013). The diffuse horizontal measurement, $dif_{hor},$ is given by

$$dif_{hor} = blk + tot_{hor} - \left(\frac{fsb+ssb}{2}\right) \quad , \tag{2.1}$$

where the other variables are defined below Fig. 2.2.

The direct horizontal (dir_{hor}) is obtained from

$$dir_{hor} = (tot_{hor} - offset) - (dif_{hor} - offset) \quad , \tag{2.2}$$

$$dir_{hor} = tot_{hor} - dif_{hor} \qquad , \tag{2.3}$$

and

$$dir_{hor} = \left(\frac{fsb+ssb}{2}\right) - blk. \tag{2.4}$$

The direct horizontal component in Eq. 2.4 is used for aerosol optical depth determination.

2.1.3 Cosine Response Correction

The cosine correction is the normalized ratio or error of the measured angular response for each MFRSR channel. The theoretical cosine correction is equal to one when the sun is direct overhead. The instrument response at other angles is called the cosine-response. Ideally, the MFRSR would have a response that varies as the cosine of the zenith angle. However, the actual instruments hardly match this ideal (Seckmeyer and Bernhard 1993; Michalsky, Harrison, and Berkheiser III 1995; Feister, Grewe, and Gericke 1997). The magnitude of the cosine error can vary from a few percent to 20 percent, depending on the atmospheric conditions and characteristics of the system (Bais et al. 1998). The cosine correction for each MFRSR is recorded in the SolarInfo file. The cosine corrected diffuse horizontal (cor_dif_{hor}), direct horizontal (cor_dir_{hor}) and total corrected horizontal (cor_tot_{hor}) measurements are given below:

$$cor\_dif_{hor} = \frac{dif_{hor}}{(diffuse\ cosine\ correction)} \qquad , \tag{2.5}$$

$$cor\_dir_{hor} = \frac{dir_{hor}}{(direct\ \ cosine\ correction)} \qquad , \tag{2.6}$$

and

$$cor\_tot_{hor} = cor\_dif_{hor} + cor\_dir_{hor} \qquad , \tag{2.7}$$

Then, the direct normal measurement is calculated as:

$$dir_{norm} = \left(\frac{cor\_dir_{hor}}{cos\theta}\right) \qquad , \tag{2.8}$$

where θ is the solar zenith angle.

Fig. 2.4 shows an example of the corrected diffuse horizontal irradiance, direct normal irradiance and total horizontal irradiance, for all channels on a cloud free day using the UNR MFRSR. The scattering of the solar light due to the presence of the aerosol in the atmosphere plays an important role in solar radiation transfer that can be diagnosed using data like that shown in Fig. 2.4. The amount of scattered light depends upon the size and concentration of the aerosol particles and wavelength of solar light. The intensity of light varies as sixth power of particle size, and varies inversely with the fourth power of the wavelength for the particles much smaller than the wavelength of the light (Rayleigh regime). For particles larger than the wavelength of light the Mie scattering model is used for the scattering intensity. Mie scattering differs from Rayleigh scattering in several respects; it is roughly independent of wavelength and it is larger in the forward direction, than in the reverse direction. For the cloud free clear sky day, the values of the diffuse irradiance decrease as the wavelength increases for the example shown in Fig 2.4 because it is a relatively clear day where Rayleigh scattering by N_2 and O_2 dominates. On clear days, the diffuse irradiance value for 415 nm is highest and the lowest value is for 940 nm, because the 415 nm channel of the MFRSR is especially sensitive to aerosols and Rayleigh scattering by molecules, while the 940 nm channel is least sensitive to these factors, and also is subject to absorption due to water vapor.

The top panel of the Fig. 2.4 shows variation of the direct normal irradiance for different wavelengths. In the comparison of the 415 nm and 870 nm curves, the 870 nm data is notably flat whereas the 415 nm data is curved. The direct normal irradiance depends on the optical depth and airmass (see Eq. 2.9). The airmass changes with time of day. The values of airmass at morning and the evening times are higher than the mid-day time (between 10

AM to 4 PM), with values between 1.6 to 2.3 for that clear day and the time interval indicated. The total optical depths for these wavelengths depend on the aerosol optical depth and Rayleigh scattering optical depth. However, the Rayleigh optical depth and aerosol optical depth for the 415 nm are much higher than that for the 870 nm. Due to the low optical depth, the 870 nm curve is flatter than the 415 nm curve.

In Fig 2.4, we calculated the direct *horizontal* irradiance (leading to the top panel) by subtracting the diffuse horizontal irradiance (middle panel) from the total horizontal irradiance (bottom panel). However, the direct *normal* irradiance values in the top panel are calculated by dividing the direct *horizontal* irradiance values by the cosine of the solar zenith angle. Due to this reason, the lower panel of Fig. 2.4 has total horizontal irradiance values that are generally smaller than the direct normal irradiance values for all wavelengths because of the definition of the direct normal irradiance.

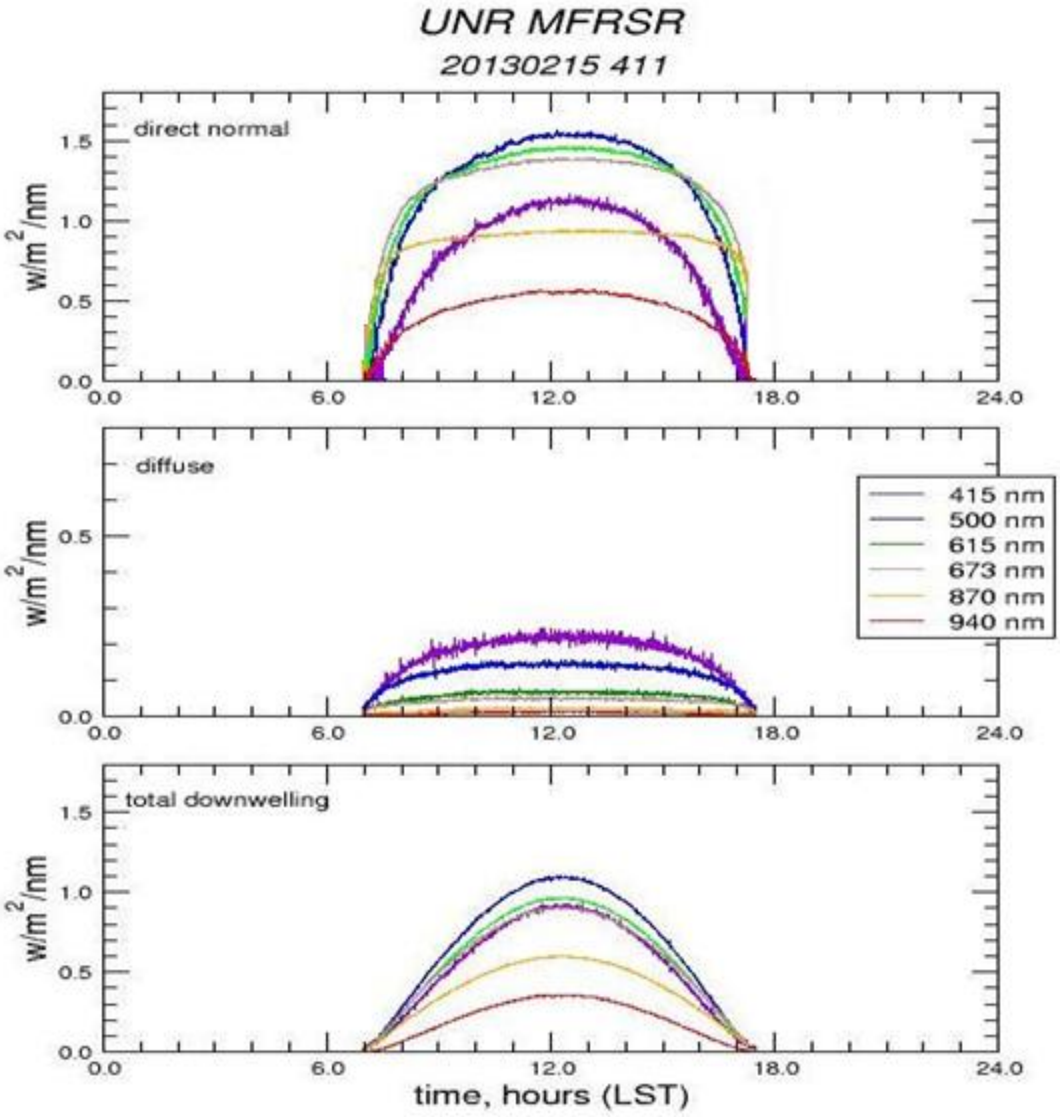

Figure 2.4 Example of daily solar plots from University of Nevada Reno site for February 15, 2013 using data from all channels.

2.1.4 Langley Regression Retrieval Algorithm

The MFRSR is located on roof of the physics building of the University of Nevada Reno (39.52°N, 119.81°W), measuring solar irradiance at six narrowband wavelengths (415, 500, 615, 673, 870, and 940 nm). The total optical depth (τ_{tot}) is calculated using the standard Beer's law approach (Hand et al. 2004).

$$I(\lambda) = I_0(\lambda)e^{-m\,\tau_{tot}} \ , \tag{2.9}$$

where $I(\lambda)$ is solar irradiance measured at the site of the instrument, $I_0(\lambda)$ is the solar irradiance at the top of the atmosphere and m is the airmass factor. The airmass is the amount of atmosphere between the sun and the earth's surface, normalized such that the airmass is equal to one when the sun is directly overhead (Koontz et al. 2013). Given the time of day and the site's latitude and longitude, the airmass is calculated using the formula (Kasten and Young 1989).

$$m = \frac{1}{\{cos\theta + 0.50572 * (96.07995 - \theta)^{-1.6364}\}} \ , \tag{2.10}$$

where θ is the solar zenith angle (Fig. 2.5) as measured from directly overhead to the geometric center of the sun's disc, as described using a horizontal coordinate system.

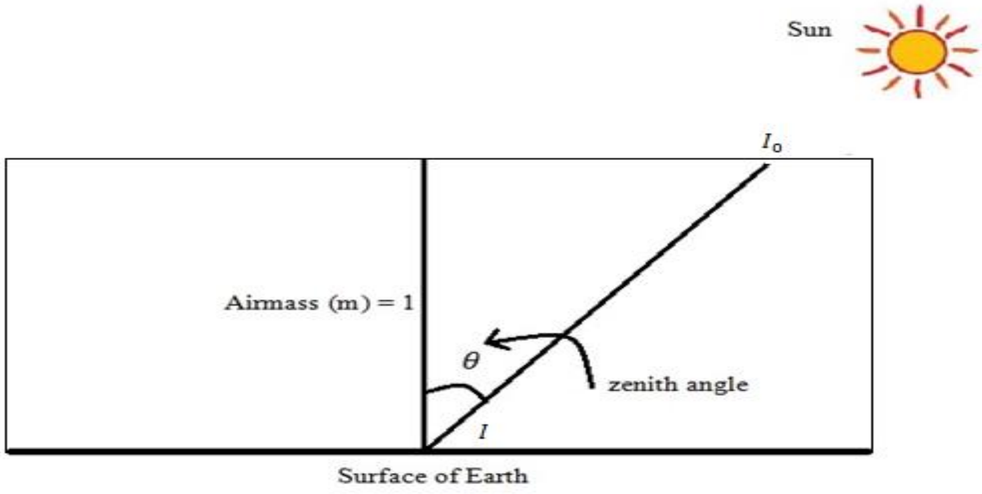

Figure 2.5 Basic ideas about the solar zenith angle and airmass.

Recall that I_0 and I are calibrated quantities with units of W/m^2/nm. In practice, we do not know what these quantities really are, prior to the calibration procedure. The MFRSR measures irradiances in uncalibrated units of "counts", V, related to the voltage output of the detectors. Conversion of "counts" to calibrated units can be done several ways, e.g., using a standard lamp or Langley regressions. However, to find optical depths, we can use uncalibrated data, because the optical depth depends only on the ratio of V and V_0 and therefore the calibration coefficients are irrelevant. To find this ratio V/V_0, we first find V_0 using Langley regressions.

The most important calibration assumption is that the atmosphere does not change with respect to time during the Langley regression on a given day, and that the day is cloudless, or the effect of clouds can be removed. To reduce the problem to a linear regression, the logarithmic form:

$$\ln\big(V(\lambda)\big) = -\,\tau_{tot} * m + \; ln\big(V_0(\lambda)\big) \qquad (2.11)$$

is used. This equation is similar to the linear form of a straight line:

$$y = a\,x + b \qquad , \qquad (2.12)$$

where $b = ln\big(V_0(\lambda)\big)$ and $a = \; -\tau_{tot}$ is the slope of the line (which is the negative optical depth). The best fit values for the coefficients $V_0(\lambda)$ and τ_{tot} ideally must be determined by applying a linear regression under perfectly clear sky conditions. For the real-world MFRSR data, we perform this operation for morning and afternoon when the airmass range is correct. An example of the Langley regression is shown in Fig. 2.6. The red curve is the plot of the natural logarithm of direct irradiance versus airmass for a clear sky day. The blue dotted line is the linear fit of the data and the magnitude of the slope is the total optical depth for that day.

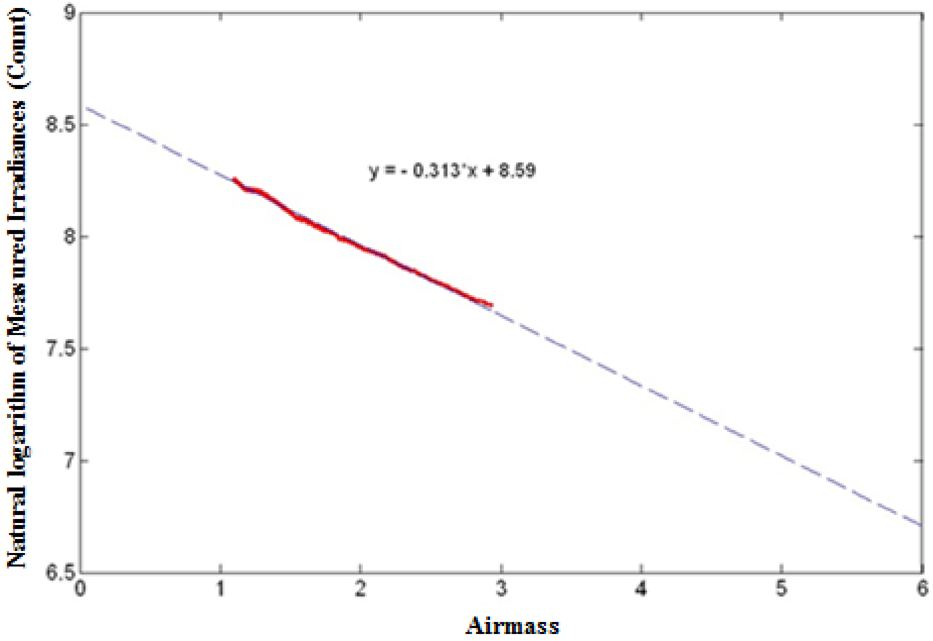

Figure 2.6 The natural logarithm of direct irradiance vs. airmass.

Fig. 2.7 shows the results of a typical Langley regression. It is important to keep in mind that these regressions are subject to noise, such as cloud contamination, and the fact that a V_0 found from one regression may not be the true value of V_0. Therefore we must find a way to use the results of many Langley regressions to find a robust value of V_0. We do this by finding a time series of V_0 and fitting a smooth curve to these values. This procedure is illustrated in Fig. 2.7, in which time series of V_0 are plotted for the 415 through 870 nm channels of the MFRSR. From this figure, one can see that for a particular wavelength, the V_0s are quite noisy.

A procedure to filter out this noise is described in Koontz et al., 2013. This procedure follows a three step process: First, a ratio of V_0s is taken from 415 nm and 870 nm wavelength channels. Second, a sliding window is applied for a two month length to the ratio time series. In this step all ratios in the lower and upper 25% quartiles are removed. This helps to remove the outliers. Finally, a Gaussian filter of 30 days width is used to smooth the time series of V_0s. From this process we get the final smoothed V_0 values, termed $V_{0,f}$, for the time corresponding to the center of the sliding window.

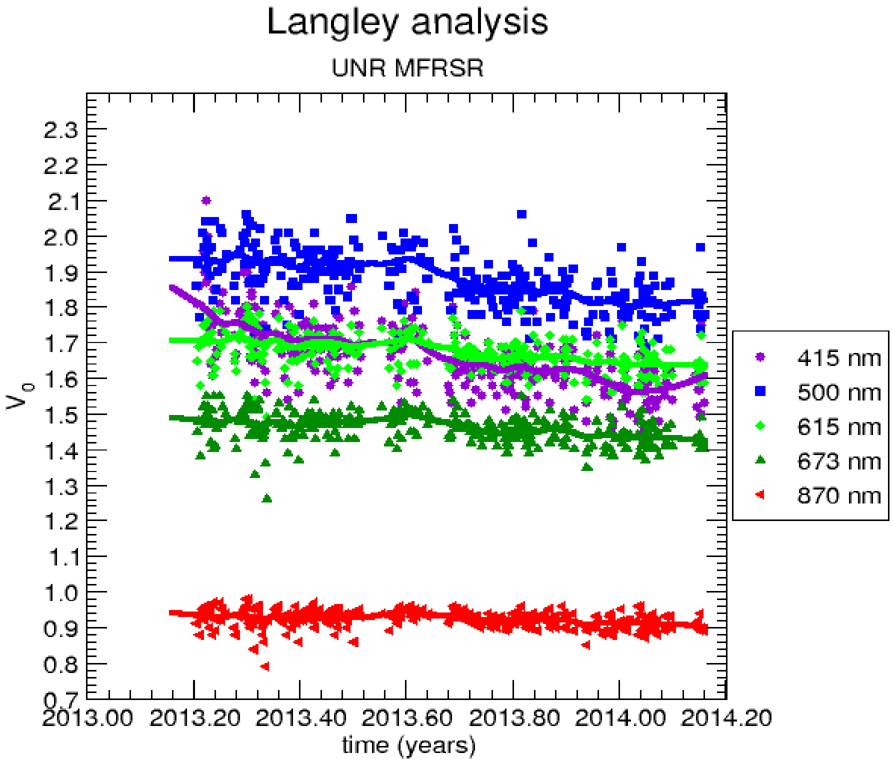

Figure 2.7 Time series of the V_0s (dots) from the UNR MFRSR for wavelengths 415, 500, 615, 673 and 870 nm. The daily-corrected $V_{0,f}$ values are obtained by a smooth curve fit to these data for each wavelength. These smooth curves are shown by the solid lines.

The total optical depth at each wavelength, at a given time, is obtained by taking the natural logarithm of Eq. (2.11), which is shown below:

$$\tau_{tot}(\lambda) = -\frac{1}{m}\, ln\left(\frac{V}{V_{0,f}}\right). \tag{2.13}$$

The total optical depth is comprised of contributions from aerosol, Rayleigh scattering by the air molecules, light absorption by ozone, and water vapor. Other gases, such as NO_2, also absorb but their effect is usually minor in the ultraviolet and visible spectral regions.

$$\tau_{tot}(\lambda) = \tau_{Aerosol}(\lambda) + \tau_{Ray}(\lambda) + \tau_{O_3}(\lambda) + \tau_{H_2O}(\lambda)\ . \tag{2.14}$$

Subtraction of the Rayleigh scattering by the air molecules, ozone and water vapor absorption optical depths from total optical depth yields the aerosol optical depth ($\tau_{Aerosol}$).

$$\tau_{Aerosol}(\lambda) = \tau_{tot}(\lambda) - \tau_{Ray}(\lambda) - \tau_{O_3}(\lambda) - \tau_{H_2O}(\lambda)\ . \qquad (2.15)$$

The Rayleigh optical depth (which must be subtracted from every channel of the MFRSR before obtaining the aerosol optical depth) is approximated as (J. E. Hansen and Travis 1974).

$$\tau_{Ray}(\boldsymbol{\lambda}) = 0.008569\boldsymbol{\lambda}^{-4}(1 + 0.0113\boldsymbol{\lambda}^{-2} + 0.00013\boldsymbol{\lambda}^{-4})\frac{P}{P_0} \quad , \qquad (2.16)$$

where $P_0 = 1013.24$ is the standard surface pressure at sea level and P is the pressure in mbar measured at the site of instrument. For the determination of the Rayleigh optical depth using the above formula, the wavelength is measured in micrometers (μm). The ozone absorption optical depth (τ_{O_3}) was calculated by multiplying the total column ozone (η) by the ozone absorption coefficients (a_λ).

$$\tau_{0_3} = \eta\ a_\lambda \quad . \qquad (2.17)$$

The ozone absorption coefficients for different wavelengths are given below:

Wavelength (nm)	**a_λ (cm^{-1}atm^{-1})**
415	0.0003
500	0.032
615	0.1162
673	0.0419
870	0.0013
940	0.0008

Table 2.1 Ozone absorption coefficients for different wavelengths (from Koontz et al. 2013).

In our analysis, the ozone column burden value is taken to be 300 DU (Dobson unit). Then, we divide that value by 1000 to get the ozone column in atm-cm units.

The top panel in Fig. 2.8 shows a typical time series of the aerosol optical depth (*AOD*) for the different five wavelengths: 415, 500, 615, 673 and 870 nm obtained from UNR MFRSR for the date April 18, 2013. The *AOD*s for this clear day are quite low; for 500 nm the average *AOD* is about 0.045. The calculation of the aerosol Ångström exponent is done by using the 500 nm and 870 nm wavelength for the MFRSR. The relation of the Ångström exponent is:

$$\tau_{aerosol}(\lambda) = A\,\lambda^{-\alpha} \quad , \tag{2.18}$$

where A is the prefactor in a two-term fit to the wavelength dependence and α is known as the Ångström exponent. Using this relation for two wavelengths 500 nm and 870 nm, the Ångström exponent (α) is derived as:

$$\alpha = \frac{-log\left(\frac{\tau_{aerosol}(500\ nm)}{\tau_{aerosol}(870\ nm)}\right)}{log\left(\frac{500}{870}\right)} \quad . \tag{2.19}$$

The Ångström exponent is an indirect calculation of the aerosol size. In general, when the Ångström exponent is less than 1, coarse mode particles are present. When the Ångström exponent is greater than 1, particles are mostly fine mode. Fig. 2.8 (lower panel) shows that the coarse mode particles contribution is higher during the morning time and fine mode particles increase in the atmosphere during the evening time.

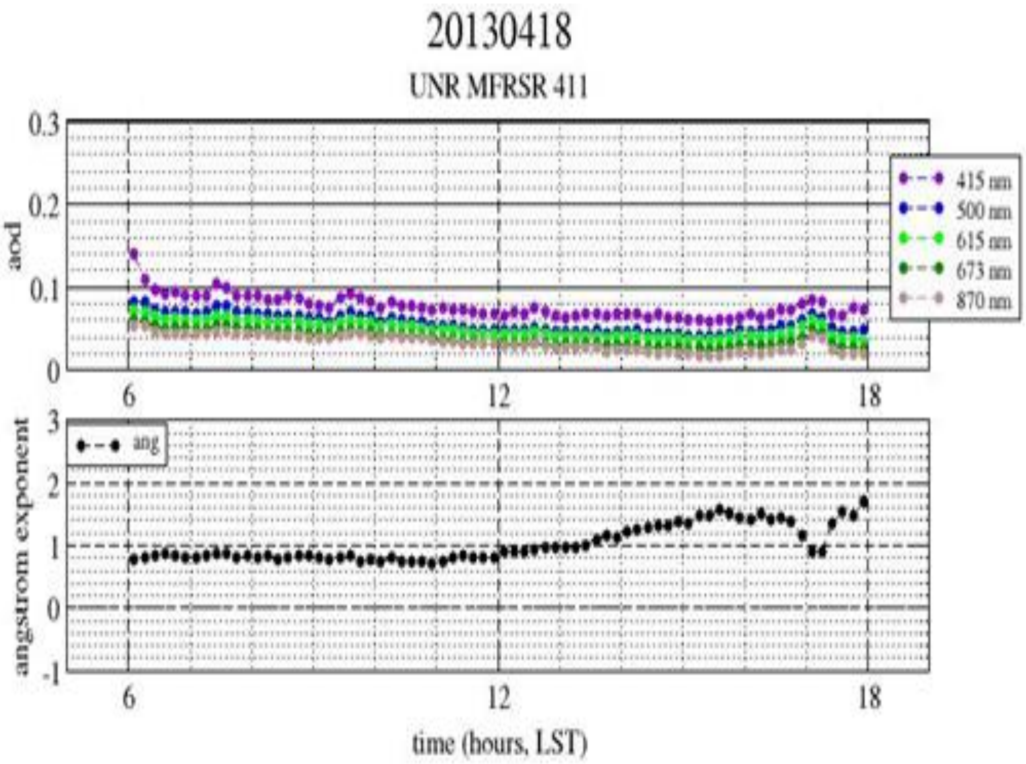

Figure 2.8 The top panel shows a time series of the *AOD* for five wavelengths and the lower panel displays the Ångström exponent using 500 nm and 870 nm channels.

2.2 Cimel Sun Photometer

2.2.1 Instrumentation and Data Collection

The Cimel CE-318 sun photometer of UNR is operated as part of the NASA AERONET (AErosol RObotic NETwork) network of sun-photometer ground-based aerosol measurements to, in part, evaluate retrievals of *AOD* by satellite. The Cimel CE-318 measures atmospheric aerosol columnar properties. This is a multi-channel, automatic sun-and-sky scanning radiometer that measures the direct solar and sky irradiance at the earth's surface. The instrument has a 1.2 degree field of view and two detectors for the measurement of sun and sky radiances. The detectors of the Cimel are constructed with a quartz window and enhanced silicon detector for the measurement of radiances between 340 nm and 1020 nm. Eight optical filters produce radiance measurements at 340, 380, 440, 500, 670, 870, 1020 and 1640 nm with band passes (FWHM) of 2 nm for the 340 nm channel, 4 nm for the 380 nm channel, and 10 nm for all visible wavelength channels (Holben et al. 2001).

Sun position is calculated internally based on time, latitude, and longitude. This information is then used to position the instrument sensor head. It provides the *AOD* at all wavelengths, along with the water vapor column content and the estimation of several optical and microphysical aerosol properties, such as the refractive index, size distribution, single scattering albedo and asymmetry parameter. The Cimel system is fully automatic and can be powered using solar panels. The modern digital and microcontroller units of high quality and robustness can collect data precisely and quickly with the onboard microprocessor (Schmid et al. 1997; Ehsani, Reagan, and Erxleben 1998; and Forgan 1994). Using direct solar irradiance, the total optical depth for each wavelength can be derived according to the Beer-Lambert-Bouguer law.

$$V_\lambda = \left(\frac{V_{0\lambda}}{R^2}\right)\exp(-\tau_\lambda\, m) \qquad , \tag{2.20}$$

where V_λ is the wavelength specific voltage, $V_{0\lambda}$ is the calibration constant for that wavelength, R is the earth-sun distance in Astronomical Units (AU), at the time of observation, and m is the relative optical airmass (as in Eq. 2.10). Fig. 2.9 shows that a sun photometer CE-318 is composed of an optical head, which has two channel systems for near IR and other wavelength range measurements. The instrument is mounted on an arm robot sensor pointed at nadir when the data are not taken to prevent contamination of the optical collimator from suspended particles and rain. The sun collimator is protected by a quartz window, the photons that pass through this window are sensed either with silicon or a InGaAS detector with sufficient signal-to-noise for spectral observations between 340 and 1640 nm (Holben et al. 1998). The Cimel sun photometer makes two measurements: The first is the direct sun irradiance measurement, and second is the sky radiance measurement.

Figure 2.9 The CE 318 automatic sun tracking photometer has been designed and realized to be a very accurate sun photometer with all the qualities of a field instrument (http://fsf.nerc.ac.uk/instruments/Cimel.shtml).

Fig. 2.10a shows the direct sun measurements; they are performed every 15 minutes at eight spectral bands. Using a combination of special filters it sequentially makes measurements at selected spectral bands centered at: 340, 380, 440, 500, 675, 870, 1020 and 1640 nm in about ten seconds. A sequence of three such measurements can be made 30 seconds apart, making a triplet observation per wavelength. This observation is used for recognizing the presence of clouds. The direct sun measurement gives the products *AOD*, precipitable water and Ångström coefficient given in Eq. 2.19.

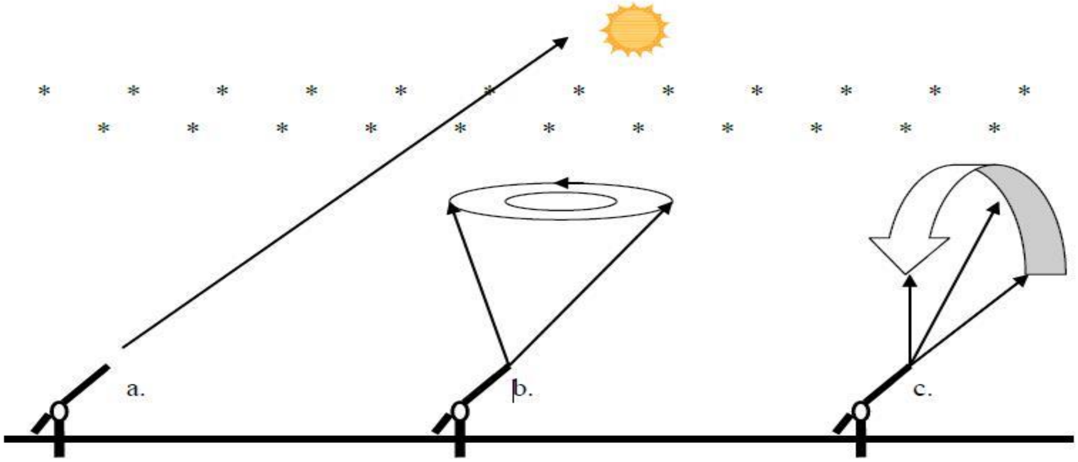

Figure 2.10 Representations of the (a) Direct, (b) Almucantar and (c) Principal plane measurements. Almucantar and principal plane are done only at 440, 675, 870 and 1020 nm channels. Direct measurement is done at all wave lengths: 340, 380, 440, 500, 670, 870, 940, 1020, and 1640 nm (Muguel Bustamante, 2010).

The direct sun measurements are made between airmass of 2 to 7 for both morning and afternoon and may be used for Langley calibrations. The airmass is calculated by using the solar zenith angle (Eq. 2.10). The zenith angles between 60^o to 80^o are important for the correct determination of the Langley calibration slope. Sky or diffuse measurements are made about once per hour at selected spectral bands: 440, 675, 870 and 1020 nm. There are two diffuse sky measurements shown in Fig. 2.10b and Fig. 2.10c.

The almucantar (Fig. 2.10b) scans the horizontal plane at constant solar zenith angle, with measurements at specified azimuths relative to the sun counterclockwise through 360^0 of azimuth (Muguel Bustamante, 2010). The almucantar measurements are normally made at an airmass of 2 or more to maintain large scattering angles (Rollin 2000). The direct sun measurement gives the aerosol optical depth, Ångström exponent, size distribution, and phase function.

The principal plane scan of the sky (Fig. 2.10c) is swept in a vertical direction rotating orthogonal to the azimuth plane spanning to 150^0. The idea of the direct sun, almucantar and principal plane measurements is to obtain the observations from a large range of scattering angles to retrieve size distribution, phase function and *AOD* (Holben et al. 1998, Nakajima et al. 1996, Tanré et al. 1988, and Kaufman 1993). The measured uncertainty in the retrieved *AOD* is estimated to be approximately 0.01 - 0.02 (Holben et al. 1998)

2.2.2 Cimel Data Processing and Products

As with the MFRSR measurements, the total optical depth measured with the Cimel is the sum of the Rayleigh optical depth (from atmospheric gases, e.g. nitrogen, oxygen, and argon), the ozone optical depth, the mixed gas optical depth (e.g. carbon dioxide, oxides of nitrogen), the water vapor optical depth and the *AOD*. The *AOD* is measured most directly by sun photometers like the Cimel. The sun photometer measurements are important as standards for evaluation of satellite derived values of *AOD*. Data collected from the Cimel, are processed by NASA AERONET. The level 1.0 raw *AOD* data are not calibrated and have no cloud screen; level 1.5 data are cloud screened; and level 2.0 data are cloud screened and calibrated.

The aerosol size distribution, refractive index, asymmetry parameter and single scattering albedo are determined using Cimel sky radiance measurements. The inversion scheme is used which involves a minimization procedure. The observed values of radiance and optical depth from Cimel are used for this minimization. The mean square error between the model and observed values is used for minimization scheme similar to that we use with the MFRSR, described below. The sky irradiance and optical depth are modeled as a function of the refractive index, volume size distribution and surface albedo (C. A. Corr, 2008).

$$I(\Theta,\lambda) = I\left(\frac{dV}{dlnr}, \mu(\lambda), A(\lambda)\right) + \Delta(\lambda,\Theta) \quad , \tag{2.21}$$

and

$$\tau(\lambda) = \tau\left(\frac{dV}{dlnr}, \mu(\lambda)\right) + \Delta(\lambda) \quad , \tag{2.22}$$

where I is sky irradiance, Θ is scattering angle, μ is complex part of the refractive index, A is surface albedo, and Δ denotes the uncertainty attributed to instrument error. Using this concept, values of aerosol size distributions and complex refractive indices limited by previous constraints are used to calculate radiance and optical depth. The optimized solution provides the best fit between measurements and the model. These retrieved aerosol properties are used to calculate the scattering optical depth ($\tau_{sca}(\lambda)$) and total optical depth as well as phase function ($P(\Theta,\lambda)$) as a function of size distribution, aerosol optical depth and scattering cross-section per particle as indicated by the equations (Dubovik and King 2000):

$$\tau_{sca}(\lambda)P(\Theta,\lambda) = \int_{r_{min}}^{r_{max}} \frac{K_{sca}(\Theta,\lambda,\mu,r)}{g_n(r)}\, x_n(lnr)\, dlnr \approx K_{sca}(\Theta,\lambda,n,k)x_n \ , \tag{2.23}$$

and

$$\tau(\lambda) = \int_{r_{min}}^{r_{max}} \frac{\tau(\lambda,\mu,r)}{g_n(r)}\, x_n(lnr)\, dlnr \approx K_{\tau}(\lambda,n,k)x_n \ , \tag{2.24}$$

where $K_{sca}(\Theta, \lambda, n, k)$ and $K_{\tau}(\lambda, n, k)$ are the kernel functions of the scattering cross-section and optical depth, and x_n is aerosol size distribution where, $n = 0, 1, 2, 3$ represents the number, radius, surface area, or volume of the distribution as follows (Dubovik and King 2000):

$$\text{For,} n = 0 \text{ (number)}, \ \ x_0(lnr) = \frac{dR^0(r)}{d\,lnr} = \frac{dN}{d\,lnr} \ ,$$

$$\text{For,} n = 1 \text{ (radius)}, \ \ x_1(lnr) = \frac{dR^1(r)}{d\,lnr} = r\frac{dN}{d\,lnr} = \frac{dR}{d\,lnr} \ ,$$

$$\text{For,} n = 2 \text{ (area)}, \ \ x_2(lnr) = \frac{dR^2(r)}{d\,lnr} = 2\pi r^2\frac{dN}{d\,lnr} = \frac{dS}{d\,lnr} \ ,$$

$$\text{For,} n = 1 \text{ (volume)}, \ \ x_3(lnr) = \frac{dR^3(r)}{d\,lnr} = \frac{4}{3}\pi r^3\frac{dN}{d\,lnr} = \frac{dV}{d\,lnr} \ .$$

The dependence of K_{τ} and K_{sca} on scattering angle (Θ), wavelength (λ), complex refractive index (μ), and particle radius (r) are approximated by matrices and look-up tables to improve inversion efficiency (Dubovik and King 2000). The total single scattering albedo (SSA) is given by (C. A. Corr, 2008):

$$SSA^{total}(\lambda) = \frac{\tau_{sca}^{total}(\lambda)}{\tau^{total}(\lambda)} \ . \tag{2.25}$$

The final inversion products from the retrieval are aerosol volume size distributions ($0.05 < r < 15\ \mu m$), effective radius, complex refractive index, asymmetry parameter, single scattering albedo and top of the atmosphere radiative forcing at different wavelengths. There are two versions of the AERONET inversion scheme: Version 1 and Version 2. These two versions employ the (Dubovik and King 2000) inversion; however, the inversion method has been improved to include additional aerosol microphysical properties (i.e., percentages of spherical and spheroidal particles; fine and coarse mode distinction) retrievals in version 2 (Dubovik et al. 2006).

Examples of the data output from AERONET for aerosol properties are given below in Fig. 2.11 and Fig. 2.12. The top panel of the Fig. 2.11 shows the variation of the AOD for all wavelengths during the day of the August 3, 2013. The lower panel of the Fig. 2.11 is the size distribution curve which indicates that the fine and coarse mode aerosol contribution are equal for that day. Fig. 2.12 shows the wavelength dependence of the single scattering albedo (top panel) and asymmetry parameter (lower panel). Both plots indicate that the single scattering albedo and asymmetry parameter decrease as wavelength increases.

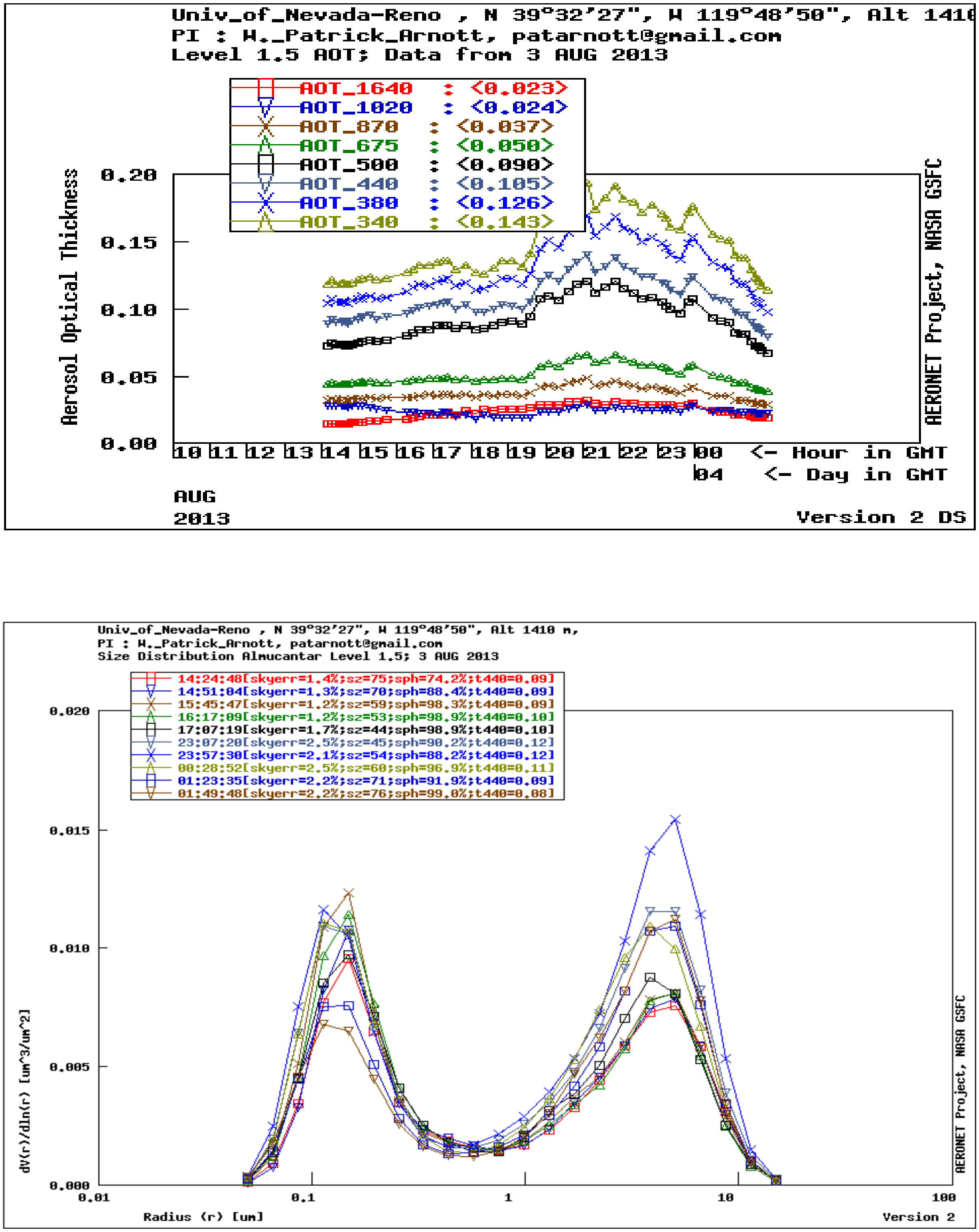

Figure 2.11 The variation of the AOD (top panel); and size (volume) distribution (lower panel) from UNR Cimel for August 3, 2013.

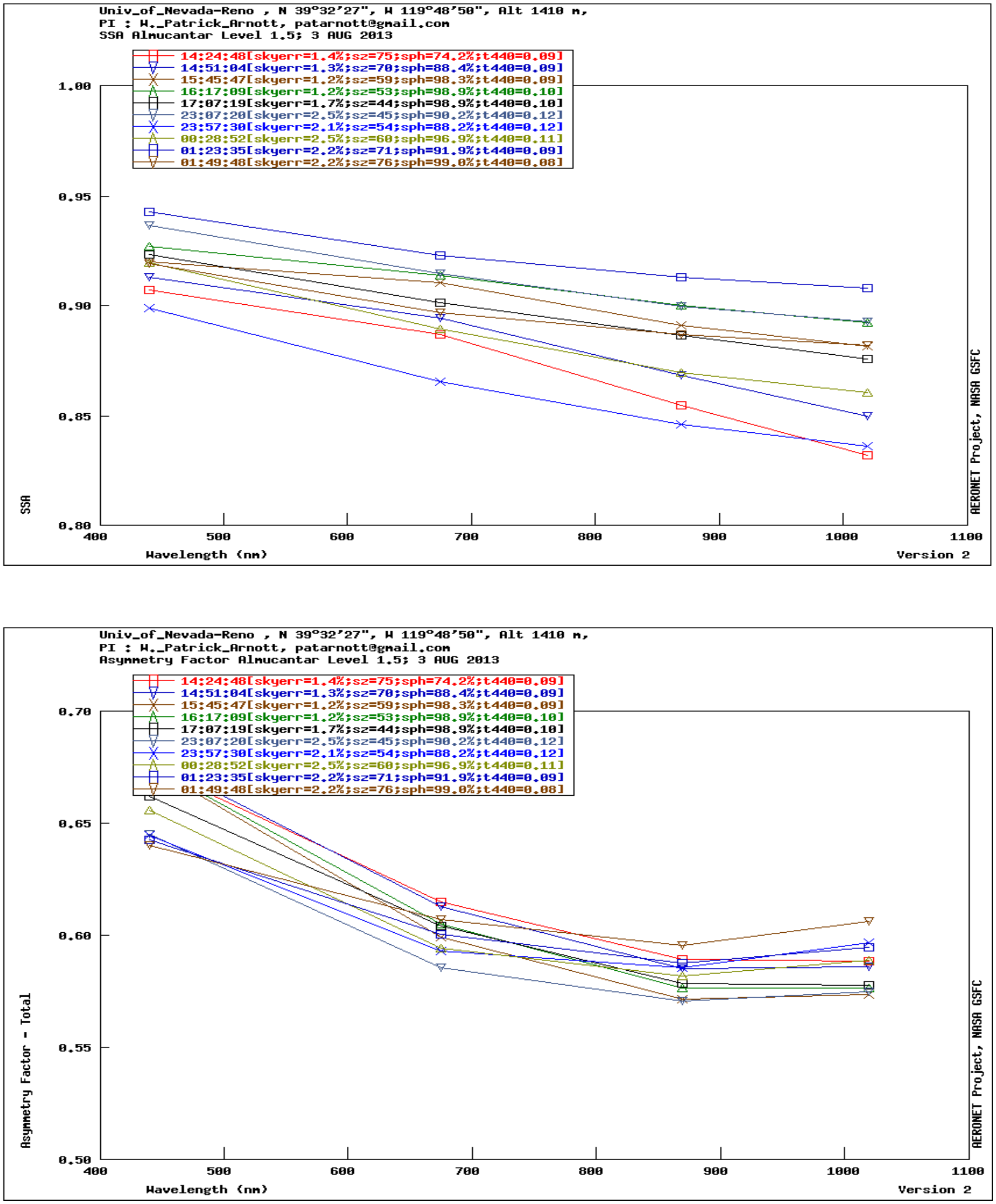

Figure 2.12 The spectral variation of the single scattering albedo (top panel); and asymmetry parameter (lower panel) from UNR Cimel for August 3, 2013.

2.3 Photoacoustic Instruments and Operation

A photoacoustic instrument has been developed to measure in situ light absorption by suspended atmospheric particles. The measured quantity is the sound pressure produced in an acoustic resonator caused by light absorption (Patrick Arnott et al. 1999). Fig. 2.13 shows the schematic of the single wavelength (532 nm) photoacoustic instrument.

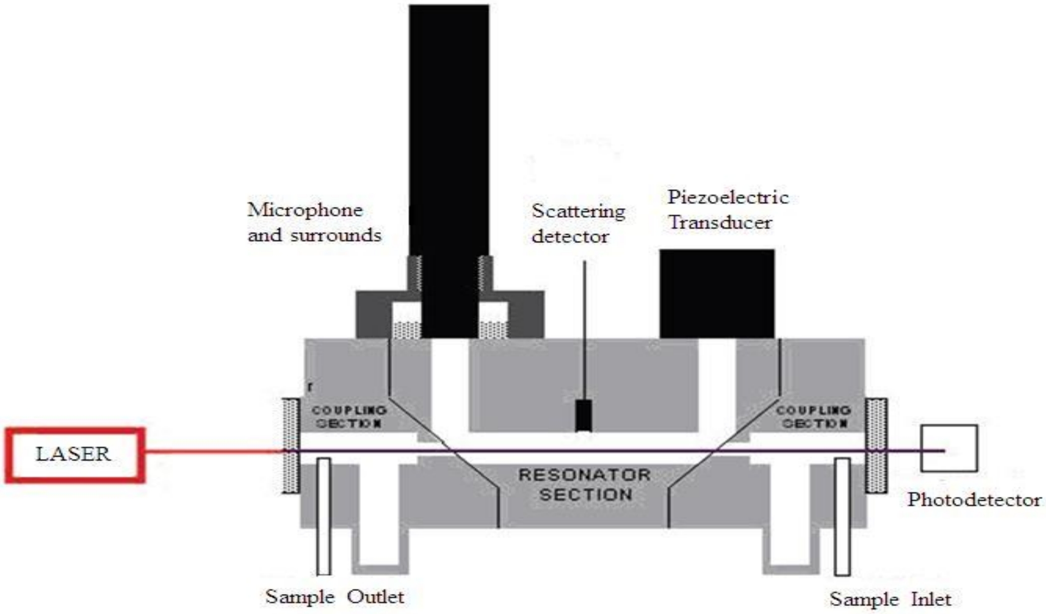

Figure 2.13 Schematic of 532 nm wavelength photoacoustic instrument (K. A. Lewis 2007).

An air sample is continuously introduced into the acoustic resonator during the photoacoustic operation. The sample air is illuminated by the laser radiation and then it is power modulated at the resonance frequency of the cavity. The radiation of the laser beam is absorbed by particles within the air sample inside the resonator, and then it is immediately transferred to the surrounding air as heat. A change in pressure is made by the heated air inside the resonator. The varying pressure disturbance caused by particle heat transfer is amplified by constructive interference. This is accomplishment by modulating the laser intensity to match the standing wave frequency of the resonator (K. A. Lewis 2007). The pressure fluctuations are measured by using the microphone in the resonator. The light absorbing components like gas or aerosol convert laser power to an acoustic pressure that are detected by the microphone positioned at a pressure anti-node (Patrick Arnott et al. 1999). The piezoelectric disk is used to determine the acoustic resonance frequency and quality factor of the resonator. The range of the microphone covers at least 6 orders of magnitude, resulting in a very large dynamic range for light absorption measurements (W. P. Arnott et al. 2005).

The resonance cavity is U-shaped. The length of the horizontal section is one half of acoustic wavelength and the lengths of the two vertical sections are one fourth of the acoustic wavelength. At the 90^o corners of the resonator, low pressure nodes of the standing wave exist but high pressure antinodes exist at both ends of the vertical sections and at the center of the horizontal section. The center of the cavity and two ends have high pressure points of the acoustic standing wave that are 180^o out of phase in the cycle is shown in Fig. 2.14.

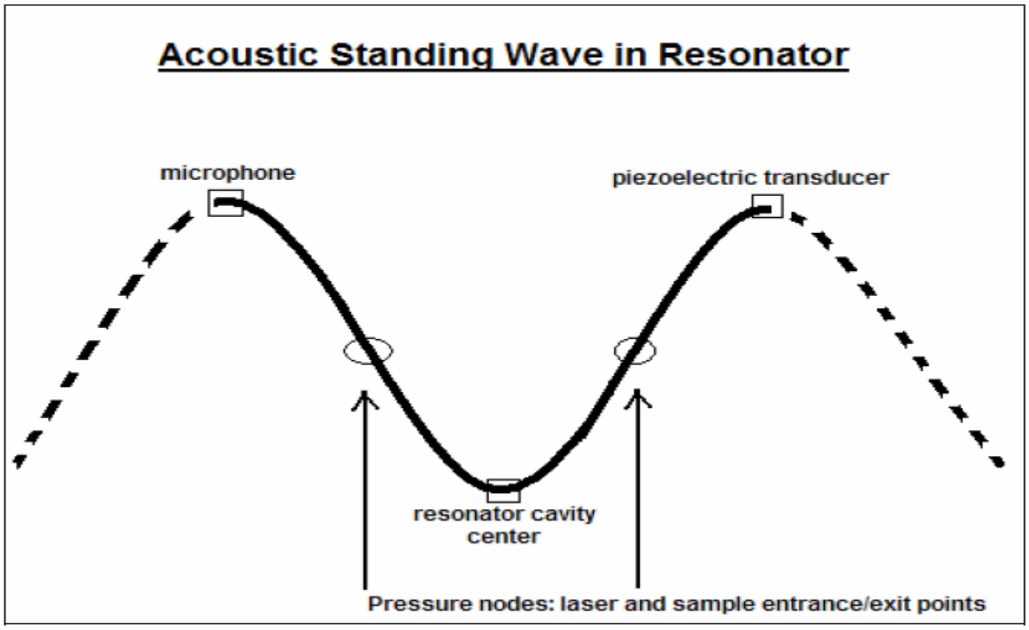

Figure 2.14 Schematic of the standing wave with high-pressure antinodes exist at microphone, piezoelectric transducer and central cavity locations (K. A. Lewis 2007).

The schematic of the dual wavelength photoacoustic instrument is shown in Fig. 2.15. The light scattering measurement is carried out with a cosine-weighted sensor located at the center of the cavity. The sensor is fiber coupled to a photomultiplier tube (PMT) for light scattering measurement.

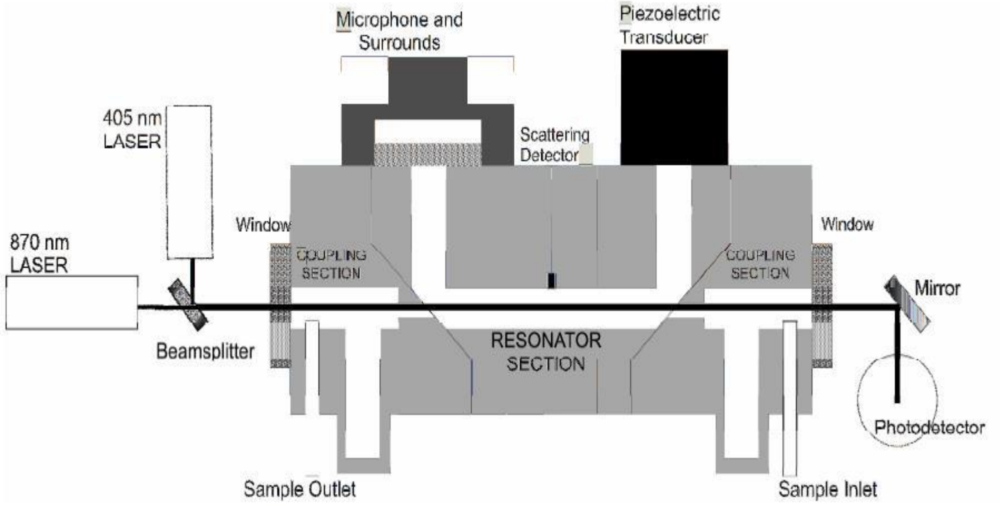

Figure 2.15 Schematic of duel-wavelength photoacoustic instrument (K. A. Lewis 2007).

The light absorption and scattering measurements were completed simultaneously with a dual-wavelength photoacoustic instrument operating at 405 and 870 nm (K. A. Lewis 2007), and two single-wavelength photoacoustic instruments operating at 532 and 1047 nm (W P Arnott et al. 2005b). The light absorption coefficient is given by the photoacoustic equation:

$$\beta_{abs} = \frac{P_m}{P_L}\frac{A_{res}}{\gamma-1}\frac{\pi^2 f_0 \cos(\emptyset_m-\emptyset_L)}{Q} \quad , \qquad (2.26)$$

where γ is the ratio of isobaric and isochoric specific heats of air and its value for dry air is 1.4 but in general depends upon relative humidity, P_m and P_L are the measured microphone pressure and laser power at the resonance frequency f_o, $\emptyset_m$ and $\emptyset_L$ are the electric phases of the microphone pressure and laser power measurements, respectively. A_{res} is the resonator cross-sectional area, and Q is the quality factor (Lewis et al., 2008).

The scattering coefficient is calculated by using the magnitude of the Fourier transformed function of PMT signal and power at resonance frequency:

$$\beta_{sca} = a\frac{|P_{PMT}|}{|P_L|} \quad , \tag{2.27}$$

where a is calibration factor determined during the instrument calibration, P_{PMT} and P_L are the photomultiplier tube signal and measured laser power (Lewis et al., 2008). The single scattering albedo (*SSA*) is defined as the ratio of scattering coefficient to extinction coefficient. The scattering and absorption coefficients from equations 2.26 and 2.27 are used to calculate the SSA. The relation of the *SSA* is given below:

$$SSA = \frac{\beta_{sca}}{\beta_{sca} + \beta_{abs}} \quad . \tag{2.28}$$

An example of the data output from photoacoustic instrument for absorption coefficient, scattering coefficient and *SSA* are given in Figures 2.16, 2.17 and 2.18, respectively, for August 23, 2013.

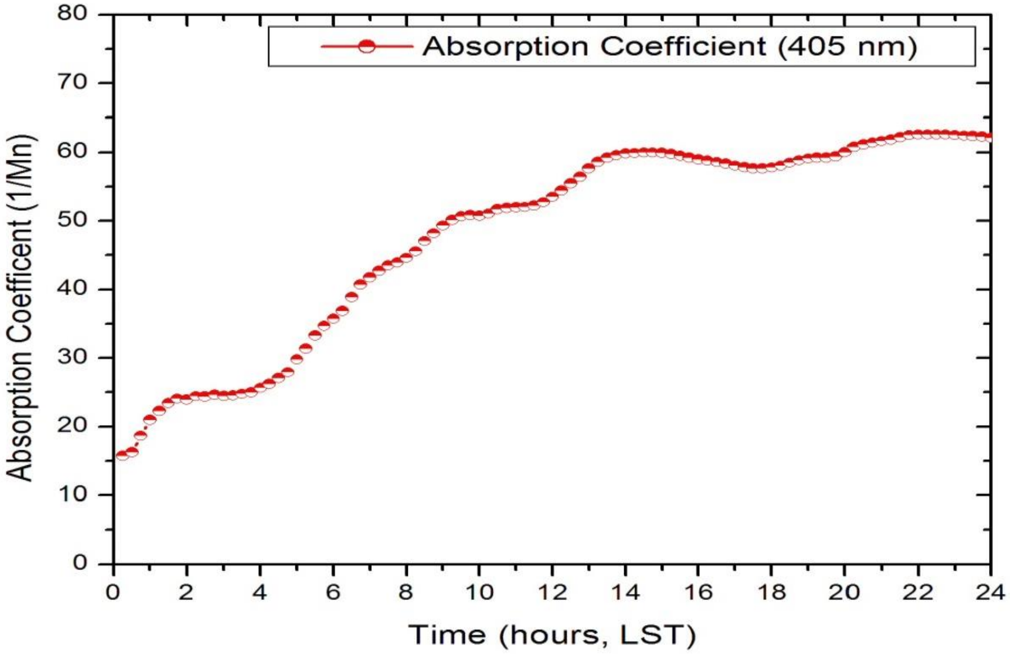

Figure 2.16 Time series of the absorption coefficient during the Rim Fire on August 23, 2013 using the photoacoustic instrument.

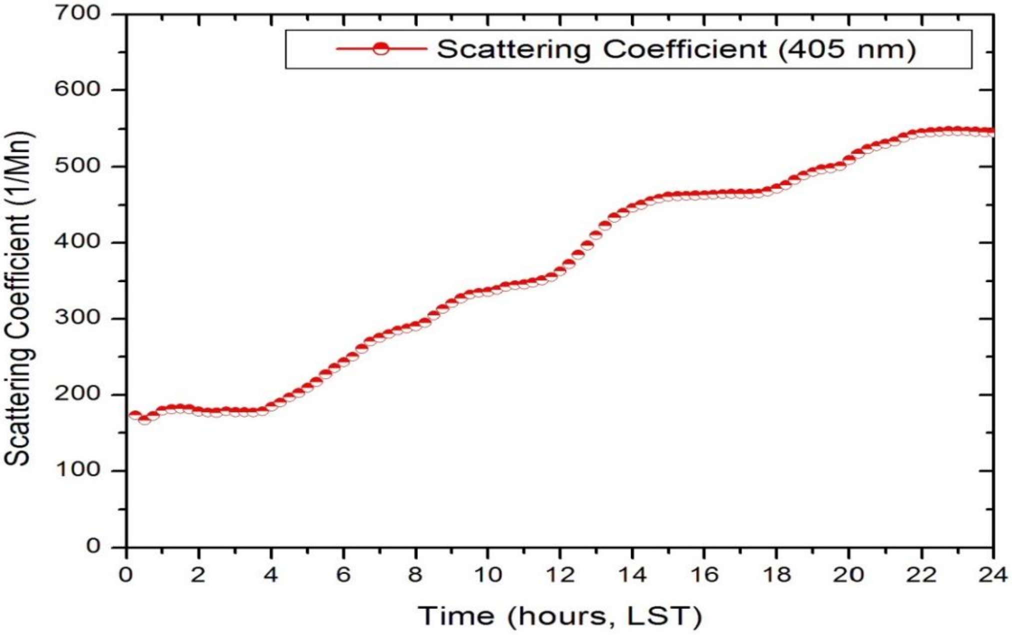

Figure 2.17 The scattering coefficient for the same day at in Fig. 2.16. August 23, 2013 using photoacoustic instrument.

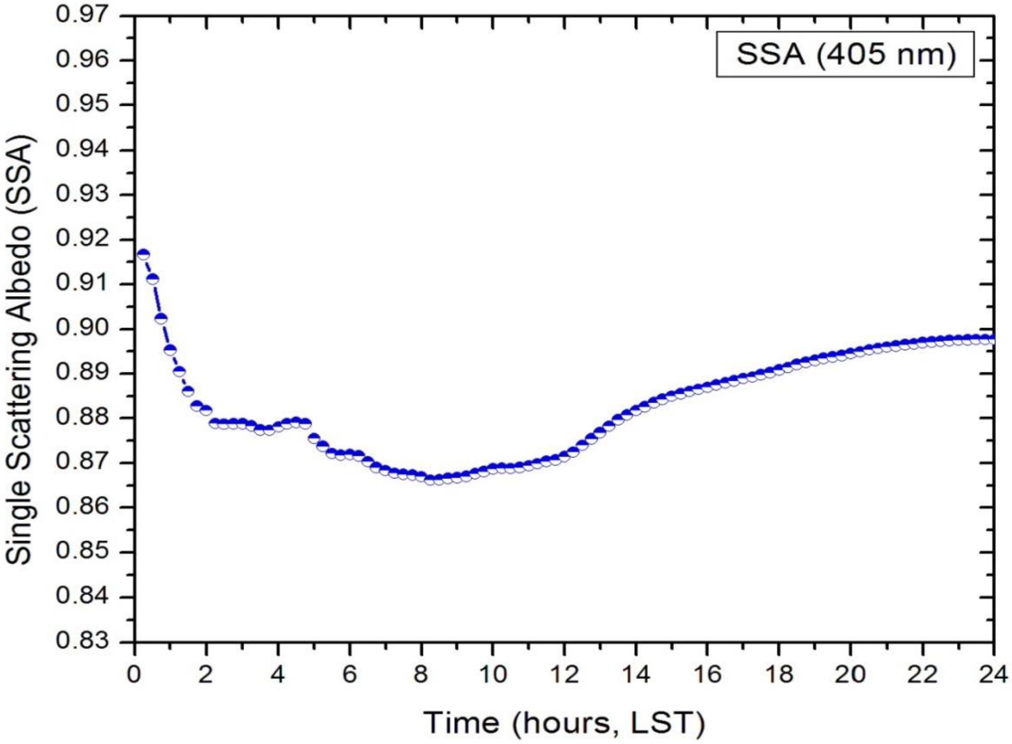

Figure 2.18 Time series of the *SSA* for August 23, 2013 using photoacoustic instrument.

2.4 MODIS Satellite Measurement

The Moderate Resolution Imaging Spectroradiometer (MODIS) is an instrument launched by NASA in 1999 on Terra and in 2002 on Aqua satellites. The Terra satellites orbits around the earth in the morning (about 10:30 AM) from north to south across the equator, while Aqua passes south to north over the equator in the afternoon (around 1:30 PM). The Terra and Aqua MODIS view the entire earth's surface every day, acquiring data in 36 spectral bands between 415 and 14235 nm. The MODIS aerosol products provide aerosol properties over both land (Y. J. Kaufman et al. 1997) and ocean (Tanré et al. 1997) as explained below.

The NASA Goddard Earth Sciences Distributed Active Archive Center (DES DAAC) is responsible for the distribution of the level 1 radiance data, and the higher levels of all ocean and atmosphere products (Savtchenko et al. 2004). The MODIS atmosphere products are grouped into the following data types: aerosol properties, atmospheric water vapor, cloud properties, atmospheric profiles and cloud mask (King et al. 2003). There are 5 separate data types for Terra and Aqua at level 2, and each data type is distributed as separate HDF files. We are interested in these atmospheric products. The description of the MODIS atmosphere data types that appear at level 2 are given as follows (Savtchenko et al. 2004):

- Aerosol properties (MOD04_L2 for Terra, MYD04_L2 for Aqua) data contains aerosol type, optical thickness, mass concentration, particle size distribution, cloud condensation nuclei (CCN), asymmetry factor, backscattering, and Ångström exponents.
- Atmospheric water vapor (MOD05_L2, MYD05_L2) data contains near-infrared estimates of total atmospheric column water vapor over clear land areas of the earth, over extended clear oceanic areas, and above clouds over both the land and ocean.

- Cloud optical and physical properties (MOD06_L2, MYD06_L2) data contains cloud temperature, cloud height, cloud pressure, cloud phase, cloud brightness temperature, cloud forcing, and surface temperature. The data also contains cloud reflectance, cloud water path, cloud optical thickness, and effective radius.
- Atmospheric profiles and stability indices (MOD07_L2, MYD07_L2) data contains temperature, moisture, total ozone, and stability indices. The total ozone burden is an estimate of the total tropospheric and stratospheric ozone column.
- Cloud mask (MOD35_L2, MYD35_L2) data contains global cloud mask, clear sky confidence level (high confident clear, probably clear, undecided, cloudy), and identifications of cirrus cloud.

For satellite measurements, the retrieval of the aerosol optical thickness over land is difficult because of the complexity of the earth land surface. The surface reflectance of land surface is variable with respect to different places and also changes with wavelength. There are many algorithms that have been applied to satellite datasets to solve the problem of separating the surface and atmospheric scattering contributions. For instance, MODIS retrievals of aerosol over land (Y.J. Kaufman et al. 1997) are based on the correlation of reflectance in the visible wavelengths of light. Dark surfaces have very low reflectance in the visible wavelength range (J. Hansen et al. 1992) and therefore provide good contrast for observing aerosol. The MODIS aerosol retrievals are performed using two separate algorithms, one for aerosols over land and the other for retrievals over ocean (Remer et al. 2002).

The Deep Blue algorithm was developed specially for aerosol retrievals over the bright surface such as deserts and urban areas. The algorithm was designed to tackle the problem of retrieving aerosol properties by making use of the fact that desert surfaces are much darker in the blue channels (412 and 470 nm) than they are in the red (660 nm) channel. The Deep Blue algorithm uses radiances measured from each channel and uses a radiative transfer model to calculate the intensity at top of the atmosphere for a given surface albedo. The surface reflectance for the 412, 470 and 660 nm channels are determined from a database based upon its geolocation (Hsu et al. 2004).

The cloud screening procedure is used to prevent retrievals with cloud-contaminated pixels. Additionally, the Deep Blue aerosol index (DAI) is used to distinguish thick dust layers from cloud, which is a similar measure to the Total Ozone Mapping Spectrometer (TOMS) aerosol index (Hsu et al. 2004). A Maximum Likelihood Estimation (MLE) is used to find the best match of modeled radiance as a function of AOD and single-scattering albedo for the given measured radiance. The assumptions are made on the dominant aerosol model used for the retrieval based on the geographical location and time of the year.

The Deep Blue algorithm produces outputs at the spatial resolution of the data from the satellite (250 meter resolution). The MODIS channels 8 (412 nm), 10 (470 nm), and 13 (660 nm) provide Deep Blue retrievals with higher resolution than the normal MODIS aerosol retrieval with the additional benefit of working over bright surfaces. The Deep Blue algorithm can be applied over bright surfaces such as arid, semiarid, urban, and desert surfaces.

Maps of Terra MODIS, Aqua MODIS and Deep Blue derived aerosol optical thickness at 550 nm of the Reno area on August 23, 2013 as presented in Figs. 2.19, 2.20 and 2.21. These plots indicate the high *AOD* in Reno during the Rim fire.

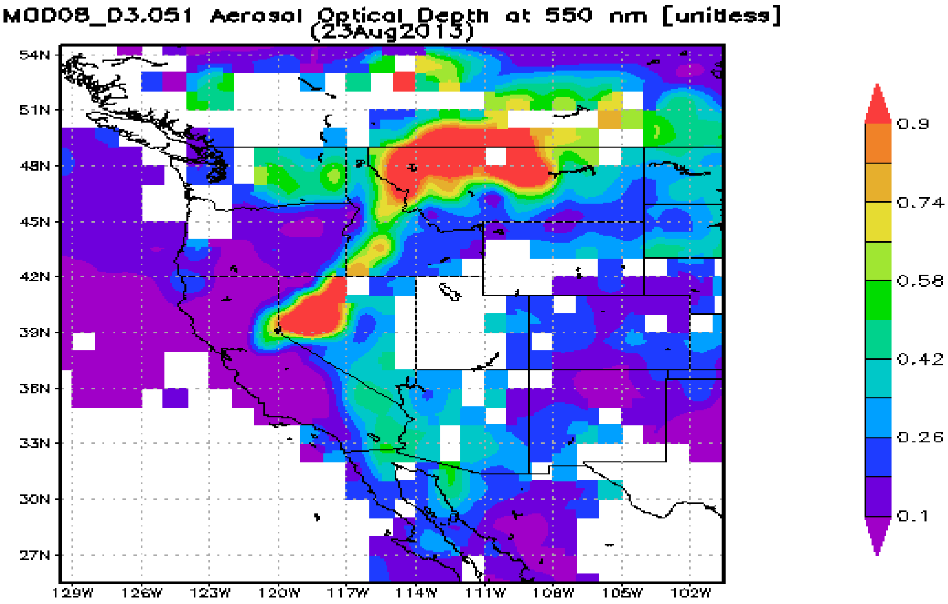

Figure 2.19 Terra MODIS derived aerosol optical thickness at 550 nm of the Reno land on August 23, 2013 near 10:30 am local time.

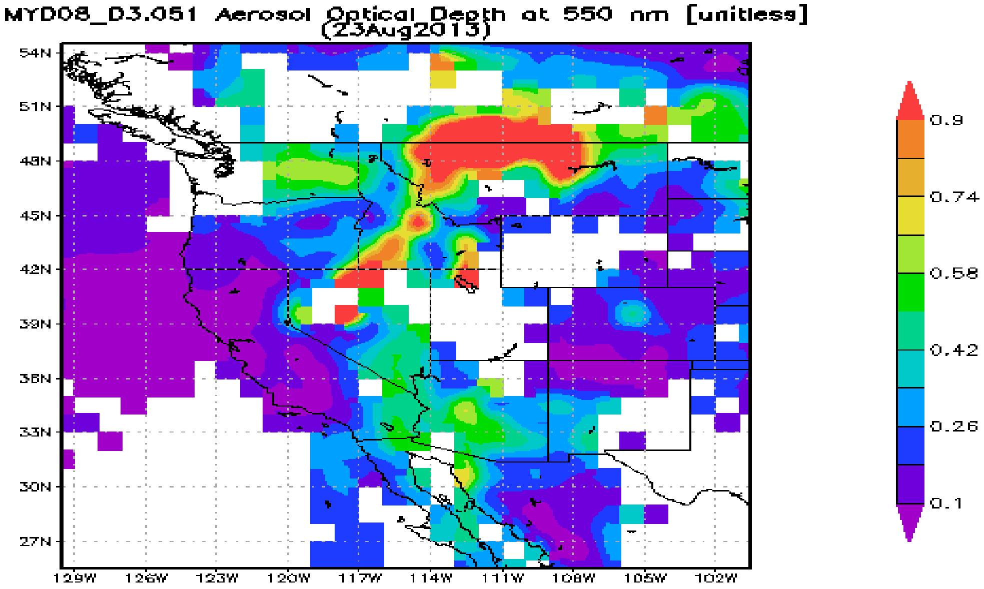

Figure 2.20 Aqua MODIS derived aerosol optical thickness at 550 nm of the Reno land on August 23, 2013 near 1:30 pm local time.

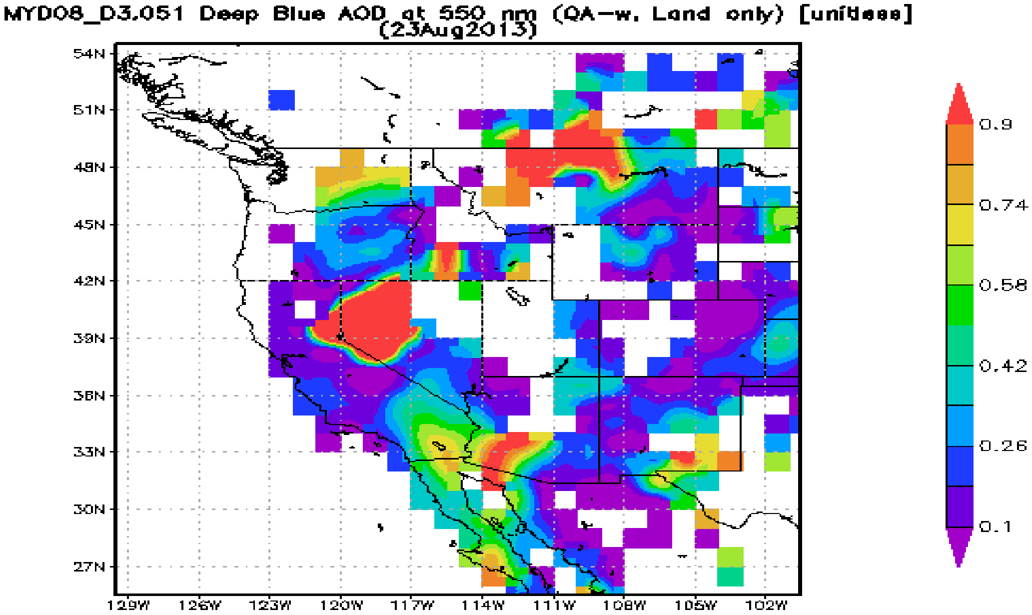

Figure 2.21 Deep Blue AOD at 550 nm of the Reno land on August 23, 2013 near 1:30 pm local time.

2.5 References for Chapter 2

Arnott, W P, B Zielinska, C F Rogers, J Sagebiel, Kihong Park, Judith Chow, Hans Moosmüller, et al. 2005. “Evaluation of 1047-Nm Photoacoustic Instruments and Photoelectric Aerosol Sensors in Source-Sampling of Black Carbon Aerosol and Particle-Bound PAHs from Gasoline and Diesel Powered Vehicles.” *Environmental Science & Technology* 39 (14): 5398–5406.

Bais, Alkiviadis F., Stelios Kazadzis, Dimitrios Balis, Christos S. Zerefos, and Mario Blumthaler. 1998. “Correcting Global Solar Ultraviolet Spectra Recorded by a Brewer Spectroradiometer for Its Angular Response Error.” *Applied Optics* 37 (27): 6339–44. doi:10.1364/AO.37.006339.

Muguel Bustamante, 2010. “Improved Processing and Development of the Multi-Filter Rotating Shadow-Band Radiometer (MFRSR) Network.” *Barnes & Noble*. Accessed January 17. http://www.barnesandnoble.com/w/improved-processing-and-development-of-the-multi-filter-rotating-shadow-band-radiometer-miguel-a-bustamante-benitez/1101727247.

C. A. Corr. "Retrieval of aerosol single scattering albedo at UV wavelength for two Urban fields campaign" PhD dissertation, Colorado State University, 2008.

Chen, Maosi, John Davis, Hongzhao Tang, Carolyn Ownby, and Wei Gao. 2013. “The Calibration Methods for Multi-Filter Rotating Shadowband Radiometer: A Review.” *Frontiers of Earth Science* 7 (3): 257–70. doi:10.1007/s11707-013-0368-9.

Dubovik, Oleg, and Michael D. King. 2000. “A Flexible Inversion Algorithm for Retrieval of Aerosol Optical Properties from Sun and Sky Radiance Measurements.” *Journal of Geophysical Research: Atmospheres* 105 (D16): 20673–96. doi:10.1029/2000JD900282.

Dubovik, Oleg, Alexander Sinyuk, Tatyana Lapyonok, Brent N. Holben, Michael Mishchenko, Ping Yang, Tom F. Eck, et al. 2006. “Application of Spheroid Models to Account for Aerosol Particle Nonsphericity in Remote Sensing of Desert Dust.” *Journal of Geophysical Research: Atmospheres* 111 (D11): n/a–n/a. doi:10.1029/2005JD006619.

Ehsani, A. R., J. A. Reagan, and W. H. Erxleben. 1998. “Design and Performance Analysis of an Automated 10-Channel Solar Radiometer Instrument.” *Journal of Atmospheric and Oceanic Technology* 15 (3): 697–707. doi:10.1175/1520-0426(1998)015<0697:DAPAOA>2.0.CO;2.

Feister, Uwe, Rolf Grewe, and Klaus Gericke. 1997. “A Method for Correction of Cosine Errors in Measurements of Spectral UV Irradiance.” *Solar Energy* 60 (6): 313–32. doi:10.1016/S0038-092X(97)00030-3.

Forgan, Bruce W. 1994. “General Method for Calibrating Sun Photometers.” *Applied Optics* 33 (21): 4841–50. doi:10.1364/AO.33.004841.

GB Hodges, JJ Michalsky. “Multifilter Rotating Shadowband Radiometer (MFRSR) Handbook.” doi:10.2172/1020261.

Hand, J.L., S.M. Kreidenweis, J. Slusser, and G. Scott. 2004. “Comparisons of Aerosol Optical Properties Derived from Sun Photometry to Estimates Inferred from Surface Measurements in Big Bend National Park, Texas.” *Atmospheric Environment* 38 (39): 6813–21. doi:10.1016/j.atmosenv.2004.09.004.

Hansen, James E., and Larry D. Travis. 1974. “Light Scattering in Planetary Atmospheres.” *Space Science Reviews* 16 (4): 527–610. doi:10.1007/BF00168069.

Hansen, James, Andrew Lacis, Reto Ruedy, and Makiko Sato. 1992. "Potential Climate Impact of Mount Pinatubo Eruption." *Geophysical Research Letters* 19 (2): 215–18. doi:10.1029/91GL02788.

Holben, B. N., D. Tanré, A. Smirnov, T. F. Eck, I. Slutsker, N. Abuhassan, W. W. Newcomb, et al. 2001. "An Emerging Ground-Based Aerosol Climatology: Aerosol Optical Depth from AERONET." *Journal of Geophysical Research: Atmospheres* 106 (D11): 12067–97. doi:10.1029/2001JD900014.

Holben, B.N., T.F. Eck, I. Slutsker, D. Tanré, J.P. Buis, A. Setzer, E. Vermote, et al. 1998. "AERONET—A Federated Instrument Network and Data Archive for Aerosol Characterization." *Remote Sensing of Environment* 66 (1): 1–16. doi:10.1016/S0034-4257(98)00031-5.

Hsu, N.C., Si-Chee Tsay, M.D. King, and J.R. Herman. 2004. "Aerosol Properties over Bright-Reflecting Source Regions." *IEEE Transactions on Geoscience and Remote Sensing* 42 (3): 557–69. doi:10.1109/TGRS.2004.824067.

Kasten, Fritz, and Andrew T. Young. 1989. "Revised Optical Air Mass Tables and Approximation Formula." *Applied Optics* 28 (22): 4735–38. doi:10.1364/AO.28.004735.

Kaufman, Y. J., D. Tanré, L. A. Remer, E. F. Vermote, A. Chu, and B. N. Holben. 1997. "Operational Remote Sensing of Tropospheric Aerosol over Land from EOS Moderate Resolution Imaging Spectroradiometer." *Journal of Geophysical Research: Atmospheres* 102 (D14): 17051–67. doi:10.1029/96JD03988.

Kaufman, Y.J., A.E. Wald, L.A. Remer, Bo-Cai Gao, Rong-Rong Li, and L. Flynn. 1997. "The MODIS 2.1-Mm Channel-Correlation with Visible Reflectance for Use in Remote Sensing of Aerosol." *IEEE Transactions on Geoscience and Remote Sensing* 35 (5): 1286–98. doi:10.1109/36.628795.

Kaufman, Yoram J. 1993. "Aerosol Optical Thickness and Atmospheric Path Radiance." *Journal of Geophysical Research: Atmospheres* 98 (D2): 2677–92. doi:10.1029/92JD02427.

King, M.D., W.P. Menzel, Y.J. Kaufman, D. Tanre, Bo-Cai Gao, S. Platnick, S.A. Ackerman, L.A. Remer, R. Pincus, and P.A. Hubanks. 2003. "Cloud and Aerosol Properties, Precipitable Water, and Profiles of Temperature and Water Vapor from MODIS." *IEEE Transactions on Geoscience and Remote Sensing* 41 (2): 442–58. doi:10.1109/TGRS.2002.808226.

Koontz, A., G. Hodges, J. Barnard, C. Flynn, and J. Michalsky. 2013. "Aerosol Optical Depth Value-Added Product Report". DOE/SC-ARM/TR-129. DOE Office of Science Atmospheric Radiation Measurement (ARM) Program (United States). http://www.osti.gov/scitech/biblio/1092419.

Lewis, Kristin A. 2007. "Development of a Dual-Wavelength Photoacoustic Instrument for Measurement of Light Absorption and Scattering by Aerosol and Gases." *ProQuest Dissertations And Theses; Thesis (Ph.D.)--University of Nevada, Reno, 2007.; Publication Number: AAI3258842; Source: Dissertation Abstracts International, Volume: 68-03, Section: B, Page: 1503.; 156 P.* http://adsabs.harvard.edu/abs/2007PhDT........54L.

Michalsky, J.J., L.C. Harrison, and W.E. Berkheiser III. 19
95. “Cosine Response Characteristics of Some Radiometric and Photometric Sensors.” *Solar Energy* 54 (6): 397–402. doi:10.1016/0038-092X(95)00017-L.

Nakajima, Teruyuki, Tadahiro Hayasaka, Akiko Higurashi, Gen Hashida, Naser Moharram-Nejad, Yahya Najafi, and Hamzeh Valavi. 1996. “Aerosol Optical Properties in the Iranian Region Obtained by Ground-Based Solar Radiation Measurements in the Summer Of 1991.” *Journal of Applied Meteorology* 35 (8): 1265–78. doi:10.1175/1520-0450(1996)035<1265:AOPITI>2.0.CO;2.

Patrick Arnott, W., Hans Moosmüller, C. Fred Rogers, Tianfeng Jin, and Reinhard Bruch. 1999. “Photoacoustic Spectrometer for Measuring Light Absorption by Aerosol: Instrument Description.” *Atmospheric Environment* 33 (17): 2845–52. doi:10.1016/S1352-2310(98)00361-6.

Remer, L. A., D. Tanré, Y. J. Kaufman, C. Ichoku, S. Mattoo, R. Levy, D. A. Chu, et al. 2002. “Validation of MODIS Aerosol Retrieval over Ocean.” *Geophysical Research Letters* 29 (12): MOD3–1–MOD3–4. doi:10.1029/2001GL013204.

Rollin, E. M. 2000. “An Introduction to the Use of Sun-Photometry for the Atmospheric Correction Ofairborne Sensordata. Annual Meeting of the Users of the NERC Airborne Remote Sensing Facility, Keyworth, Nottingham, United Kingdom, Airborne Research & Survey Facility (ARSF), 22 Pp.”

Savtchenko, A, D Ouzounov, S Ahmad, J Acker, G Leptoukh, J Koziana, and D Nickless. 2004. “Terra and Aqua MODIS Products Available from NASA GES DAAC.” *Advances in Space Research* 34 (4): 710–14. doi:10.1016/j.asr.2004.03.012.

Schmid, B., C. Matzler, A. Heimo, and N. Kampfer. 1997. “Retrieval of Optical Depth and Particle Size Distribution of Tropospheric and Stratospheric Aerosols by Means of Sun Photometry.” *IEEE Transactions on Geoscience and Remote Sensing* 35 (1): 172–82. doi:10.1109/36.551945.

Seckmeyer, Gunther, and Germar Bernhard. 1993. “Cosine Error Correction of Spectral UV-Irradiances.” In , 2049:140–51. doi:10.1117/12.163505. http://dx.doi.org/10.1117/12.163505.

Tanré, D., C. Devaux, M. Herman, R. Santer, and J. Y. Gac. 1988. “Radiative Properties of Desert Aerosols by Optical Ground-Based Measurements at Solar Wavelengths.” *Journal of Geophysical Research: Atmospheres* 93 (D11): 14223–31. doi:10.1029/JD093iD11p14223.

Tanré, D., Y. J. Kaufman, M. Herman, and S. Mattoo. 1997. “Remote Sensing of Aerosol Properties over Oceans Using the MODIS/EOS Spectral Radiances.” *Journal of Geophysical Research: Atmospheres* 102 (D14): 16971–88. doi:10.1029/96JD03437.

Chapter 3 Aerosol Optical and Physical Properties Retrieval and Radiative forcing

3.1 Introduction (Aerosol Size Distributions, Single Scattering Albedo and Asymmetry Parameter)

The radiative impact of aerosols depends on aerosol concentration in the atmosphere, their size, morphology and chemical composition (Pandithurai et al. 2008). The most significant sources of fine aerosol particulates come from motor vehicle emissions and smoke from wildfire and the sources of coarse aerosol particulates come from wind-blown dust and sea salt. The fine mode aerosols have particle diameter less than 1 µm whereas the coarse mode aerosols have particle diameter greater than 1 µm.

One of the most important properties of aerosol with respect to the direct forcing is the ratio of scattering and total extinction coefficients which is known as the single scattering albedo (ω);

$$\omega = \frac{\sigma_{sca}}{\sigma_{ext}} \qquad , \tag{3.1}$$

where σ_{sca} is scattering coefficient, and total extinction coefficient (σ_{ext}) is sum of aerosol absorption and scattering coefficients ($\sigma_{ext} = \sigma_{abs} + \sigma_{sca}$).

The aerosol asymmetry parameter (g) is defined as the cosine-weighted average of the phase function, where the phase function is the probability of radiation being scattered in a given direction. Assuming azimuthal asymmetry, the scattering angle extended from $-\pi$ to π then the asymmetry parameter is given as:

$$g = \frac{1}{2} \int_{-\pi}^{\pi} cos\theta \; P(\theta) \; sin\theta \;\; d\theta \qquad , \tag{3.2}$$

where θ is the scattering angle and $P(\theta)$ is the scattering phase function. The phase function is the angular distribution function of light intensity scattered by a particle at a given wavelength. The values for g range from -1 to 1, with a value of -1 indicating incident radiation is back scattered and a value of 1 indicating complete forward scattering (C. A. Corr et al. 2009). There are several methods for the determination of aerosol properties in the visible spectral range using direct sun and sky radiances by using Cimel, MFRSR and other radiometers. For example, as explained by Dubovik et al. (2002) the retrieval of aerosol optical depth and aerosol properties may be done using inversion techniques applied to observations of optical depth and angular distribution of sky radiances at visible and near-infrared wavelengths measured by the Cimel instrument described in Chapter 2. The method employed in this work for retrieval of aerosol optical properties at UV, visible, and near IR wavelengths uses MFRSR measurements of direct and diffuse irradiances and a retrieval model proposed by (Kassianov et al. 2005, Kassianov et al. 2007).

The volume size distribution, single scattering albedo and asymmetry parameter are retrieved from solar direct and diffuse irradiances measured with the MFRSR. The bimodal aerosol volume distribution concept is used. The bimodal concept states that the atmospheric aerosol mass is distributed in two size ranges: fine and coarse modes. Each aerosol mode has a characteristic size distribution, chemical composition and optical properties. In bimodal lognormal size distribution retrieval algorithm, it is assumed that the aerosols are composed of spherical and homogeneous particles. The scattering is simulated by using Mie theory, and multiple scattering effects are also taken into account (Pandithurai et al. 2008). For the bimodal retrievals, six additional items of information are needed: the aerosol concentration, effective radius, and effective variance for both coarse mode and fine mode components, assuming lognormal distribution for both fine and coarse modes.

3.2 MFRSR size distribution retrieval

The bimodal lognormal distribution is the most appropriate model for aerosol column-averaged size distribution representing both fine and coarse mode aerosol (Kassianov et al. 2007, Dubovik et al. 2002);

$$\frac{dV(r)}{dlnr} = \frac{C_f}{\sqrt{2\pi}\sigma_f}\ exp\left(\frac{-\left(lnr - lnR_f\right)^2}{2\sigma_f^2}\right) + \frac{C_c}{\sqrt{2\pi}\sigma_c}\ exp\left(\frac{-(lnr - lnR_c)^2}{2\sigma_c^2}\right), \tag{3.3}$$

where $dV(r)/dln(r)$ is the volume distribution, *r* is the particle radius, C is particle volume concentration, R is the volume median radius, σ^2 is the variance and the subscripts f and c stand for fine and coarse modes, respectively (Kassianov et al. 2007). The value of σ is taken to be 0.42 for the fine mode and 0.61 for the coarse mode (Dubovik et al. 2002). Then we have four unknown parameters (C_f, C_c, R_f, R_c) in the volume size distribution Eq. 3.3 so at least 4 independent measurements are needed to retrieve these parameters. The total volume of aerosol particles per unit area of the atmosphere (V_T) is then given as:

$$V_T = \int_0^\infty \left(\frac{dV}{dlnr}\right) dlnr = C_f + C_c \quad . \tag{3.4}$$

The two unknown parameters (C_f, C_c) are determined by using the size distribution retrieval procedure discussed below.

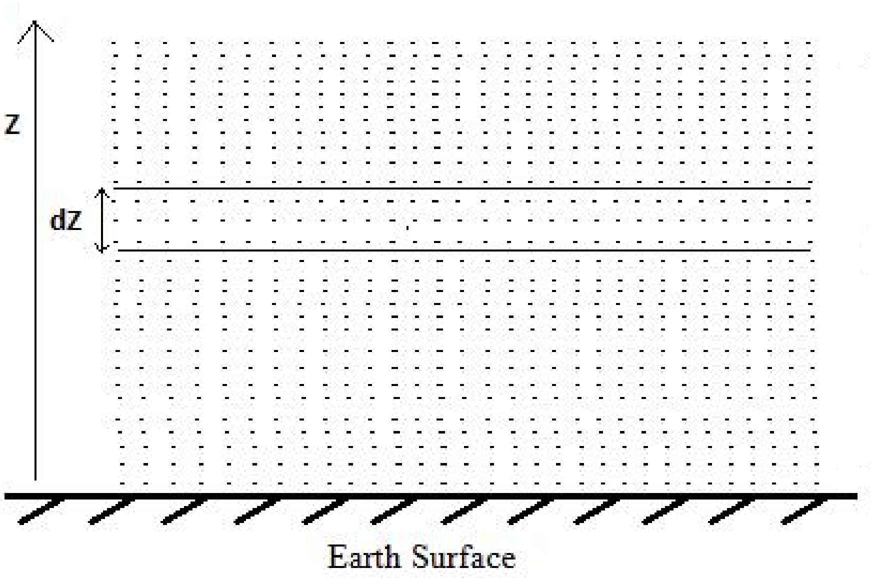

Figure 3.1 Aerosol distributions over the height of the atmosphere.

We consider the aerosol particles are distributed in the atmosphere over height z from the ground surface (Fig. 3.1). Then the *AOD* in terms of the aerosol number distribution given as:

$$\tau_\lambda = \int_{r=0}^{\infty} \int_{z=0}^{\infty} n(r,z)\ K_{ext,\,\lambda}(r, m_\lambda)\ dz\ dr\ , \tag{3.5}$$

where $n(r,z)$ is the aerosol number concentration distribution function over the height z, $K_{ext,\,\lambda}(r, m_\lambda)$ is extinction cross-section and $m_\lambda = (m_{1,\,\lambda} + i\, m_{2,\,\lambda})$ is complex refractive index. For our optical depth calculation, we set the real part of refractive index 1.5 and the imaginary part of refractive index 0.007 for each wavelength (E. I. Kassianov et al. 2007). The particle number distribution path in whole atmosphere is defined as:

$$n(r) = \int_{z=0}^{\infty} n(r,z) dz\ . \tag{3.6}$$

Then, we can relate the aerosol optical depth with particle number distribution path and extinction cross-section (using Eq. 3.5 and Eq. 3.6) given as:

$$\tau_\lambda = \int_{0}^{\infty} n(r)\ K_{ext,\,\lambda}(r, m_\lambda)\ dr\ . \tag{3.7}$$

We assume that all aerosol particles are assumed spherical. The volume size distribution $dV(r)/dln(r)$ and particle number size distribution path $n(r)$ are related as:

$$\int_0^\infty \frac{dV(r)}{dlnr} dlnr = \int_0^\infty \frac{4}{3}\,\pi r^3\ n(r)\, dr\ \ , \tag{3.8}$$

which gives;

$$n(r) = \frac{3}{4\pi}\,\frac{1}{r^4}\frac{dV(r)}{dln(r)} \qquad , \tag{3.9}$$

Then the *AOD* in term of the volume size distribution is given as:

$$\tau_\lambda = \int_0^\infty \frac{3}{4\pi}\,\frac{1}{r^4}\frac{dV(r)}{dln(r)}\ K_{ext,\,\lambda}(r, m_\lambda)\ dr \qquad . \tag{3.10}$$

The limit of the integration changes according to the size of the aerosol particle. For the measurement of *AOD*, we use the particle size range from $(r_{min} = 0.02\,\mu m)$ to $(r_{max} = 10\ \mu m)$. The *AOD* with volume size distribution Eq. 3.3 becomes:

$$\tau_\lambda^{model} = \int_{r_{min}}^{r_{max}} \begin{pmatrix} \frac{3C_f}{4\,\pi r^4\sqrt{2\pi}\sigma_f}\ exp\left(\frac{-\left(lnr - lnR_f\right)^2}{2\sigma_f^2}\right) + \\ \frac{C_c}{4\,\pi r^4\sqrt{2\pi}\sigma_c}\ exp\left(\frac{-(lnr - lnR_c)^2}{2\sigma_c^2}\right) \end{pmatrix} K_{ext,\,\lambda}(r, m_\lambda)\, dr. \tag{3.11}$$

The four unknowns (C_f, C_c, R_f, R_c) can be estimated by using the observed MFRSR aerosol optical depth $\tau_\lambda^{observed}$ at five wavelengths (415, 500, 615, 673, 870 nm) and an error minimization scheme. The values of these parameters that produce a minimum of the mean square error of optical depth over the five wavelengths are considered the best estimate of their values (Kassianov et al. 2007). The root-mean square error is given below:

$$error = \frac{1}{5}\sum_{j=1}^{5}\left(\tau_\lambda^{model} - \tau_\lambda^{observed}\right)^2 \quad . \tag{3.12}$$

From the mean square minimization, the unknown values (C_f, C_c, R_f, R_c) are found which are used in Eq. 3.3 to determine the aerosol size distribution. A conceptual example of the typical volume size distribution of aerosol in an urban environment is given below (Fig. 3.2). This plot shows that the fine and coarse modes of the aerosol volume size distribution.

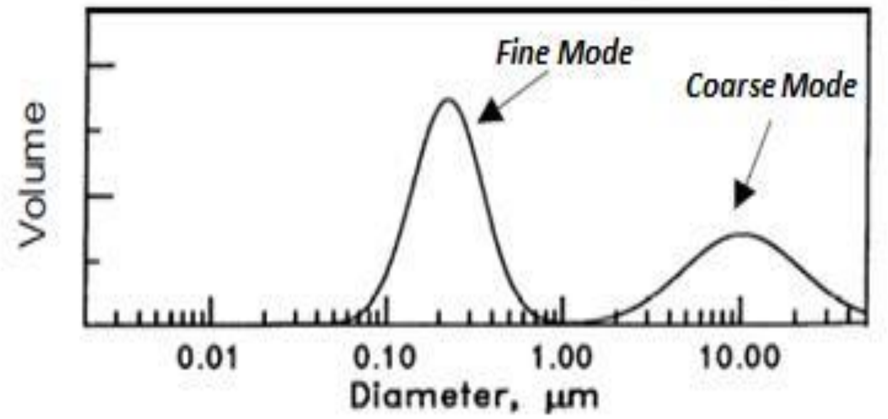

Figure 3.2 illustration of volume distributions for a typical urban model aerosol (Seinfeld and Pandis 1998).

3.3 MFRSR Single Scattering Albedo (SSA) and Asymmetry Parameter (g) retrieval

For the single scattering albedo and the asymmetry parameter, we assume that the aerosol particles are homogeneous spheres. The basic notion used in the retrieval is that the diffuse radiation amount is especially sensitive to these parameters. The wavelength dependent single scattering albedo (ω_λ) and asymmetry parameter (g_λ) are written as follows (Ge et al. 2010).

$$\omega_\lambda = \frac{\int_{r_{min}}^{r_{max}} \pi r^2 \, Q_s(m_\lambda, r/\lambda) \; n(r) \, dr}{\int_{r_{min}}^{r_{max}} \pi r^2 \, Q_e(m_\lambda, r/\lambda) \; n(r) \, dr} \quad , \tag{3.13}$$

$$g_\lambda = \frac{\int_{r_{min}}^{r_{max}} \pi r^2 g(r) \; Q_s(m_\lambda, r/\lambda) \; n(r) \, dr}{\int_{r_{min}}^{r_{max}} \pi r^2 \, Q_s(m_\lambda, r/\lambda) \; n(r) \, dr} \quad , \tag{3.14}$$

where r is the aerosol particle radius, $Q_s(m_\lambda, r/\lambda)$ and $Q_e(m_\lambda, r/\lambda)$ are scattering efficiency and extinction efficiency respectively. Both efficiencies are function of the imaginary part of refractive index (m_λ). The columnar aerosol particle number size distribution path $n(r)$ can be determined by using Eq. 3.3 and Eq. 3.9, which is given below:

$$n(r) = \frac{3C_f}{4\,\pi r^4 \sqrt{2\pi}\sigma_f} \, exp\left(\frac{-\left(lnr - lnR_f\right)^2}{2\sigma_f^2}\right) + \frac{3C_c}{4\,\pi r^4 \sqrt{2\pi}\sigma_c} \, exp\left(\frac{-(lnr - lnR_c)^2}{2\sigma_c^2}\right) . \tag{3.15}$$

We can determine the number size distribution $n(r)$ by using values of (C_f, C_c, R_f, R_c) and assumed values for (σ_f, σ_c) from size distribution retrieval explained in Section 3.2. Then we can calculate single scattering albedo (ω_λ) and asymmetry parameter (g_λ) simultaneously from Mie theory if the imaginary part of the refractive index (m_λ) is known. We used the diffuse – to – direct ratio (*DDR*) at five wavelength 415, 500, 515, 673 and 870 nm (Kassianov et al. 2007) to estimate the imaginary part of the refractive index (m_λ). We begin by assuming the value of m_λ, which is now only unknown parameter in Eqs. 3.13 and

3.14, from which we can calculate single scattering albedo and asymmetry parameter simultaneously. Then we use these aerosol properties ($\omega_\lambda,\ g_\lambda, \tau_\lambda$) at five wavelengths (415, 500, 615, 673 and 870 nm) and a two-stream radiation transfer model explained below in section 3.4 to obtain a model value of the *DDR*. We iterate the value of m_λ for each wavelength until the difference between the model *DDR* values form retrieval and observed *DDR* values from MFRSR are less than 5% for each wavelength. The schematic for the determination of single scattering albedo and asymmetry parameter using the best fit of modeled *DDR* to measured *DDR* is given below Fig. 3.3. For modeled *DDR*, we use the two stream radiation transfer model.

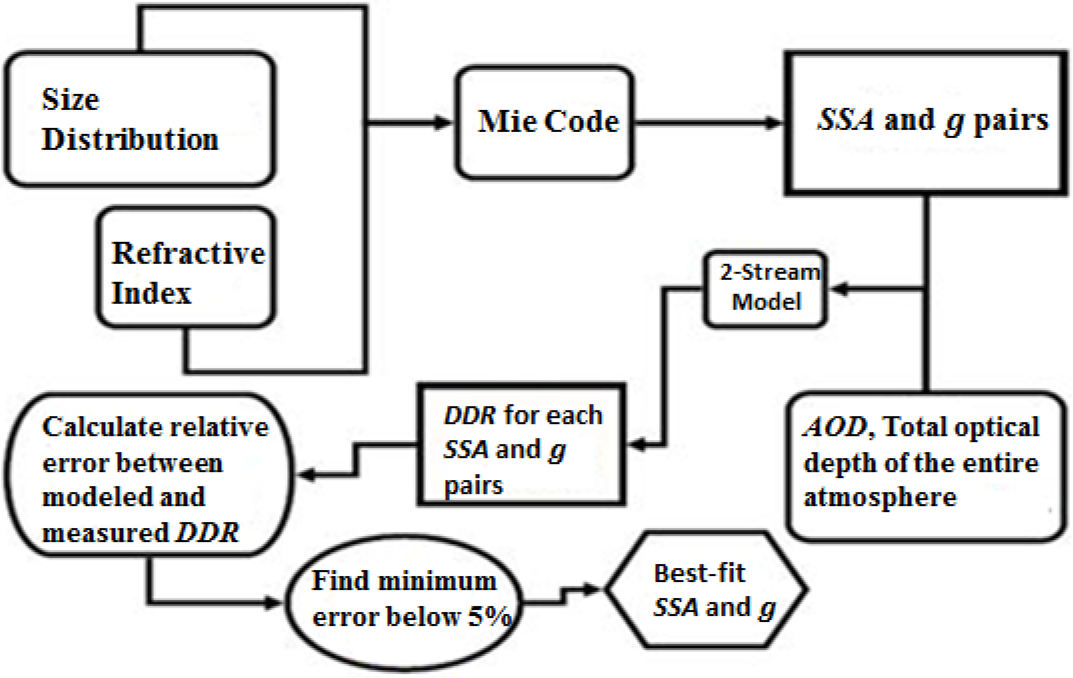

Figure 3.3 Schematics for the estimation of the single scattering albedo and asymmetry parameter (modified from Chelsea A. Corr and Science 2008).

3.4 Two Stream Radiative Transfer Model

The two stream model is an approximation of the radiative transfer equation in which radiation is propagating in only two directions, up and down. The studies of two stream radiative transfer have centered on the atmospheric problems such as the effects on planetary albedos of haze and clouds (Sagan and Pollack 1967, Lyzenga 1973), transfer of solar irradiance through cirrus cloud layers (Liou 1973), transfer of solar irradiance through vertically inhomogeneous turbid atmospheres (Shettle and Weinman 1970, Liou, 2002) and climatic effects of aerosols (Rasool and Schneider 1971). In our research, we are focused on the transfer of the solar irradiance through the inhomogeneous atmosphere. The radiative transfer equation in terms of Legendre polynomials (Liou, 2002) assuming azimuthal symmetry can be written as:

$$\mu_i \frac{dI(\tau,\mu_i)}{d\tau} = I(\tau,\mu_i) - \frac{\omega}{2}\sum_{l=0}^{N} \omega_l\, P_l(\mu_i) \sum_{j=-n}^{n} a_j\, P_l(\mu_j) -$$

$$\frac{\omega}{4\pi}\sum_{l=0}^{N}(-1)^l \omega_l P_l(\mu_i)\, P_l(\mu_0) F_0 e^{-\tau/\mu_0} \quad , \tag{3.16}$$

where $\omega_l = \frac{2l+1}{2}\int_{-1}^{1} P(cos\Theta)\, P_l(cos\Theta)\, dcos\Theta \quad ,$ (3.17)

$i = -n, n$, ω is the single scattering albedo, τ is total optical depth, P_l is Legendre polynomials, F_0 is the incident solar irradiance on the top of atmosphere, $P(cos\Theta)$ is phase function , Θ is the scattering angle, and $\mu_i(-n,n)$ is the direction cosine of radiation streams.

In a two stream model, we take only two streams (i.e. $j = -1$ and $j = 1$) and $N = 1$. The other values are $\mu_1 = 1/\sqrt{3}$, $a_1 = 1$ and $a_{-1} = 1$. Denote $I^{\uparrow} = I(\tau,\mu_1)$ and $I^{\downarrow} = I(\tau,-\mu_1)$ as the up and downwelling irradiance and rearrange the above equation. Then Eq. 3.16 splits into two equations (Liou, 2002):

$$\mu_1 \frac{d\mathrm{I}^{\uparrow}}{d\tau} = \mathrm{I}^{\uparrow} - \omega(1-b)\mathrm{I}^{\uparrow} - \omega b \mathrm{I}^{\downarrow} - S^{-}\, e^{-\tau/\mu_0} \quad , \tag{3.18}$$

and

$$\mu_1 \frac{d\mathrm{I}^{\downarrow}}{d\tau} = \mathrm{I}^{\downarrow} - \omega(1-b)\mathrm{I}^{\downarrow} - \omega b \mathrm{I}^{\uparrow} - S^{+}\, e^{-\tau/\mu_0} \ , \tag{3.19}$$

where

$$S^{\pm} = \frac{F_0 \omega}{4\pi}(1 \pm 3\, g\, \mu_0 \mu_1) \quad , \tag{3.20}$$

$$g = \frac{\omega}{3} = \frac{1}{2}\int_{-1}^{1} P(cos\Theta)\, cos\Theta \;\; dcos\Theta \quad , \tag{3.21}$$

$$b = \frac{1-g}{2} = \frac{1}{2}\int_{-1}^{1} P(cos\Theta)\, \frac{(1-cos\Theta)}{2} \;\; dcos\Theta \quad , \tag{3.22}$$

Here the parameters b and $(1-b)$ can be taken as the integrated fractions of energy backscattered and forward scattered, respectively. Thus, the multiple scattering contributions in the context of the two stream approximation are represented by the upward and downward irradiances (Liou, 2002).

Eq. 3.18 and Eq. 3.19 are the first order inhomogeneous differential equations for the upward and downward irradiances. The solutions of these equations are determined by considering $P = \mathrm{I}^{\uparrow} + \mathrm{I}^{\downarrow}$ and $Q = \mathrm{I}^{\uparrow} - \mathrm{I}^{\downarrow}$. After adding and subtracting these two equations, we find two equations, which are given as below (Liou, 2002):

$$\mu_1 \frac{dP}{d\tau} = (1-\omega g)Q - (S^{-} - S^{+})\, e^{-\tau/\mu_0} \quad , \tag{3.23}$$

and

$$\mu_1 \frac{dQ}{d\tau} = (1-\omega)P - (S^{-} + S^{+})\, e^{-\tau/\mu_0} \quad . \tag{3.24}$$

These two equations are first order differential equations. To find the solutions of these equations, at first, we fist differentiate these two equations with respect to τ.

$$\mu_1 \frac{d^2P}{d\tau^2} = (1-\omega g)\frac{dQ}{d\tau} + \frac{(S^- - S^+)}{\mu_0} e^{-\tau}/\mu_0 \quad , \tag{3.25}$$

and

$$\mu_1 \frac{d^2Q}{d\tau^2} = (1-\omega)\frac{dP}{d\tau} + \frac{(S^- + S^+)}{\mu_0} e^{-\tau}/\mu_0 \quad . \tag{3.26}$$

Then, using the Eq. 3.23 and Eq. 3.24 in Eq. 3.25 and Eq. 3.26, respectively, we find that

$$\frac{d^2P}{d\tau^2} = k^2P + X_1\, e^{-\tau}/\mu_0 \quad , \tag{3.27}$$

and

$$\frac{d^2Q}{d\tau^2} = k^2Q + X_2\, e^{-\tau}/\mu_0 \quad , \tag{3.28}$$

where the eigenvalue k^2 and parameters X_1 and X_2 are given below

$$k^2 = \frac{(1-\omega)(1-\omega g)}{\mu_1^2} \quad , \tag{3.29}$$

$$X_1 = \frac{(S^- + S^+)(1-\omega g)}{\mu_1^2} + \frac{(S^- - S^+)}{\mu_0\mu_1} \quad , \tag{3.30}$$

$$X_2 = \frac{(S^- - S^+)(1-\omega)}{\mu_1^2} + \frac{(S^- + S^+)}{\mu_0\mu_1} \quad . \tag{3.31}$$

The second order differential Eqs. 3.27 and 3.28 can be solved by adding the homogeneous solution and particular solution. After analysis, the solution of above equations produce upward and downward intensities of radiation (Liou, 2002).

$$\mathrm{I}^{\uparrow} = K\, v\, e^{k\tau} + H\, u\, e^{-k\tau} + \epsilon\, e^{-\tau}/\mu_0 \quad , \tag{3.32}$$

$$\mathrm{I}^{\downarrow} = K\, u\, e^{k\tau} + H\, v\, e^{-k\tau} + \gamma\, e^{-\tau}/\mu_0 \quad . \tag{3.33}$$

In these equation unknowns v, u, k, ϵ and γ are defined as:

$$v = \frac{(1+a)}{2}, \qquad u = \frac{(1-a)}{2} \quad , \tag{3.34}$$

$$a^2 = \frac{(1-\omega)}{(1-\omega g)} \quad , \qquad k^2 = \frac{(1-\omega)(1-\omega g)}{\mu_1^2}, \tag{3.35}$$

$$\epsilon = \frac{\alpha+\beta}{2}, \qquad \gamma = \frac{(\alpha-\beta)}{2} \quad , \tag{3.36}$$

$$\alpha = \frac{X_1 \mu_0^2}{(1-\mu_0^2 k^2)}, \qquad \beta = \frac{X_2 \mu_0^2}{(1-\mu_0^2 k^2)} \quad . \tag{3.37}$$

The values of the unknown coefficients K and H are determined by using boundary conditions at top and bottom of the atmospheric layer. We assume no diffuse components at the top and bottom of the atmosphere. We then have the constants K and H as given below:

$$K = \frac{-\left(\epsilon\, v\, e^{-\tau_1/\mu_0} - \gamma\, u\, e^{-k\tau_1}\right)}{\left(v^2\, e^{k\tau_1} - u^2 e^{-k\tau_1}\right)} \quad , \tag{3.38}$$

and

$$H = \frac{(\epsilon\, u\, e^{-\tau_1/\mu_0} - \gamma\, v\, e^{k\tau_1})}{(v^2\, e^{k\tau_1} - u^2 e^{-k\tau_1})} \quad . \tag{3.39}$$

The upward diffuse irradiance and downward diffuse irradiance are evaluated by using two relations $F_{diff}^{\uparrow}(\tau) = 2\pi\mu_1 I^{\uparrow}$ and $F_{diff}^{\downarrow}(\tau) = 2\pi\mu_1 I^{\downarrow}$. Using Eq. 3.32 and Eq. 3.33, the total upward diffuse irradiance and total downward diffuse irradiance are given by

$$F_{diff}^{\uparrow}(\tau) = 2\pi\mu_1\left(K\, v\, e^{k\tau} + H\, u\, e^{-k\tau} + \epsilon\, e^{-\tau/\mu_0}\right) \quad , \tag{3.40}$$

and

$$F_{diff}^{\downarrow}(\tau) = 2\pi\mu_1(K\, u\, e^{k\tau} + H\, v\, e^{-k\tau} + \gamma\, e^{-\tau/\mu_0}) \quad . \tag{3.41}$$

Direct solar irradiance (also referred to as direct normal irradiance) is a measure of the rate of solar energy arriving at the earth's surface from the sun's direct beam, on a plane perpendicular to the beam. The normal component of direct solar irradiance is given by (Joseph, Wiscombe, and Weinman 1976).

$$F_{direct}^{\downarrow}(\tau) = F_0\, e^{-\tau/\mu_0} \quad . \tag{3.42}$$

The total (global) irradiance is the sum of downward diffuse irradiance and downward direct normal irradiance, i.e.

$$F_{total}^{\downarrow}(\tau) = F_{diff}^{\downarrow}(\tau) + F_{direct}^{\downarrow}(\tau) \quad . \tag{3.43}$$

The diffuse to direct ratio (*DDR*) is a powerful tool as an indicator of atmospheric conditions and can provide information of aerosol properties (Krotkov 2005). The diffuse to direct solar irradiance ratios are used for retrieving aerosol *SSA* and g under a variety of atmospheric conditions (Petters 2003). To estimate model values of *DDR*, we use diffuse downward irradiance and diffuse direct normal irradiance.

$$DDR(\tau) = \frac{F_{diff}^{\downarrow}(\tau)}{F_{direct}^{\downarrow}(\tau)} \quad . \tag{3.44}$$

The diffuse downward irradiance ($F_{diff}^{\downarrow}$) and diffuse direct normal irradiance ($F_{direct}^{\downarrow}$) are taken from Eqs. 3.41 and 3.42 given above.

3.5 Direct Aerosol Radiative Forcing

The radiative forcing concept was introduced to account for changes in the solar radiation fluxes due to changes in the atmospheric constituents. The aerosol radiation forcing at any level in the atmosphere is defined as the difference in the net solar flux (down minus up) with and without aerosol, keeping all other parameters constant. In the present case the direct aerosol radiation forcing (*DARF*) has been estimated in terms of Wm^{-2} at the surface and top of the atmosphere. The difference of the two therefore gives the *DARF* in the whole atmosphere. The globally averaged top of atmosphere *DARF* was calculated by using the expression (Charlson et al. 1992) as below:

$$\Delta F = -\frac{S}{4} T^2 \, (1 - N)(1 - a)^2 \, (2 \, \beta \, \tau_{sca}) \; , \tag{3.45}$$

where, S is solar constant, T is transmittance of the atmosphere above the aerosol layer, N is fraction of sky covered by clouds, a is surface albedo, β is fraction of radiation scattered by aerosol, and τ_{sca} is the scattering optical depth. The surface albedo is the ratio of reflected radiation from the surface to the radiation incident upon the surface. Its value varies from zero to one. The optical properties in Eq. 3.45 are at a wavelength of 550 nm. The above expression gives the radiative forcing due to the change of reflectance of the earth aerosol system. It is modified to more general form valid also for absorbing aerosol (Chylek and Wong 1995),

$$\Delta F = -\frac{S}{4} T^2 \, (1-N)[(1-a)^2 \, (2\, \beta \, \tau_{sca}) - 4\, a \, \tau_{abs}] \qquad , \tag{3.46}$$

where τ_{abs} is absorption optical depth. Since, total optical depth $(\tau) = \tau_{abs} + \tau_{sca}$, then the single scattering albedo in term of optical depths is given by $\omega = \tau_{sca}/\tau$, and, the scattering and absorption optical depths are $\tau_{sca} = \omega\tau$ and $\tau_{abs} = \tau(1-\omega)$. Also, the fraction of radiation scattered by aerosol is $\beta = \frac{(1-g)}{2}$. Using τ_{sca}, τ_{abs} and β in above expression for direct radiative forcing becomes:

$$\Delta F = -\frac{S}{4} T^2 \, (1-N) \, \tau \, [(1-a)^2 \, (1-g)\omega - 4\, a \, (1-\omega)] \ . \tag{3.47}$$

The parameters required for *DARF* estimations are the total optical depth (τ), single scattering albedo (ω), asymmetry parameter (g), surface albedo (a), and other constants (S, T and N). For optical depth we use the MFRSR aerosol optical depth measurements, and for the single scattering albedo and asymmetry parameter, we use the values from the *DDR* retrievals.

3.6 References of Chapter 3

Charlson, R. J., S. E. Schwartz, J. M. Hales, R. D. Cess, J. A. Coakley, J. E. Hansen, and D. J. Hofmann. 1992. “Climate Forcing by Anthropogenic Aerosols.” *Science* 255 (5043): 423–30. doi:10.1126/science.255.5043.423.

Chylek, Petr, and J. Wong. 1995. “Effect of Absorbing Aerosols on Global Radiation Budget.” *Geophysical Research Letters* 22 (8): 929–31. doi:10.1029/95GL00800.

Corr, C. A., N. Krotkov, S. Madronich, J. R. Slusser, B. Holben, W. Gao, J. Flynn, B. Lefer, and S. M. Kreidenweis. 2009. “Retrieval of Aerosol Single Scattering Albedo at Ultraviolet Wavelengths at the T1 Site during MILAGRO.” *Atmos. Chem. Phys.* 9 (15): 5813–27. doi:10.5194/acp-9-5813-2009.

Corr, Chelsea A., and Colorado State University Department of Atmospheric Science. 2008. *Retrieval of Aerosol Single Scattering Albedo at UV Wavelengths for Two Urban Field Campaigns*. Colorado State University.

Dubovik, Oleg, Brent Holben, Thomas F. Eck, Alexander Smirnov, Yoram J. Kaufman, Michael D. King, Didier Tanré, and Ilya Slutsker. 2002. “Variability of Absorption and Optical Properties of Key Aerosol Types Observed in Worldwide Locations.” *Journal of the Atmospheric Sciences* 59 (3): 590–608. doi:10.1175/1520-0469(2002)059<0590:VOAAOP>2.0.CO;2.

Ge, J. M., J. Su, T. P. Ackerman, Q. Fu, J. P. Huang, and J. S. Shi. 2010. “Dust Aerosol Optical Properties Retrieval and Radiative Forcing over Northwestern China during the 2008 China-U.S. Joint Field Experiment.” *Journal of Geophysical Research: Atmospheres* 115 (D7): n/a–n/a. doi:10.1029/2009JD013263.

Joseph, J. H., W. J. Wiscombe, and J. A. Weinman. 1976. “The Delta-Eddington Approximation for Radiative Flux Transfer.” *Journal of the Atmospheric Sciences* 33 (12): 2452–59. doi:10.1175/1520-0469(1976)033<2452:TDEAFR>2.0.CO;2.

Kassianov, E. I., C. J. Flynn, T. P. Ackerman, and J. C. Barnard. 2007. “Aerosol Single-Scattering Albedo and Asymmetry Parameter from MFRSR Observations during the ARM Aerosol IOP 2003.” *Atmospheric Chemistry & Physics* 7: 3341–51.

Kassianov, Evgueni I., James C. Barnard, and Thomas P. Ackerman. 2005. “Retrieval of Aerosol Microphysical Properties Using Surface MultiFilter Rotating Shadowband Radiometer (MFRSR) Data: Modeling and Observations.” *Journal of Geophysical Research: Atmospheres* 110 (D9): n/a–n/a. doi:10.1029/2004JD005337.

Liou, Kuo-Nan. 1973. “Transfer of Solar Irradiance through Cirrus Cloud Layers.” *Journal of Geophysical Research* 78 (9): 1409–18. doi:10.1029/JC078i009p01409.

Liou, K. N. 2002. *An Introduction to Atmospheric Radiation*. Amsterdam; Boston: Academic Press.

Lyzenga, D.R. 1973. “Note on the Modified Two-Stream Approximation of Sagan and Pollack.” *Icarus* 19 (2): 240–43. doi:10.1016/0019-1035(73)90127-9.

Nickolay Krotkov, Pawan K. Bhartia. 2005. “Aerosol Ultraviolet Absorption Experiment (2002 to 2004), Part 2: Absorption Optical Thickness, Refractive Index, and Single Scattering Albedo.” *Optical Engineering - OPT ENG* 44 (4). doi:10.1117/1.1886819.

Pandithurai, G., S. Dipu, K. K. Dani, S. Tiwari, D. S. Bisht, P. C. S. Devara, and R. T. Pinker. 2008. “Aerosol Radiative Forcing during Dust Events over New Delhi, India.” *Journal of Geophysical Research: Atmospheres* 113 (D13): n/a–n/a. doi:10.1029/2008JD009804.

Petters, J. L. 2003. “Aerosol Single Scattering Albedo Retrieved from Measurements of Surface UV Irradiance and a Radiative Transfer Model.” *Journal of Geophysical Research* 108 (D9). doi:10.1029/2002JD002360. http://adsabs.harvard.edu/abs/2003JGRD..108.4288P.

Rasool, S. I., and S. H. Schneider. 1971. “Atmospheric Carbon Dioxide and Aerosols: Effects of Large Increases on Global Climate.” *Science* 173 (3992): 138–41. doi:10.1126/science.173.3992.138.

Sagan, Carl, and James B. Pollack. 1967. “Anisotropic Nonconservative Scattering and the Clouds of Venus.” *Journal of Geophysical Research* 72 (2): 469–77. doi:10.1029/JZ072i002p00469.

Seinfeld, John H, and Spyros N Pandis. 2006. *Atmospheric Chemistry and Physics: From Air Pollution to Climate Change*. Hoboken, N.J.: J. Wiley.

Shettle, E. P., and J. A. Weinman. 1970. “The Transfer of Solar Irradiance Through Inhomogeneous Turbid Atmospheres Evaluated by Eddington’s Approximation.” *Journal of the Atmospheric Sciences* 27 (7): 1048–55. doi:10.1175/1520-0469(1970)027<1048:TTOSIT>2.0.CO;2.

Chapter 4 Aerosol Optical Depth (*AOD*), Ångström Exponent (*AE*) and Volume Size Distribution Case Studies

4.1 Introduction

Aerosol Optical Depth (*AOD*) is the measure of aerosols (e.g. smoke particles, desert dust, sea salt, urban haze) distributed within a column of air as measured at the Earth's surface to the top of the atmosphere. Total atmospheric optical depth consists of scattering and absorption by gases, aerosol, and clouds (Seinfeld and Pandis 1998).

Aerosol measurements are carried out worldwide in order to reduce the uncertainties in the impact of aerosols on climate (Smithson 2002). Different types of measurements (ground based, satellite, or aircraft) are accomplished to study aerosol optical properties. The AERONET (Aerosol Robotic Network) project started in 1990s aiming to monitor the aerosol properties using a Cimel sun photometer. Another instrument, the Multi-filter Rotating Shadow-band Radiometer (MFRSR), provides routine measurements of the aerosol optical depth at six wavelengths (415, 500, 615, 673, 870 and 940 nm).

The Ångström exponent (*AE*) given in Eq. 2.18 of Chapter 2 expresses the spectral dependence of aerosol optical thickness (τ) with the wavelength of incident light (λ). The *AE* helps to characterize the particle size and type in the atmosphere (Ångström 1929). It is an indirect calculation of the aerosol size. In general, when the *AE* is less than 1, coarse mode particles dominate, and when the *AE* is greater than 1, fine mode particles are abundant in the atmosphere (Queface et al. 2003). The main sources of fine mode particles are incomplete combustion of wood, coal, gasoline and other fuels. The sources of coarse mode particles are sea salt, dust, soil and biological particles, suspended in atmosphere. To estimate the fine and coarse mode contributions during smoky, dusty and clear sky days, we use the volume size distribution retrieval explained in chapter 3 and *AODs* derived from MFRSR retrieval explained in chapter 2 at different five wavelengths (415, 500, 615,673 and 870 nm).

4.2 California Rim Fire on August - September, 2013

The Rim fire that started on August 17, 2013 was the third largest wildfire in California's history. The fire burned 257,314 acres (1,041.31 km^2), and was the biggest wildfire on record in the Sierra Nevada Mountains. The fire was caused by a hunter's illegal fire that went out of control and was named for its proximity to the Rim of world vista point in the Stanislaus National Forest (http://en.wikipedia.org/wiki/Rim_Fire#cite_note-10). The red line of Fig. 4.1 indicates the perimeter affected by the Rim fire on September 1, 2013. The pink line was the perimeter two days earlier. The western boundary of Yosemite National Park is shown in green line.

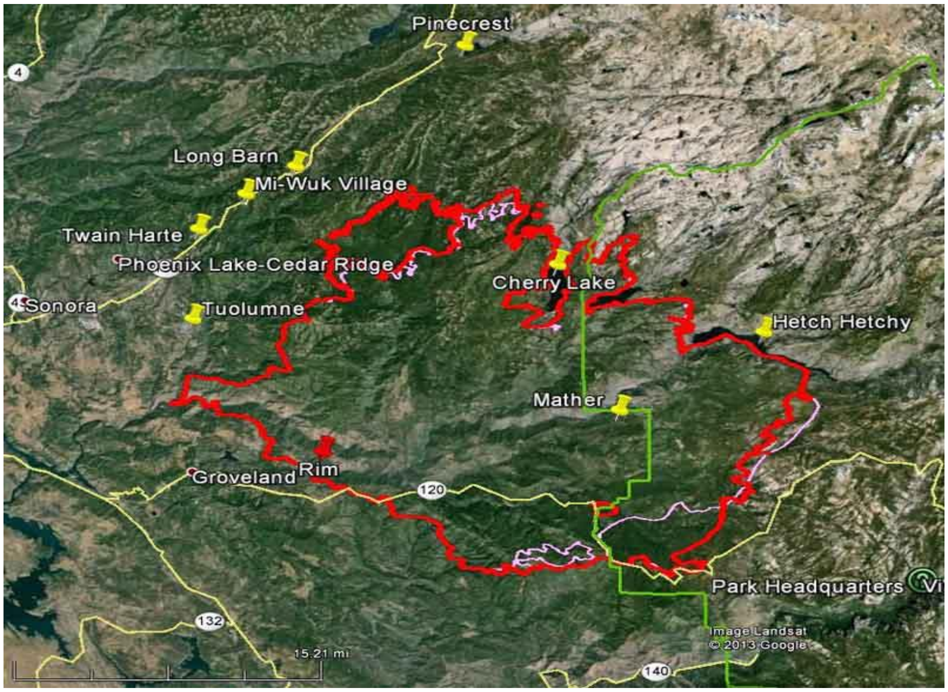

Figure 4.1 Map of the Rim fire: where the red line was the perimeter at 8 p.m., September 1, 2013. (http://wildfiretoday.com/2013/08/21/california-rim-fire-west-of-yosemite-np/).

During the Rim fire, the fire went racing through forests on the western boundary of Yosemite National Park, causing serious air-quality issues around the Lake Tahoe basin, Washoe County, Reno, and Carson City. The NASA satellite photograph given below in Fig. 4.2 shows a huge smoke plume spreading northeast from the Rim fire. For the study of smoke effect on air quality in Reno during Rim fire, we used the MFRSR, the Cimel sun photometer and photoacoustic instruments, located on the roof of the physics building at the University of Nevada Reno (39.5272° N, 119.8219° W).

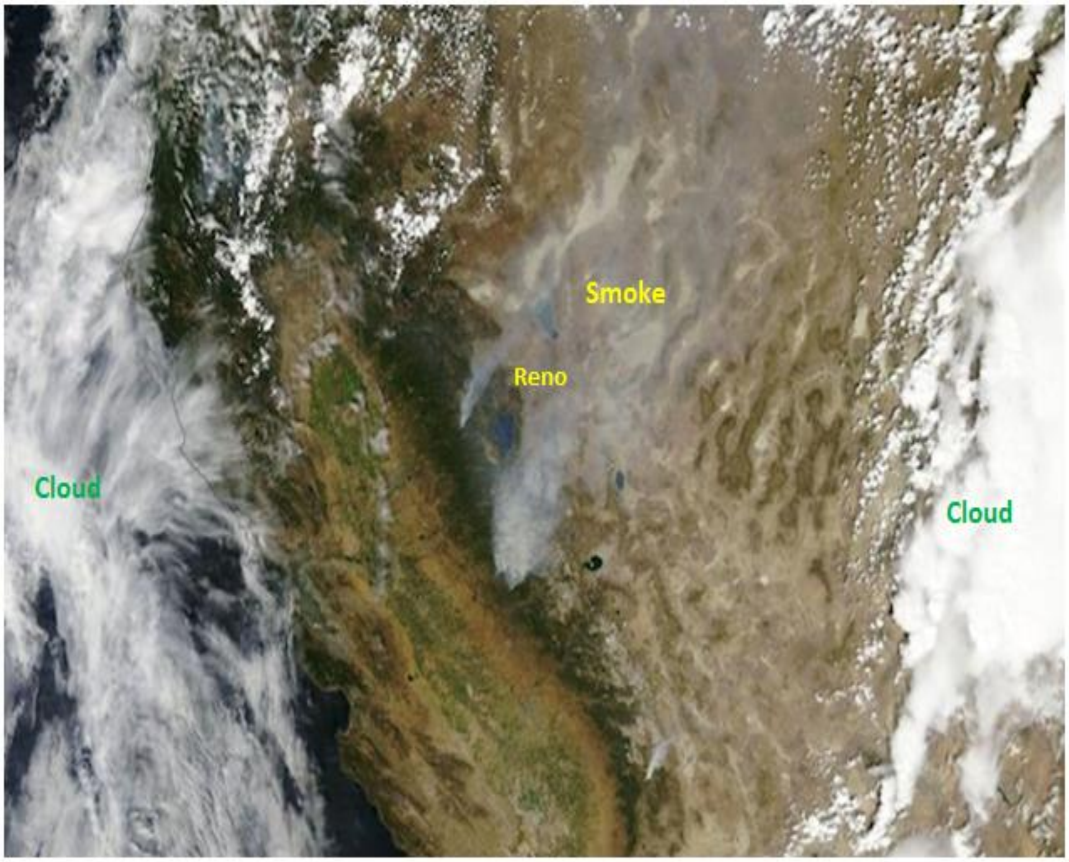

Figure 4.2 NASA satellite image of the smoke from the Rim fire, spreading over Lake Tahoe, Reno, and beyond (http://aarondames.squarespace.com/nature/?currentPage=2).

4.2.1 Aerosol Optical Depth (*AOD*) and Ångström Exponent (*AE*)

We compare our retrieved *AOD* values from the MFRSR with those from the Cimel processed by the AERONET algorithm at 415, 500, 615, 673, and 870 nm wavelengths. The *AOD* measurements suggested that the Rim fire affected the aerosol concentrations in Reno during the fire. Fig. 4.3 and Fig. 4.4 indicate that the time series plots of aerosol optical depth on 23 August and 27 August respectively. On August 23, the maximum *AOD* was 3.26 at 10:15 AM for the 415 nm channel. The values of *AE* during the Rim fire from MFRSR (500/870 nm) and Cimel (440/870 nm) were larger than 2 with uncertainty error ± 0.09 (Fig. 4.5), because of the presence of fine smoke aerosol particles during the fire in August 23, 2013.

The *AOD* at 500 nm and *AE* on August 27 exhibit rapid variability, increasing from 0.81 to 5.13 and from 0.7 to 2.3 respectively. These higher values of *AE* are due to the smoke plume in the atmosphere. It shows that the strongest intensity of the smoke plume was observed on August 27. The *AOD* and *AE* showed temporal variability all day due to the inhomogeneity of the smoke plume. The *AOD* was especially high after the midday, between 12:45 PM and 5:00 PM, remaining larger than 1. In addition, the presence of the smoke plume induced an extremely large *AOD* maximum of 5.13, which was reached at 2:10 PM local time. During the same period, the *AE* remained 2.3, indicating the presence of a significant amount of fine particles. These *AOD* values are about a factor of 100 higher than would be observed on a relatively clean day.

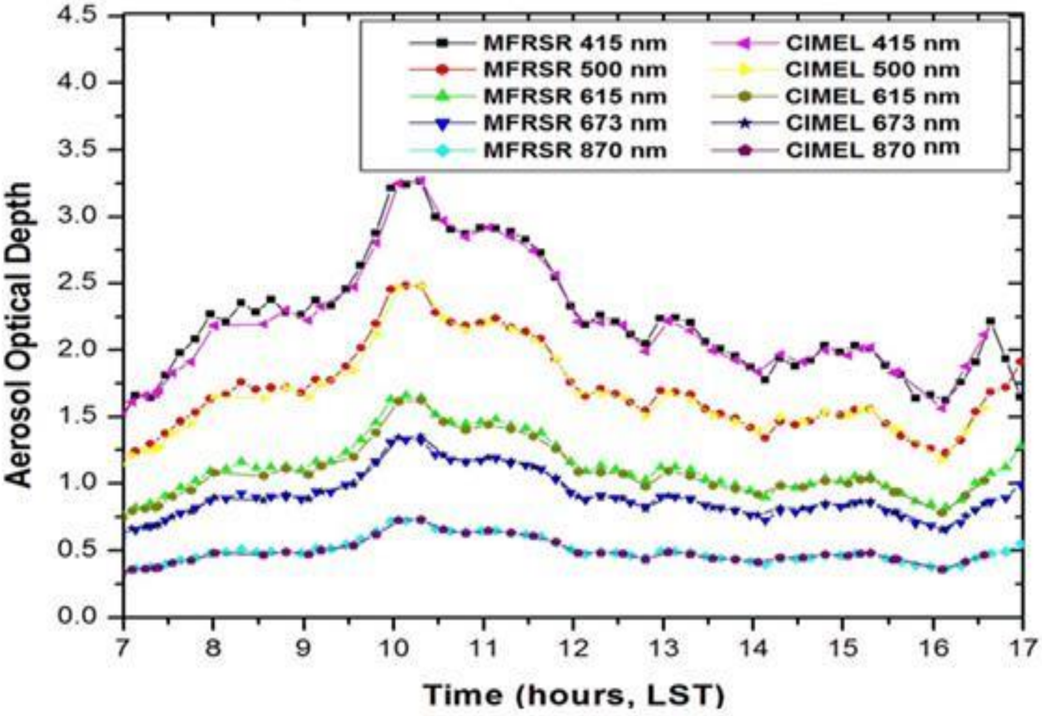

Figure 4.3 Time series comparison of MFRSR and Cimel aerosol optical depth for August 23, 2013 at UNR

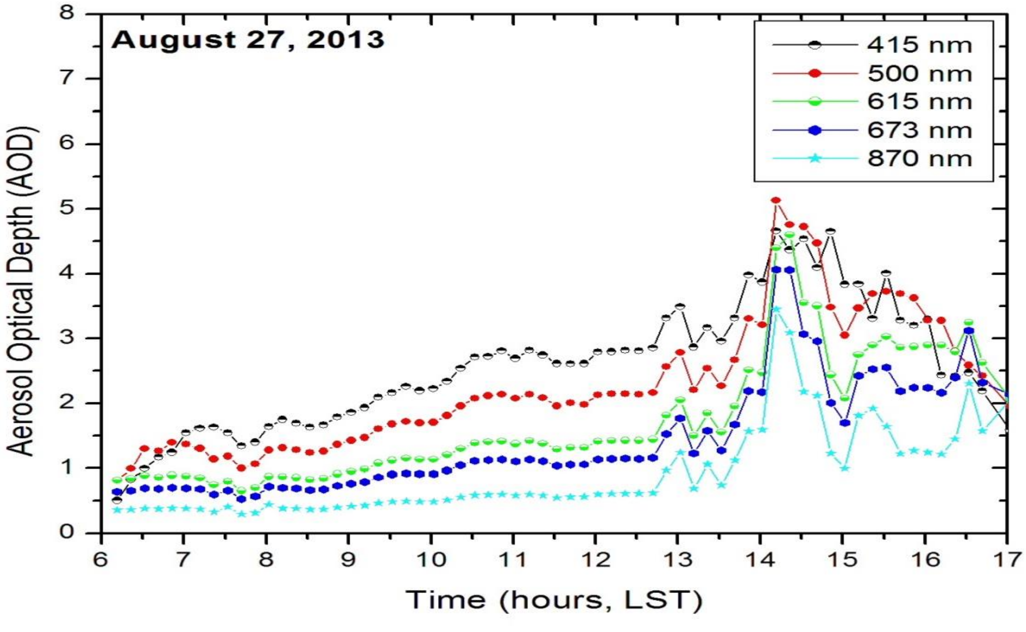

Figure 4.4 Time series of MFRSR aerosol optical depth for August 27, 2013 at UNR.

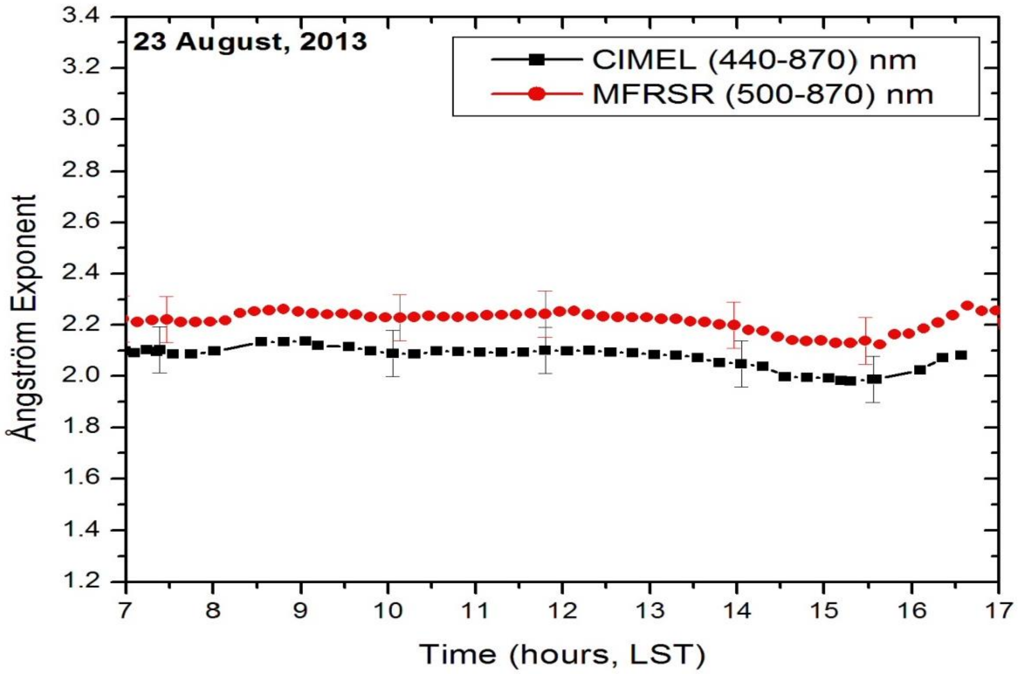

Figure 4.5 Comparison of MFRSR and Cimel Ångström Exponent On August 23, 2013.

For comparison with satellite, we chose the Cimel and MFRSR *AOD* values at 673 nm instead of other wavelengths because we have the *AOD* at a wavelength of 660 nm from satellite observations (Table 4.1 and Table 4.2). The 673 nm channel is nearly common for both ground and satellite observations. The Cimel and MFRSR *AOD* differences range between 0.002 and 0.02, which is within the limit of the calibration accuracy (Holben et al. 1998, Alexandrov et al. 2008).

Satellite observations are an effective way to provide a global coverage of *AOD*. However, satellite aerosol retrievals are complicated by the fact that the upward radiance received by the satellite is composed of light reflected by the surface and atmospheric constituents (Ge et al. 2010). The accurate determination of *AOD* requires separation of radiation reflected by the surface from the total scattered radiation. This procedure is very inaccurate over land because land surface reflectances are often large and vary with location and time (Ge et al. 2010). In this work, we compared the ground based MFRSR and Cimel *AOD* values with satellite based MODIS Terra and Aqua measurements used to retrieve *AOD* using the Dark Target and Deep Blue-Aqua *AOD* retrieval algorithms. The MODIS satellite instruments retrieve *AOD* values from 660 nm channel data, which is close to the 673 nm channel of the surface instruments.

Case	**Local Time**	**MFRSR *AOD***	**Cimel *AOD***	**Terra *AOD***	**MFRSR *AE***	**Cimel *AE***
22 August	11:10	0.10	0.09	0.18	1.50±0.09	1.53±0.08
23 August	11:55	0.93	0.95	1.32	2.05±0.08	2.09±0.07
24 August	12:35	0.51	0.52	0.84	2.13±0.11	2.10±0.10
25 August	11:40	1.17	1.19	1.66	2.15±0.04	2.06±0.02
26 August	12:25	0.27	0.26	0.73	2.25±0.02	2.28±0.03
27 August	11:30	1.03	1.01	1.82	2.30±0.07	2.27±0.08
28 August	12:15	0.70	0.68	1.29	1.99±0.05	2.01±0.10
29 August	11:20	0.07	0.06	0.14	1.85±0.08	1.89±0.04
30 August	12:00	0.27	0.25	0.78	2.29±0.02	2.19±0.04
31 August	12:45	0.06	0.05	0.13	2.03±0.08	2.02±0.03
1 September	11:50	1.50	1.52	1.98	1.82±0.04	1.79±0.02
3 September	11:35	0.20	0.21	0.55	2.43±0.02	2.45±0.06
5 September	11:25	0.07	0.07	0.17	1.98±0.05	1.93±0.09
6 September	12:09	0.05	0.06	0.23	2.10±0.04	1.95±0.05
7September	11:10	0.06	0.05	0.21	2.32±0.08	2.01±0.11

Table 4.1: MFRSR (673 nm), Cimel (673), and Terra MODIS dark target retrieval (660 nm) *AODs* and *AEs* for two cases (MFRSR and Cimel) during some selected days of the Rim fire 2013. The uncertainty for the MFRSR or Cimel measurements is ± 0.01 (Holben et al. 1998), and Terra MODIS dark target retrieval is $\pm(0.05 + 0.15 * AOD)$ (R. C. Levy 2005).

Case	**Local Time**	**MFRSR *AOD***	**Cimel *AOD***	**Aqua *AOD***	**Deep Blue *AOD***
22 August	14:30	1.52	1.48	1.82	1.20
23 August	13:15	0.90	0.88	1.75	1.08
24 August	14:15	0.41	0.40	0.88	0.65
25 August	13:40	0.21	0.19	0.72	0.34
26 August	14:05	0.19	0.19	0.54	0.23
28 August	13:50	0.70	0.67	1.45	0.58
29 August	14:35	0.17	0.16	0.37	0.13
30 August	13:40	0.24	0.26	0.66	0.38
31 August	14:25	0.09	0.09	0.18	0.08
1 September	14:05	1.61	1.58	1.86	1.75
3 September	14:35	0.08	0.09	0.17	0.05
5 September	14:40	0.12	0.13	0.28	0.09
6 September	13:45	0.10	0.09	0.36	0.12
7 September	14:30	0.12	0.11	0.52	0.11

Table 4.2: MFRSR (673 nm), Cimel (673), Aqua MODIS dark-target retrieval algorithm (660 nm) and Deep Blue retrieval algorithm *AODs* (660 nm) during the selected days of the Rim fire 2013. The uncertainty for the MFRSR or Cimel measurements is ± 0.01 (Holben et al. 1998), Aqua MODIS dark-target retrieval algorithm is $\pm(0.05 + 0.15 * AOD)$ (R. C. Levy 2005) and Deep Blue *AOD* retrieval algorithm is $\pm(0.04 + 0.15 * AOD)$ (Shi et al. 2012).

The absolute relative error between the satellite and ground measurements can be defined as (Ge et al. 2010):

$$relative\ error = \left(\frac{|AOD_{satellite} - AOD_{MFRSR}|}{AOD_{MFRSR}}\right) 100\%$$

It is found that, the maximum relative error between MFRSR and Terra MODIS Dark-Target *AOD* is 170% on August 26 and minimum relative error is 32% on September 1, and the satellite retrieved *AOD* is always larger than the MFRSR value. It is likely that the satellite

AOD retrieval algorithm is biased high due to the bright underlying surface, and the algorithm is mostly for vegetated surfaces.

The *AOD* values for two cases August 23 and August 27, 2013 are plotted in Fig. 4.6 and Fig. 4.7 respectively. On August 27, the aerosol loading is higher than August 23. In each case, the MFRSR *AOD* values are close with the Cimel *AOD* values, but the MODIS dark-target *AOD* values are much larger than the MFRSR and Cimel *AOD* values, with maximum exceeding 2.77 in 470 nm channels in August 27.

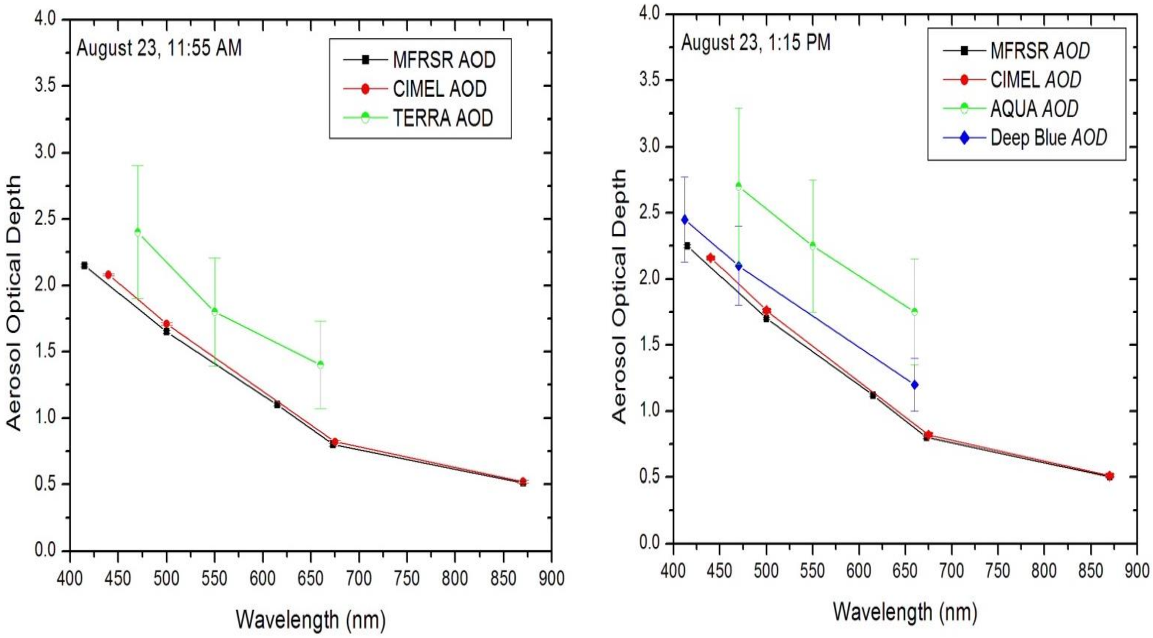

Figure 4.6 Comparison of MFRSR, Cimel, Terra MODIS dark-target, Aqua MODIS dark-target and Deep Blue retrieval *AODs* for August 23, 2013 at UNR.

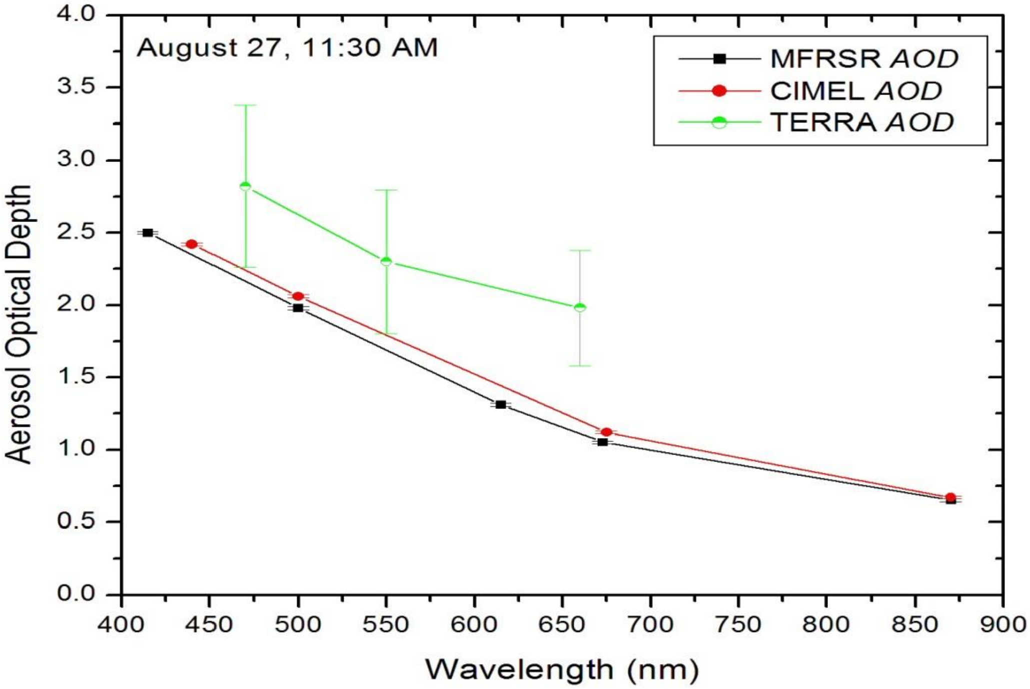

Figure 4.7 Comparison of MFRSR, Cimel and Terra MODIS dark-target *AOD*s for August 23, 2013 at 11:30 AM.

.

Fig. 4.8 shows the scatter plot of the MFRSR and Cimel hourly averaged *AOD* on August 23, 2013 which indicates that the MFRSR and Cimel measured *AOD* values at 500 nm are highly correlated with a R^2 value 0.99. The comparison of ground based measured *AOD* (MFRSR and Cimel) with satellite *AOD* measurements during the Rim fire smoke (August/September) at the time of satellite observation are shown in Figs 4.9 and 4.10. In both plots, the MFRSR and Cimel *AOD* values are close, but the satellite *AOD* values are higher than ground based *AOD* values. Figs.4.11 and 4.12 show the variation of the daily averaged *AOD* during entire month of August 2013 and indicates that the effect of smoke is larger from 22 August and with a maximum value on 27 August.

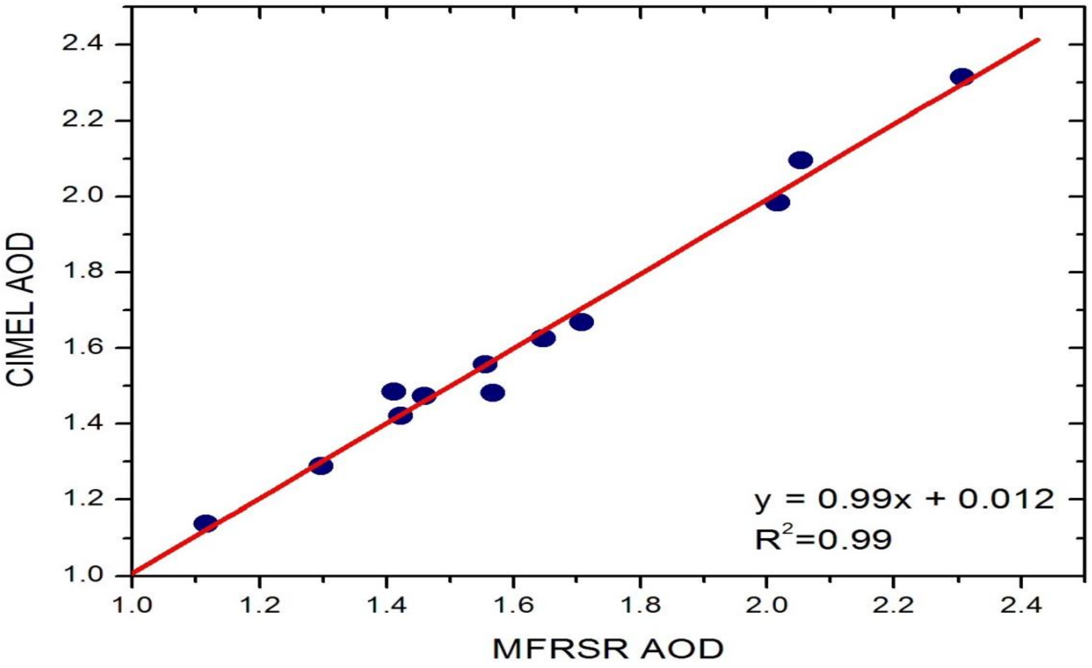

Figure 4.8 Comparison of the MFRSR and Cimel aerosol optical depth for 500 nm on August 23, 2013 at UNR.

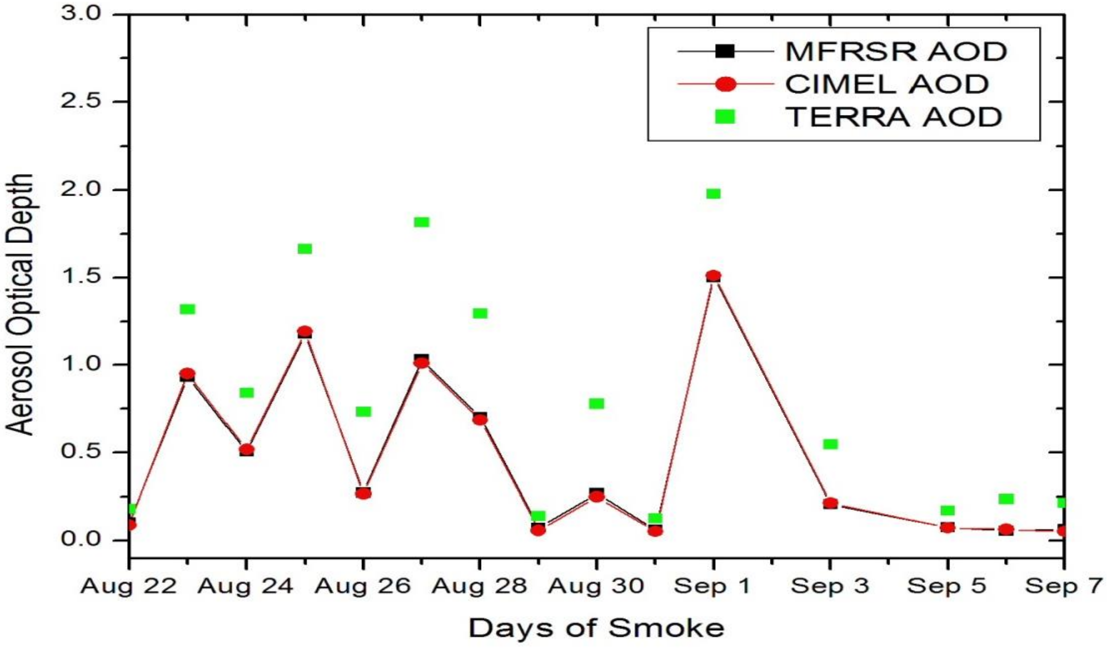

Figure 4.9 Comparison of MFRSR, Cimel and Terra MODIS dark-target *AOD*s during the rim fire, August-September, 2013.

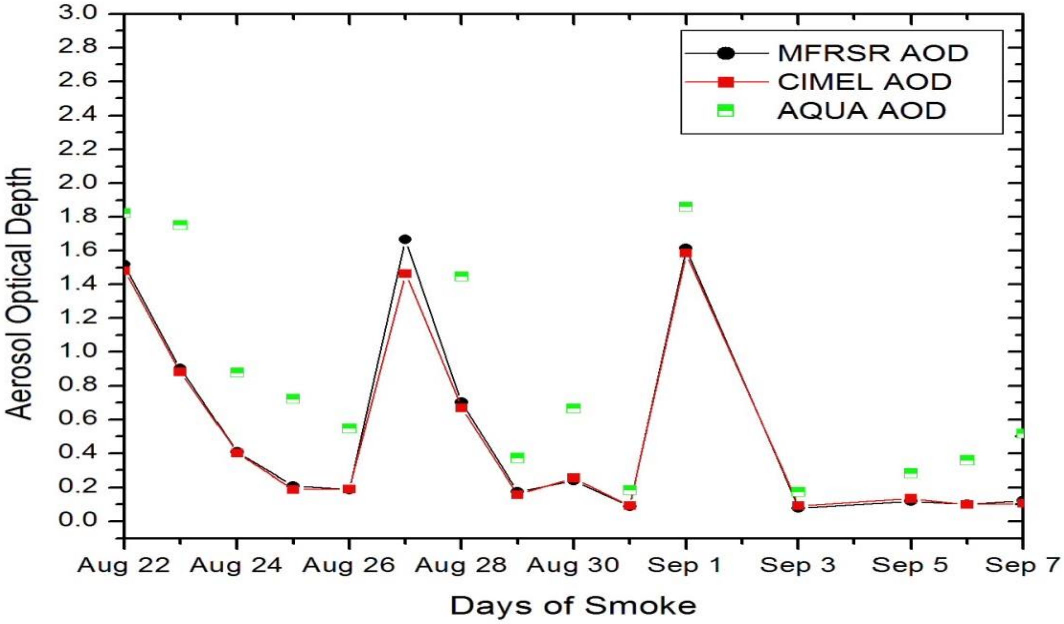

Figure 4.10 Comparison of MFRSR, Cimel and Aqua MODIS dark-target *AOD*s during the Rim fire, August-September, 2013.

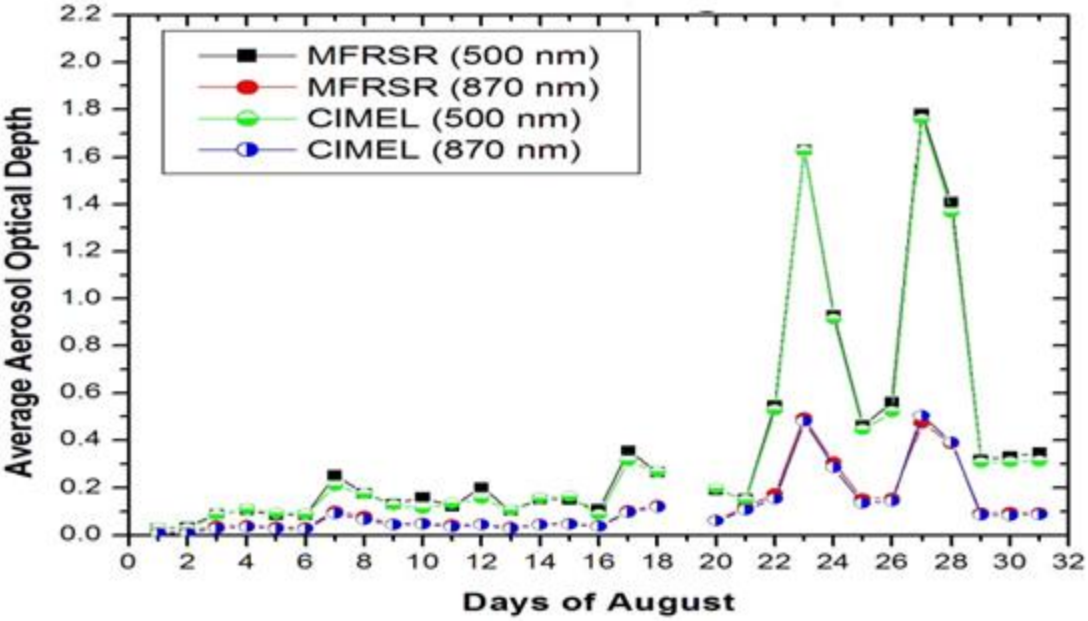

Figure 4.11 Comparison of MFRSR and Cimel aerosol optical depth for 500nm and 870 nm on August 2013.

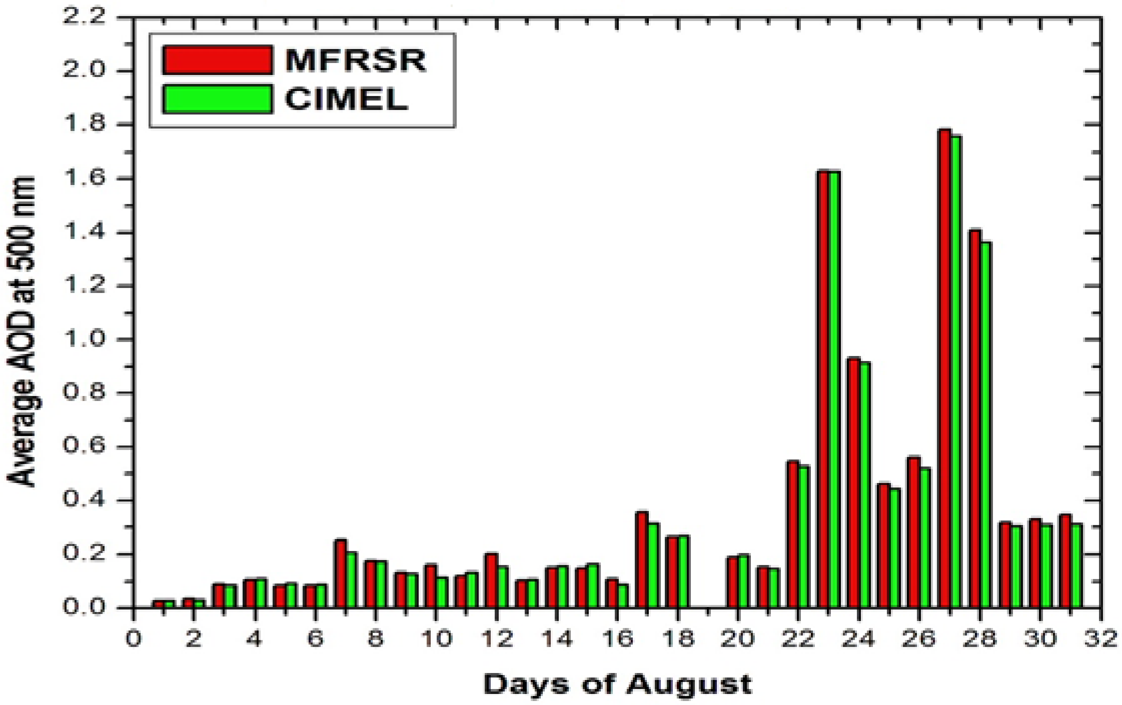

Figure 4.12 Comparison of MFRSR and Cimel aerosol optical depth for 500 nm on August, 2013 at UNR.

4.2.2 Aerosol Volume Size Distribution

The size distributions for all smoky days during the Rim fire are dominated by fine mode aerosol particles. The comparison of the retrieved size distribution using MFRSR and Cimel is shown in Fig. 4.13 (top). On August 23, the values of the fine and coarse modes radii are 0.14 and 2.22 μm respectively. The values of particle volume concentration for fine (C_f) and coarse modes (C_c) are found to be 0.221 and 0.0303 $\mu m^3/\mu m^2$ respectively. These results indicate that the particle sizes of two modes are nearly constant during this period and that the fine mode dominates the coarse mode by about 10:1 using MFRSR data. This is consistent with our observation that the majority of the aerosol particles are smoke. Fig. 4.13 (bottom) shows the wavelength dependence of measured and retrieved (model) values of *AOD*. The measured *AOD* is from MFRSR *AOD* retrieval and model *AOD* is from Mie calculation by using the retrieved aerosol size distribution and refractive index ($\mu = 1.5 + 0.007i$). The plot (Fig. 4.13 bottom) shows that measured and model values of *AOD* are in excellent agreement.

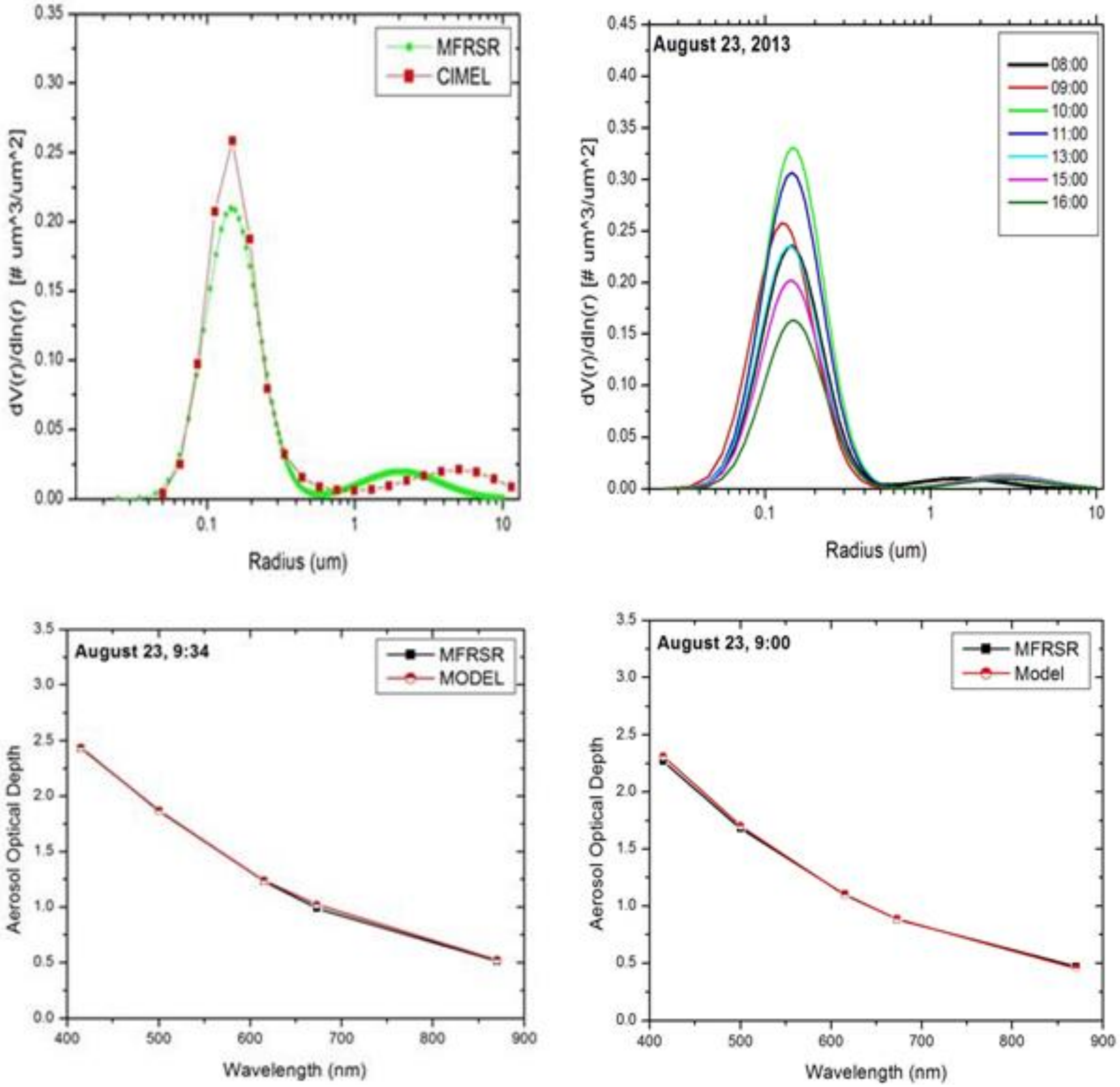

Figure 4.13 (Top) Aerosol size distribution comparison derived from MFRSR and Cimel, and (bottom) the spectrally dependent *AOD* for selected cases derived from the MFRSR data and Mie calculation by using the derived aerosol size distribution and refractive index for August 23, 2013.

4.2.3 Back Trajectories Analysis

In order to understand the origin of the aerosol particles over Reno, the 48-hour back trajectories were calculated by using the HYSPLIT (Hybrid Single Particle Lagrangian Integrated Trajectory). The HYPLIT model was developed by Air Resources Laboratory (*ARL*) of National Oceanic and Atmospheric Administration (*NOAA*). The EDAS (Eta Data Assimilation System) archive uses 40 km, Lambert Conformal Grids for its datasets (McNeal 2008). We chose three different altitudes: near-surface level (500 m from the ground), 1 km from the ground surface, in which majority of the aerosol particles are present, and the 2.5 km level, close to the top of the atmospheric boundary layer.

The HYSPLIT model was used to compute back trajectories for air parcels arriving at the surface of UNR site during the Rim fire 2013. Fig. 4.14 shows the back trajectories for air reaching Reno on August 23 and Fig. 4.15 represents the back trajectories for August 27. Both plots demonstrate that the southerly wind brought the plumes of smoke to Reno from the Rim fire. The bottom panels of both plots show the height of the air mass in meters above ground level. The time chosen for air-mass arrivals is 17:00 UTC on August 23 and 21:00 UTC on August 27 in order to give a more representative pattern for the air masses affecting the study area. The air parcels reaching Reno on these days are from the Rim fire, thus strongly influence on the *AOD* and *AE*.

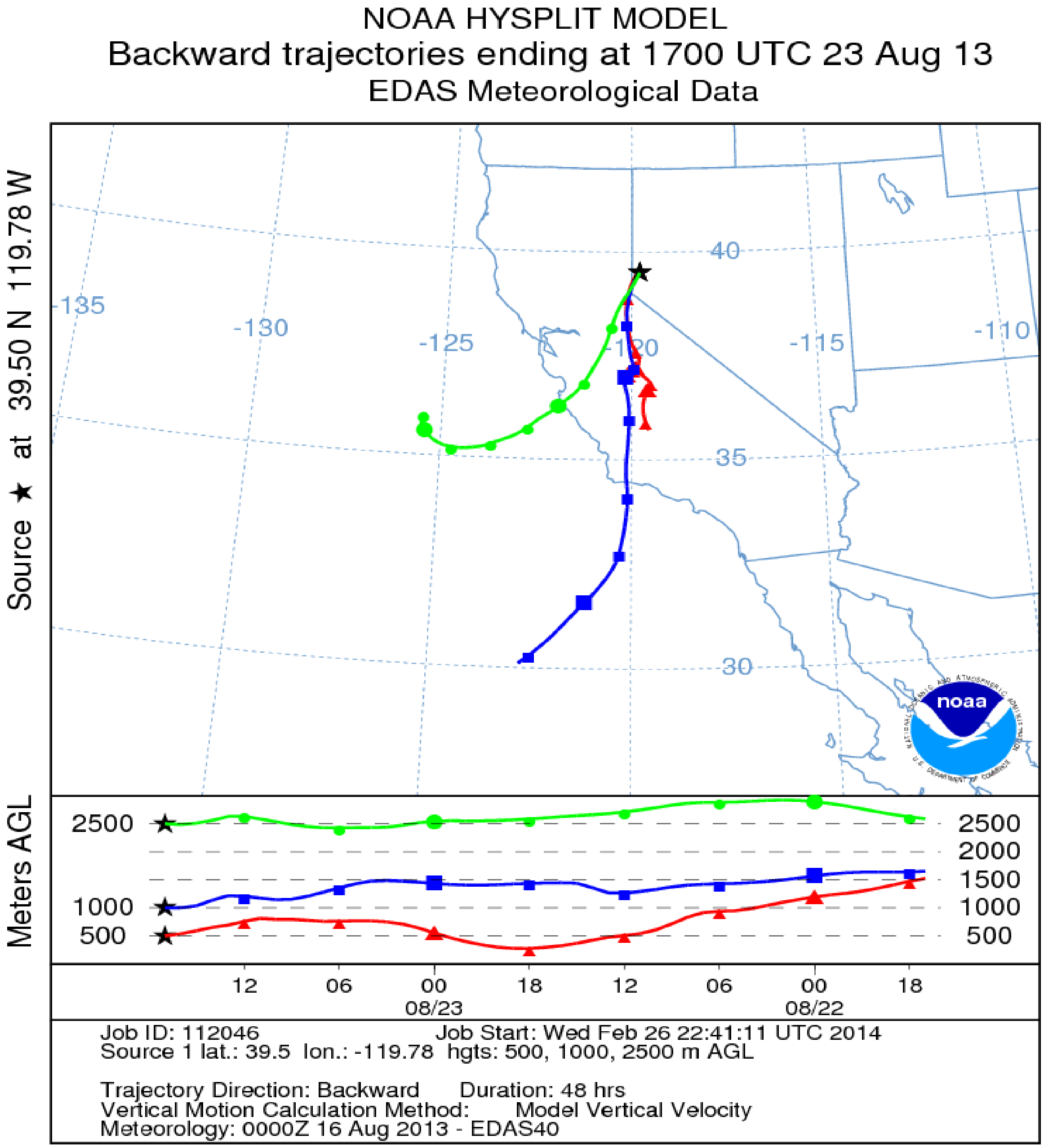

Figure 4.14 48-hours back trajectory from NOAA- HYSPLIT on August 23, 2013 to Reno during the Rim fire.

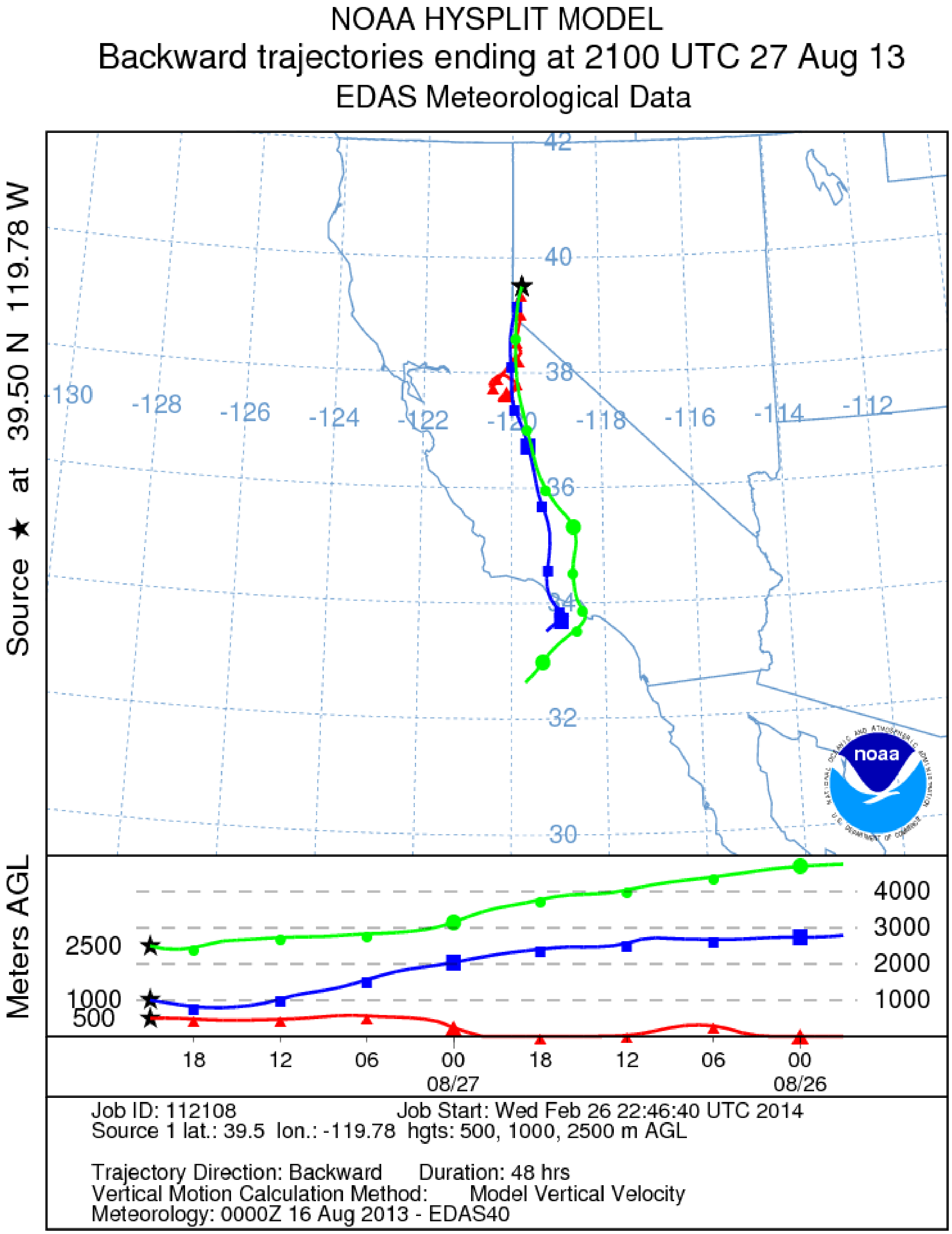

Figure 4.15 48-hours back trajectory from NOAA- HYSPLIT on August 27, 2013 to Reno during the Rim fire.

4.3 Dust Storm on 24 April, 2013 in Reno

Dust storms frequently occur in desert regions of the world, especially during the spring and summer time. In general dust aerosols are emitted from the arid and desert areas around the earth with about 90% of total emission occurring in the Northern Hemisphere, mostly in North Africa (Li, Ginoux, and Ramaswamy 2008). Dust, a major aerosol in the atmosphere, plays an important role in the radiative budget and climate. Solar radiation is absorbed and scattered by dust aerosol as a function of the wavelength. Dust can be associated with large optical depths just as with smoke from wild fires, although dust particles are larger. In April 24, 2013, northeasterly winds were reported at about 16 mph during the evening time of Reno. The winds were picking up dust from the Humboldt sink, blowing it towards the southwest, and hazing the skies over Reno and Sparks into a milky white. The white rings in Fig. 4.16 show forward diffraction by dust particles in Reno at two times on April 24, 2013.

Figure 4.16 Scattering of solar light radiation due to a dust storm on April 24, 2013 at UNR at local times 5:52 PM and 6:24 PM.

4.3.1 Aerosol Optical Depth and Ångström Exponent

Due to dust on April 24, 2013, the *AOD* is higher at evening than in the morning. Based on Fig. 4.17 (top), the values of *AOD* during the dust periods are higher than during the non-dust periods for all wavelengths (415, 500, 615, 673 and 870 nm). However, the values of *AE* at the time of dust are lower than non-dust times as shown in Fig. 4.17 (bottom). The minimum value of *AE* that we found was 0.23 at 2:30 PM local time, indicating that aerosol particles sizes were large at that time.

Fig. 4.18 shows the comparison of the *AOD* using the MFRSR and Cimel during the dust storm for wavelengths 500 nm and 673 nm. The maximum values of *AOD* at 500 nm, during the dust, were found to be 0.19 and 0.21 using MFRSR and Cimel, respectively. However, for 673 nm channel, the maximum values of the AOD were found to be 0.18 and 0.20 using MFRSR and Cimel, respectively, which are about double the non-dust values during the (morning) time on April 24, 2013. The Cimel and MFRSR *AOD* differences during the dust are below the limit of the calibration accuracy 0.02.

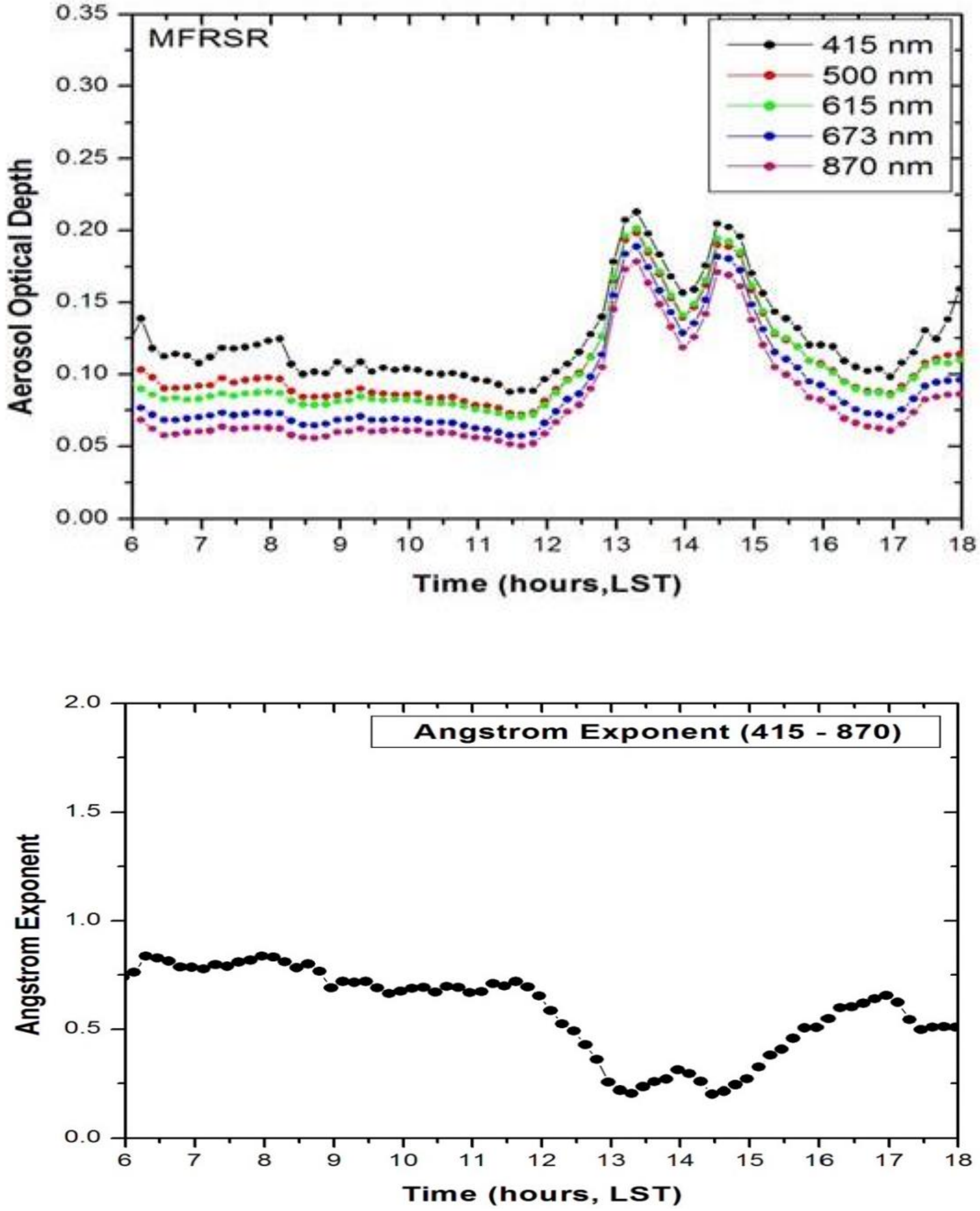

Figure 4.17 Time series of aerosol optical depth and Ångström Exponent for April 24, 2013 at UNR during the dust storm.

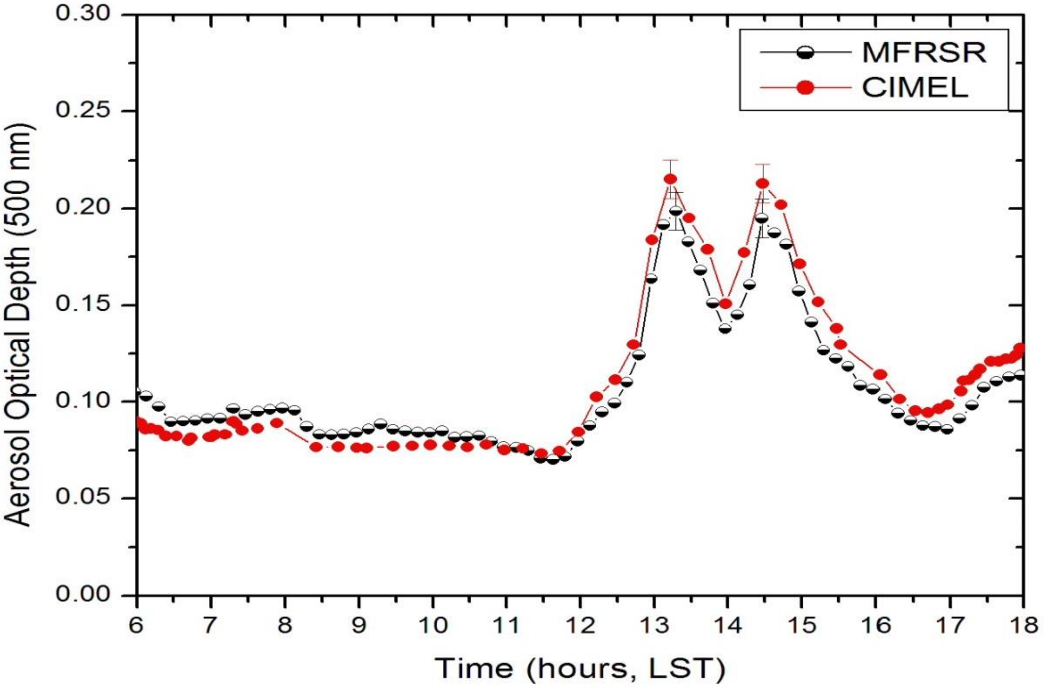

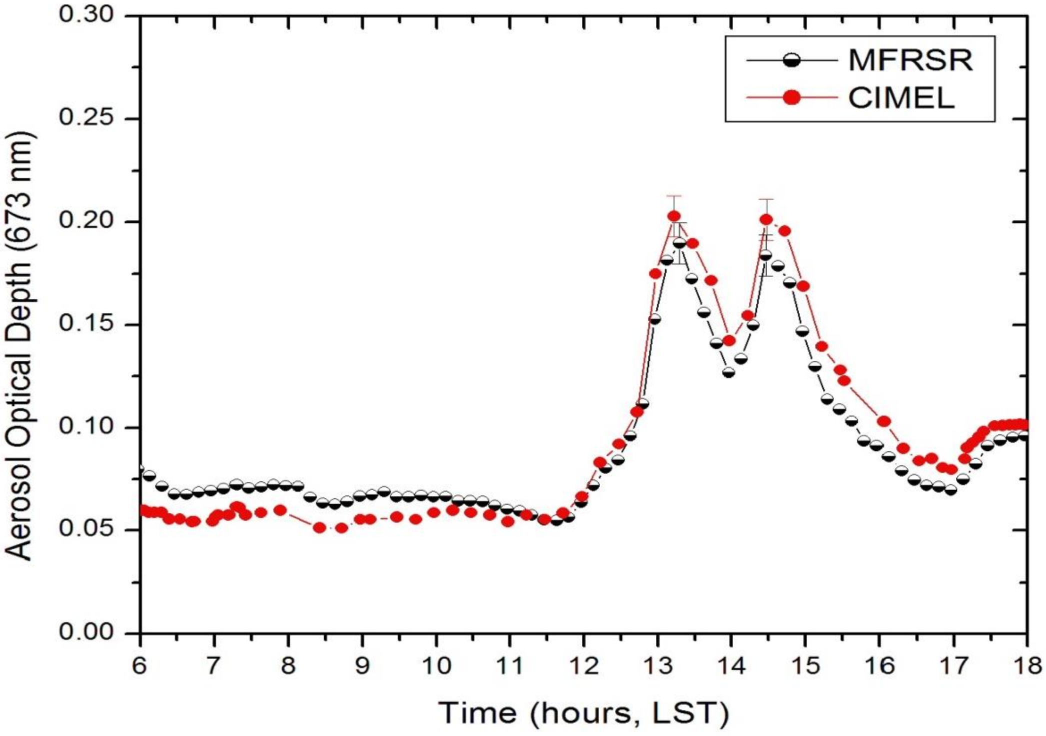

Figure 4.18 Time series comparison of MFRSR and Cimel aerosol optical depth for April 24, 2013 at UNR during the dust storm.

Fig. 4.19 and Fig. 4.20 compare the ground base *AOD* measurements (MFRSR and Cimel) with satellite *AOD* measurements (Terra MODIS, Aqua MODIS and Deep Blue). On April 24, at the time of satellite measurements, the dark-target retrieval-algorithm Terra MODIS and the Aqua MODIS dark-target *AOD* values are higher than MFRSR and Cimel *AOD* values for all wavelengths. The relative error between MFRSR at 673 nm and dark-target retrieval-algorithm measurement (Aqua MODIS) at 660 nm is 47%. However, the relative error between Deep Blue retrieval-algorithm *AOD* value at 660 nm and MFRSR *AOD* value, at 673 nm is 18% (Fig. 4.20).

These errors may be due to difficulty of distinguishing between the surface and atmospheric components of the radiance received by the satellite. The empirical relationship that is used to deduce surface reflectance of each wavelength, using the remote sensed surface reflectance values may be incorrect for bright surfaces (Kaufman et al. 1997b). The Deep Blue retrieval values are much improved over the MODIS values because Deep Blue employs two blue channels (412 and 470 nm) in MODIS, for which surface reflectances are relatively small, and are known relatively well from direct empirical measurements during clear sky conditions. (Hsu et al. 2004).

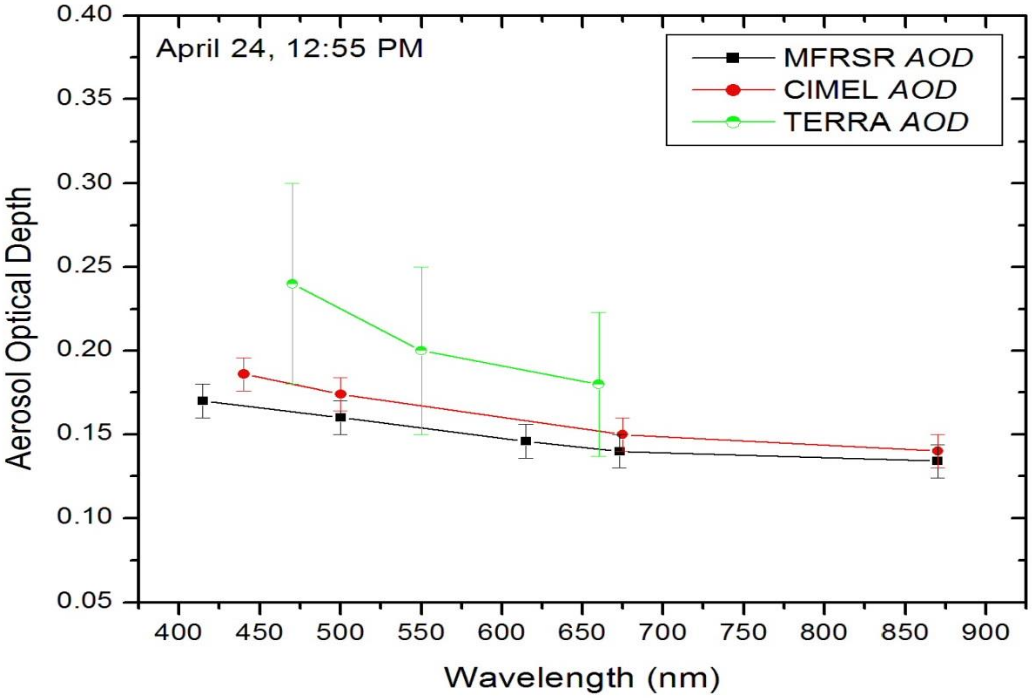

Figure 4.19 Comparison of MFRSR, Cimel and Terra MODIS dark-target *AOD*s during the dust storm for April 24, 2013 at 12:55 PM.

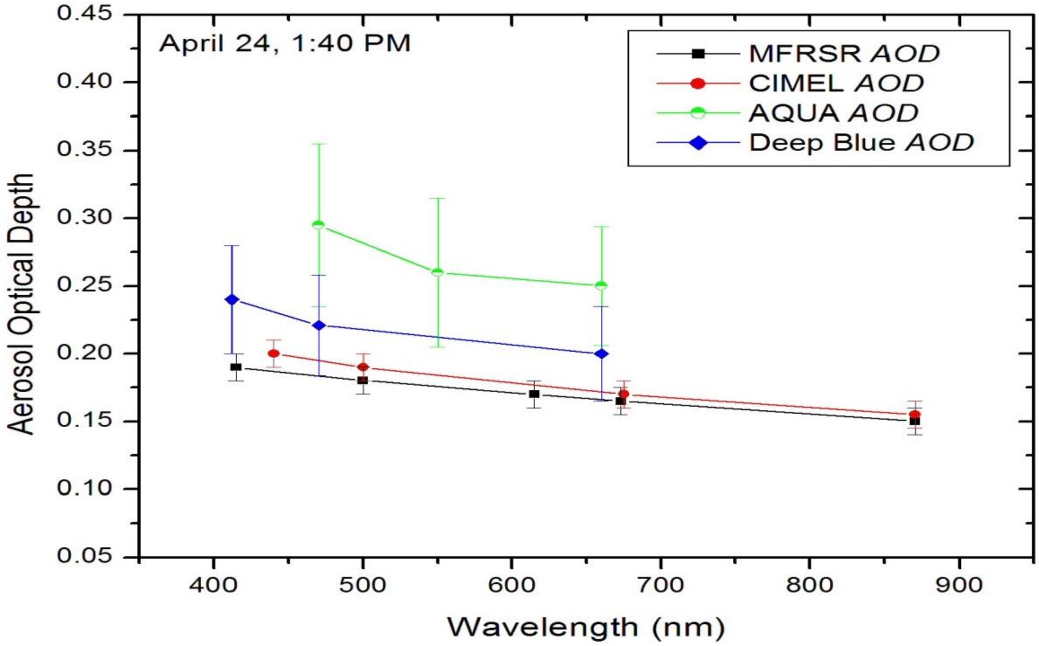

Figure 4.20 Comparison of MFRSR, Cimel, Aqua MODIS dark target and aerosol and Deep Blue retrieval *AOD*s during the dust storm for April 24, 2013 at 1:40 PM.

4.3.2 Aerosol Volume Size Distribution

The variation in aerosol volume size distribution is clearly noticeable for the dust storm in the coarse mode, while the fine mode remains relatively constant. The magnitudes of the volume size distribution of the coarse mode were high due to the dust storm during evening of April 24, 2013. The aerosol size distribution is shown in Fig. 4.21 (right). Analysis showed that the percentage of the fine mode aerosols decreased while those of coarse mode aerosols increased during the dust storm in comparison with dust free condition as shown in Fig. 4.21 (left). These results indicate that the particle sizes of the two modes are very consistent during this period and the coarse mode dominates the fine mode during the dust storm. This shows that the majority of the dust aerosol particles occurred during the evening time of April 24, 2013. The wavelength dependence of measured and retrieved (model) values of AOD shown in Fig. 4.22 indicates that they are in excellent agreement.

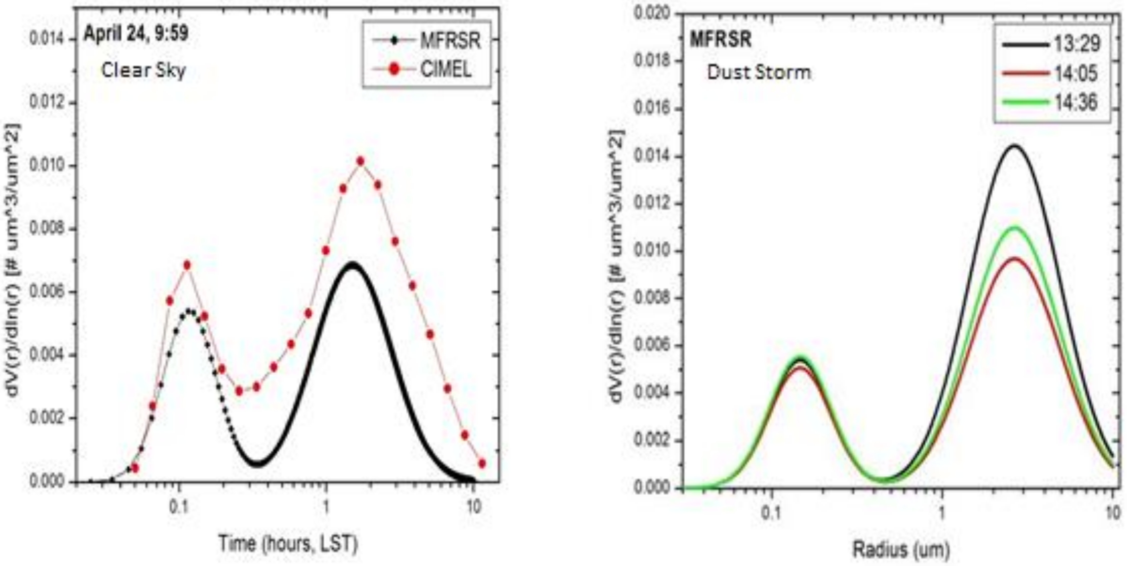

Figure 4.21 Aerosol size distributions during the dust storm using MFRSR for April 24, 2013.

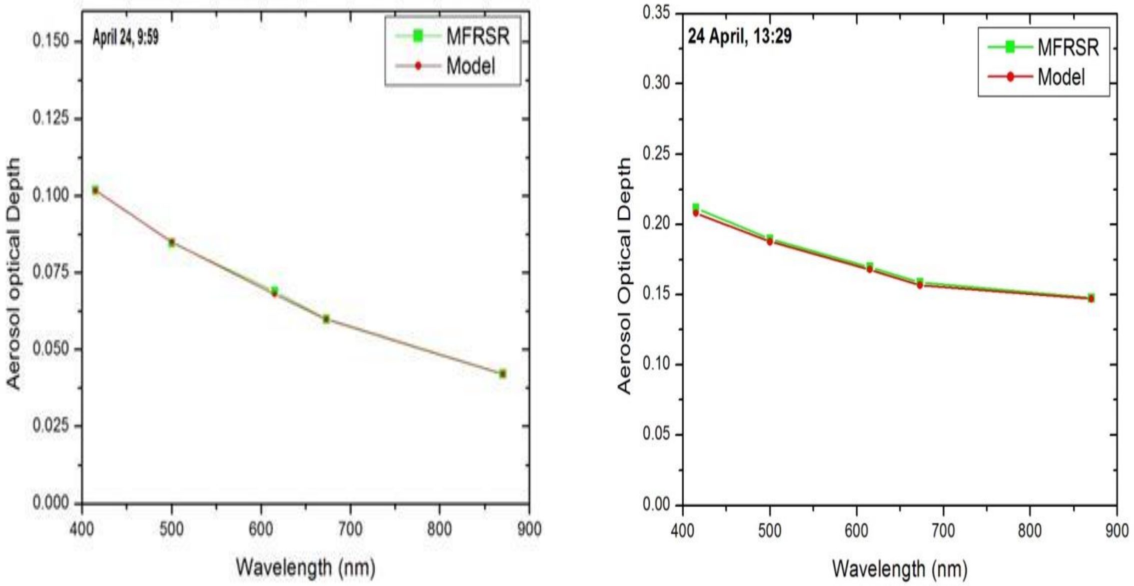

Figure 4.22 Comparison of measured and model aerosol optical depth from size distribution retrieval for April 24, 2013.

4.3.3 Back Trajectories Analysis

The HYSPLIT model was used to study the back trajectories during the dust storm on April 24, 2013. We chose three different latitudes: near-surface level (500 m from the ground), 1 km and 3 km level. Fig. 4.23 and Fig. 4.24 show the back trajectories of air masses reaching Reno on April 24 at times 1 PM and 3 PM respectively. The back trajectories demonstrate that the air masses (containing dust) reach Reno on April 24 during evening time, as expected. The bottom panels of both plots show the height of the air mass in meter above the ground level. The dust mass reaching Reno on this day strongly influences the *AOD* and *AE*.

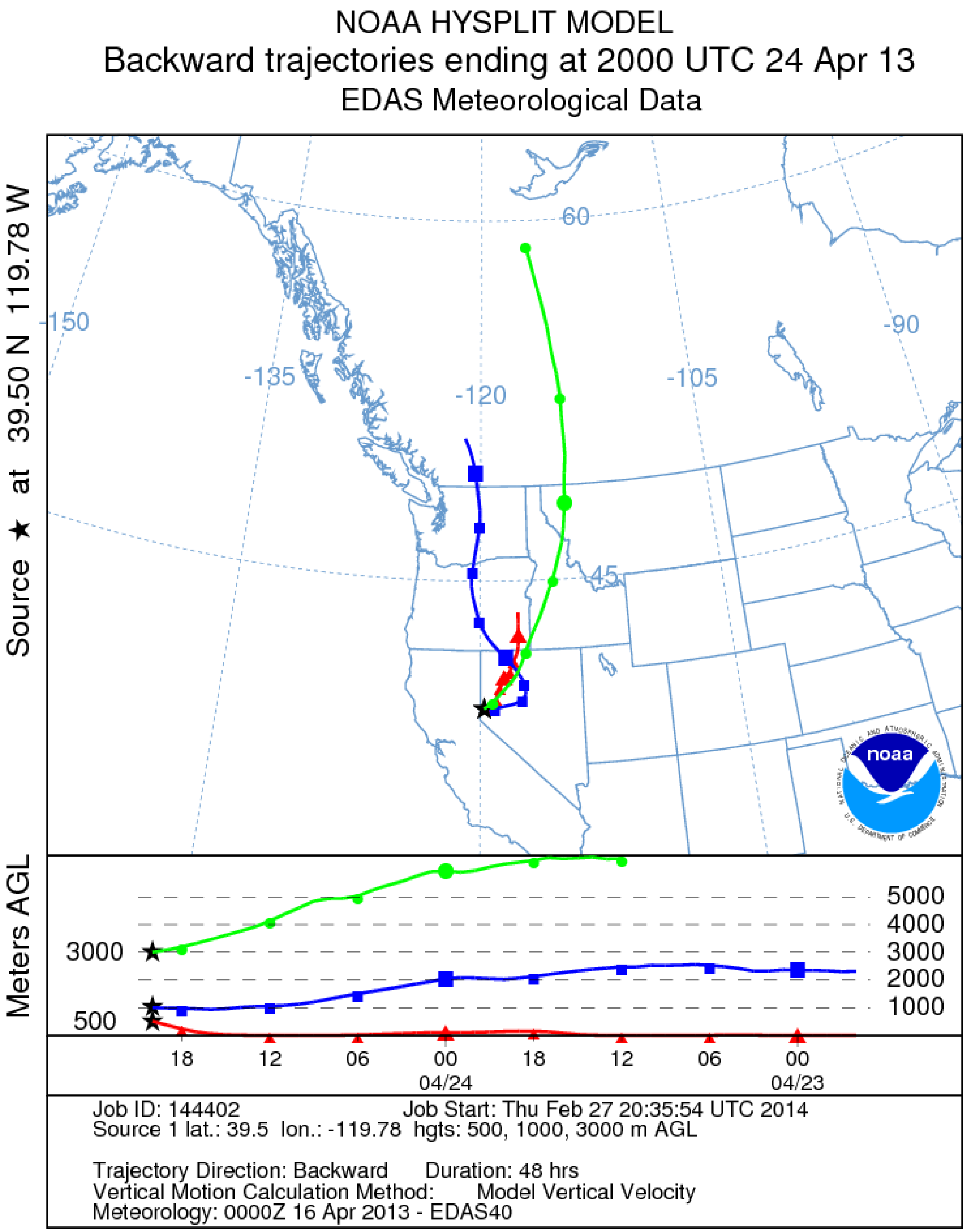

Job ID: 144402 Job Start: Thu Feb 27 20:35:54 UTC 2014
Source 1 lat.: 39.5 lon.: -119.78 hgts: 500, 1000, 3000 m AGL

Trajectory Direction: Backward Duration: 48 hrs
Vertical Motion Calculation Method: Model Vertical Velocity
Meteorology: 0000Z 16 Apr 2013 - EDAS40

Figure 4.23 48-hours back trajectory from NOAA- HYSPLIT on April 24 (20:00 UTC), 2013 to Reno during the dust storm.

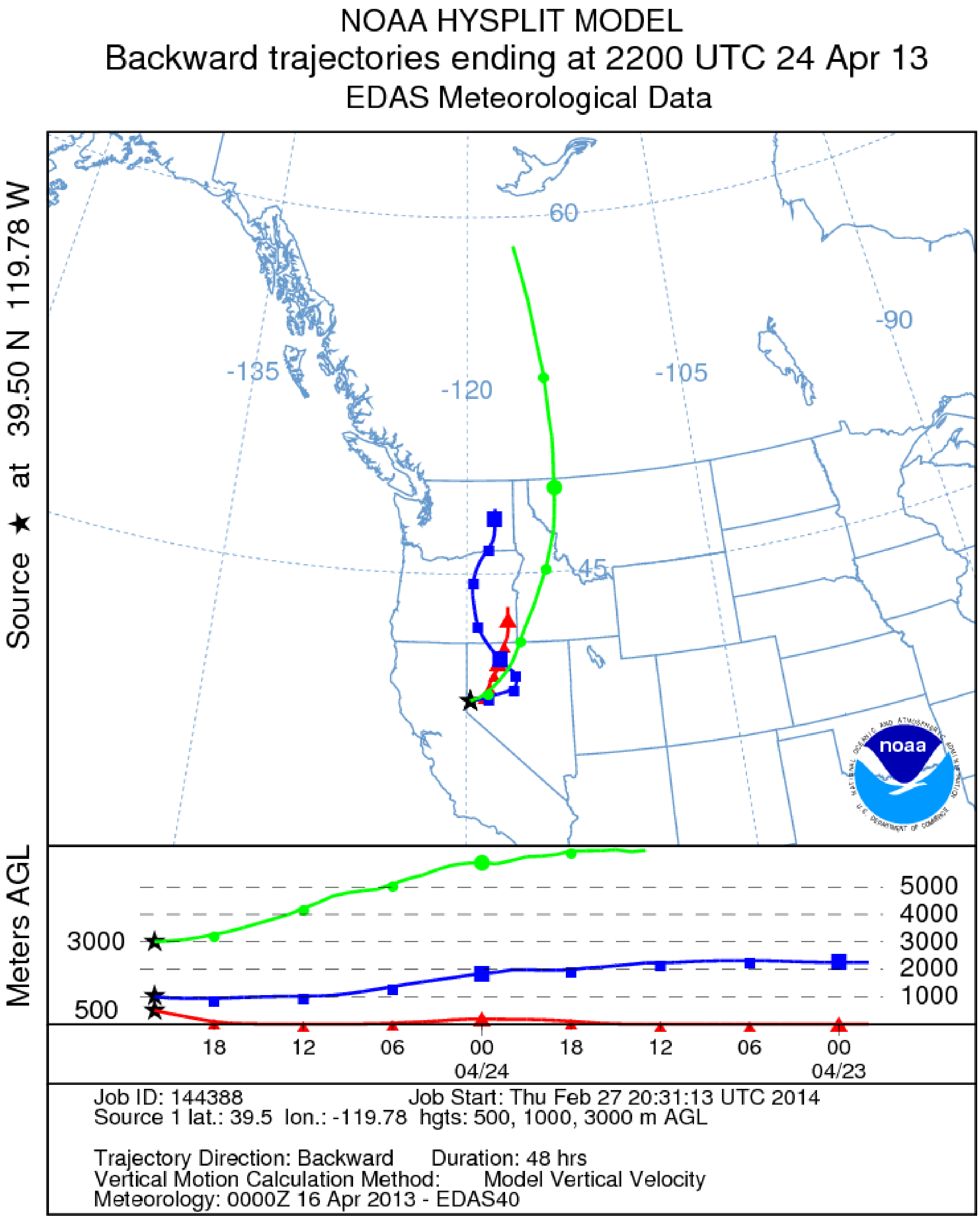

Figure 4.24 48-hours back trajectory from NOAA- HYSPLIT on April 24 (22:00 UTC), 2013 to Reno during the dust storm.

4.4 Clear Sky Days

4.4.1 Aerosol Optical Depth and Ångström Exponent

We chose 15 clear-sky days for *AOD* comparisons of ground based measurements (MFRSR and Cimel) and satellite measurements. The 500 and 870 nm channels are common to both Cimel and MFRSR instruments. For comparison with the MFRSR 673 nm channel, we interpolated between Cimel optical depths at 500 nm and 675 nm to obtain a Cimel derived estimate of optical depth at 673 nm. However, we compare the ground based *AOD* measurements at 673 nm with the satellite *AOD* measurements at 660 nm. The overall difference between the *AOD* obtained by the MFRSR and Cimel is relatively small, as shown in Table 4.3. In this work, we found that, the variation of *AOD* is between 0.018 and 0.042 at the 673 nm channel for both Cimel and MFRSR (Table 4.3).

The *AOD* variation was analyzed for early dry season months (May to August) and late dry season months (September to November). We found the aerosol concentration during the late dry season months is relatively higher compared to the other dry season months. In Fig. 4.22 and Fig. 4.23, we compare the retrieved *AOD* derived from Cimel and MFRSR. The *AOD* values during clear sky at 500 nm range from 0.017 to 0.06 for August 1, 2013 and from 0.04 to 0.06 for October 15, 2013. We compared the ground based MFRSR and Cimel *AOD* measurements with satellite *AOD* Terra MODIS dark target retrieval in Fig. 4.24 on 11:35 AM and, Aqua MODIS dark target and Deep Blue retrievals in Fig. 4.25 on 1:15 PM for the same day August 1. It was found that the Terra MODIS and Aqua MODIS dark-target *AOD* values are higher than the *AOD* values found from MFRSR and Cimel. The relative errors between MFRSR and satellite measurements (Terra MODIS, Aqua MODIS dark target and Deep Blue retrievals) are large, likely due to the misrepresentation of surface reflectance in the retrieval algorithms.

Case	**MFRSR** ***AOD***	**Cimel** ***AOD***	**Terra** ***AOD***	**Aqua** ***AOD***	**Deep Blue** ***AOD***
30 May	0.020 (0.006)	0.030 (0.006)	0.14	0.077	0.020
8 June	0.018 (0.003)	0.022 (0.002)	0.252	0.105	0.038
13 June	0.022 (0.003)	0.024 (0.003)	0.235	0.506	0.060
1 August	0.019 (0.008)	0.012 (0.005)	0.090		0.040
2 August	0.020 (0.009)	0.013 (0.003)	0.131	0.045	0.022
19 September	0.026 (0.005)	0.023 (0.005)	0.221	0.052	0.022
20 September	0.040 (0.007)	0.042 (0.005)	0.20	0.214	0.019
23 September	0.018 (0.054)	0.015 (0.002)	0.261		
4 October	0.027 (0.003)	0.026 (0.002)	0.137		
5 October	0.018 (0.008)	0.019 (0.001)	0.266		
15 October	0.026 (0.006)	0.028 (0.002)	0.157	0.154	
23 October	0.034 (0.006)	0.036 (0.004)	0.109	0.077	0.034
25 October	0.024 (0.004)	0.029 (0.008)	0.112		
26 October	0.031 (0.008)	0.037 (0.003)	0.178	0.119	0.028
27 October	0.030 (0.003)	0.040 (0.010)	0.166	0.213	

Table 4.3 MFRSR and Cimel average, (standard deviation in parentheses) of *AOD* at 673 nm wavelength and Terra MODIS dark-target, Aqua MODIS dark-target and Deep Blue retrieved *AOD* at 660 nm. The uncertainty for the MFRSR or Cimel measurements is ± 0.010 (Holben et al. 1998), Aqua MODIS dark-target is $\pm(0.05 + 0.15 * AOD)$ (R. C. Levy 2005) and Deep Blue *AOD* is $\pm(0.04 + 0.1 * AOD)$ (Shi et al. 2012).

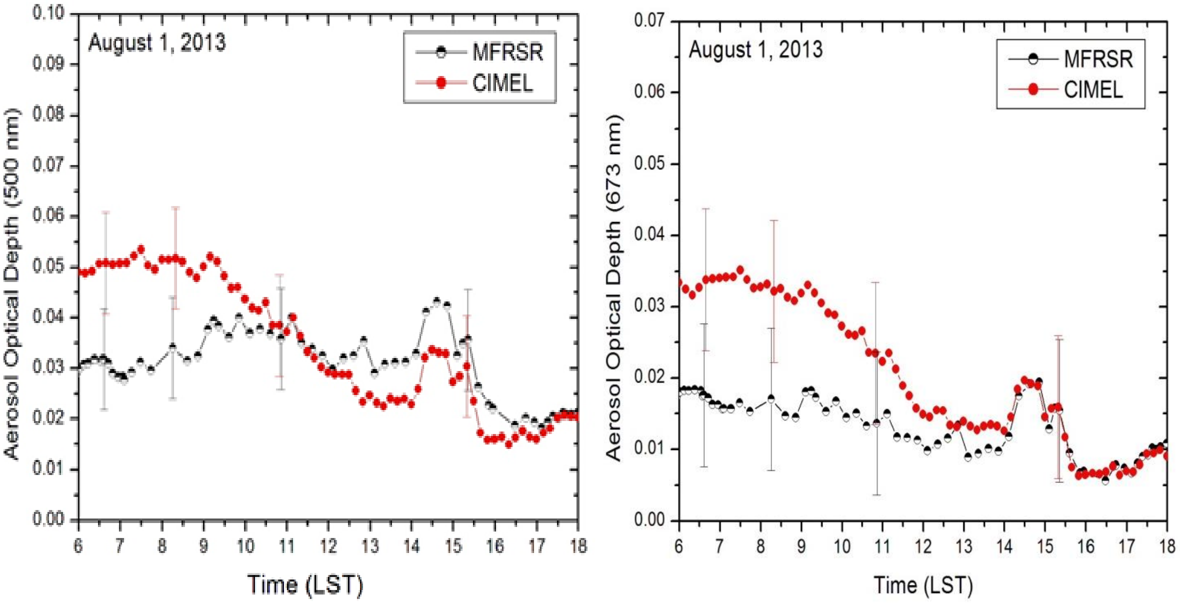

Figure 4.25 Time series comparison of MFRSR and Cimel aerosol optical depth for August 1, 2013 at UNR during the clear sky for the 500 nm and 673 nm channels.

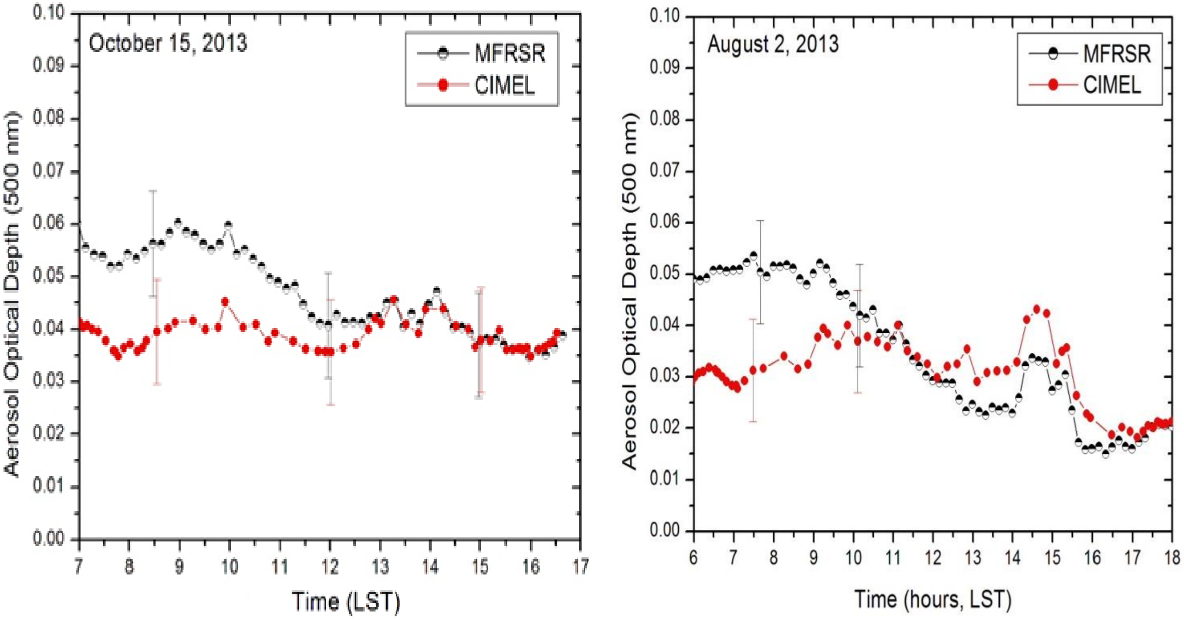

Figure 4.26 Time series comparison of MFRSR and Cimel aerosol optical depth for August 2 and October 15, 2013 at UNR during the clear sky for the 500 nm channel.

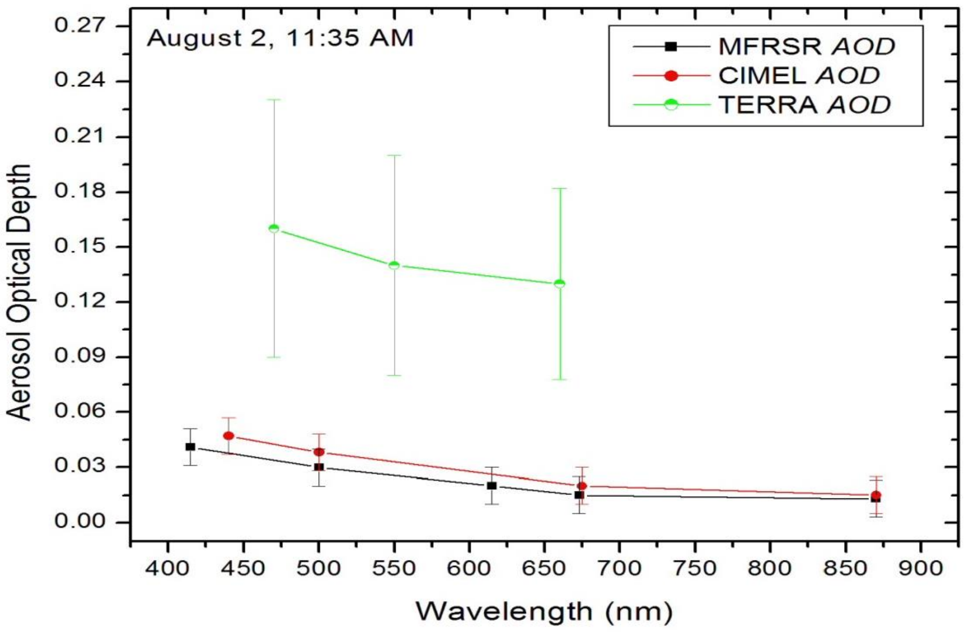

Figure 4.27 Comparison of MFRSR, Cimel and Terra MODIS dark target retrieved aerosol optical depths for August 2, 2013 at 11:35 AM.

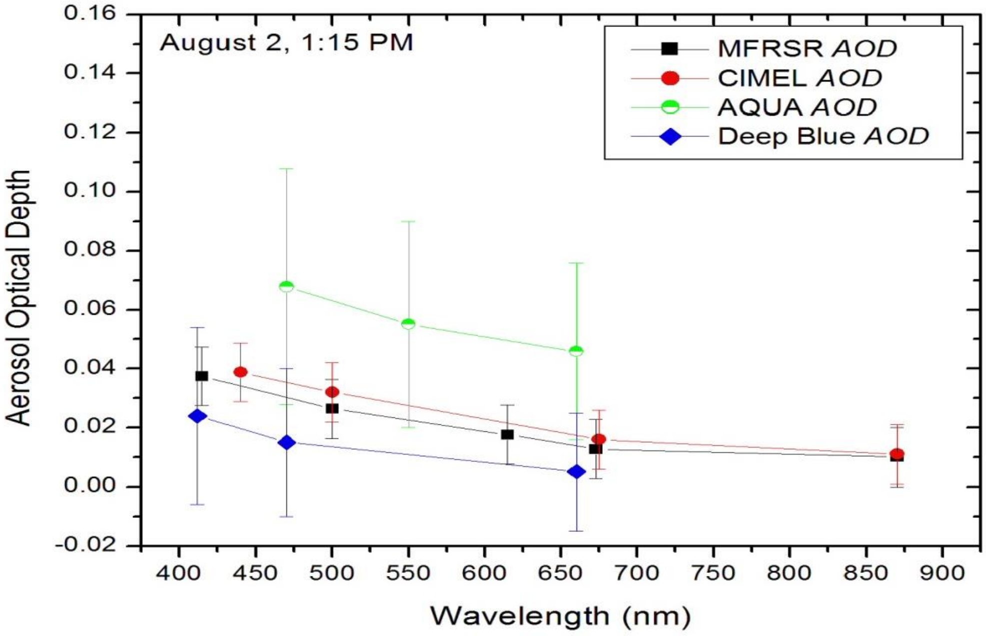

Figure 4.28 Comparison of MFRSR, Cimel, Aqua MODIS dark target and Deep Blue retrieved aerosol optical depths for August 2, 2013 at 1:15 PM.

4.4.2 Aerosol Volume Size Distribution

Fig. 4.26 shows the aerosol size distribution vs. radius obtained at ground level from MFRSR and Cimel measurements for August 2, 2013 during the clear sky cloud free day. The observed volume size distribution is bimodal with fine modal radius between 0.02 to 0.4 µm, and the coarse mode between 0.5 to 10 µm. It was found that fine and coarse mode volume concentrations were similar. It is also found that, during the clear sky, both fine and coarse modes distributions are very small as expected due to the lower aerosol loading. Fig. 4.27 indicates that the wavelength dependence of measured and retrieved (model) values of *AOD* are in excellent agreement.

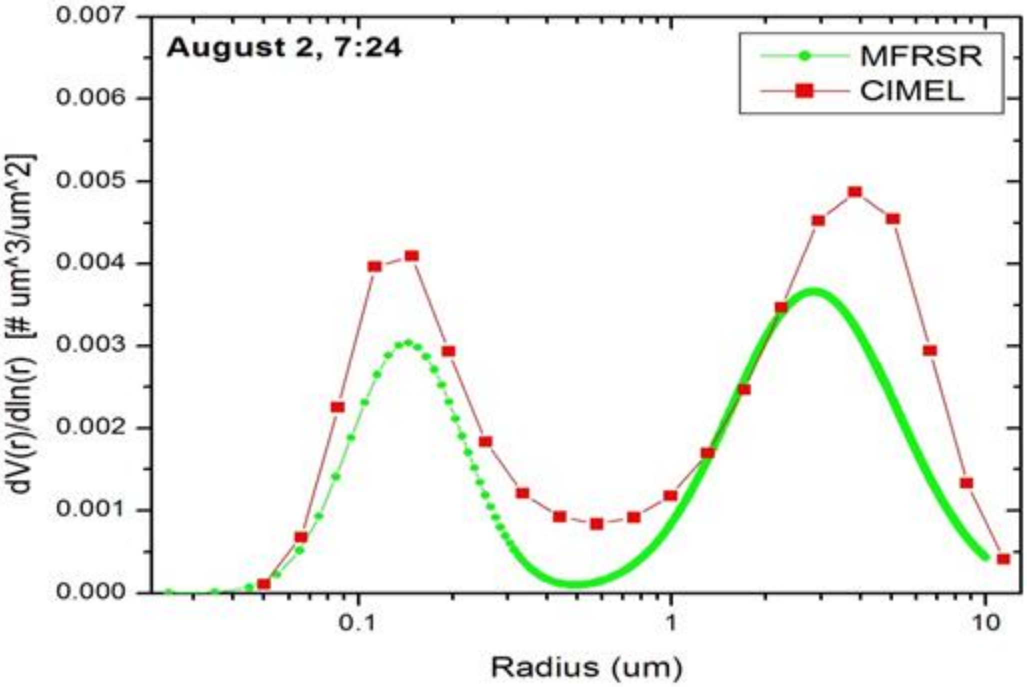

Figure 4.29 Aerosol size distribution comparison derived from MFRSR and Cimel for August 2, 2013 during the clear sky cloud free day.

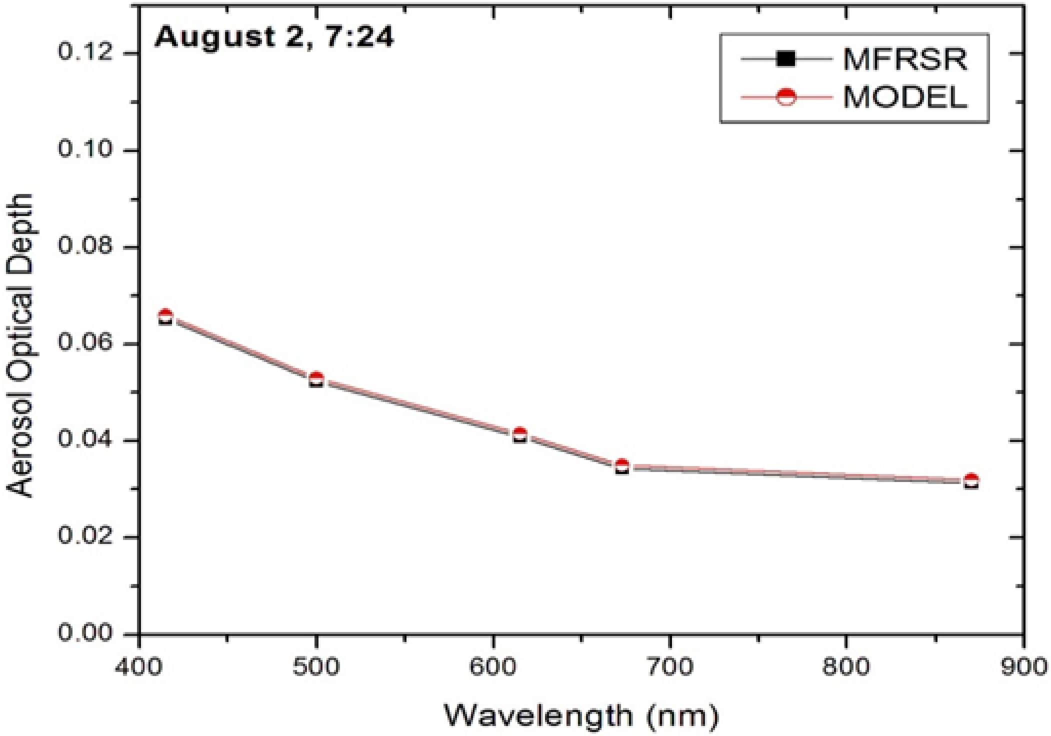

Figure 4.30 The spectrally dependent *AOD* derived from the MFRSR data and Mie calculation by using the retrieved aerosol size distribution and refractive index for clear sky on August 2, 2013.

4.5 References for Chapter 4

Alexandrov, Mikhail D., Andrew A. Lacis, Barbara E. Carlson, and Brian Cairns. 2008. "Characterization of Atmospheric Aerosols Using MFRSR Measurements." *Journal of Geophysical Research* 113 (D8). doi:10.1029/2007JD009388. http://pubs.giss.nasa.gov/abs/al07300k.html.

Ångström, Anders. 1929. "On the Atmospheric Transmission of Sun Radiation and on Dust in the Air." *Geografiska Annaler* 11 (January): 156–66. doi:10.2307/519399.

Ge, J. M., J. Su, T. P. Ackerman, Q. Fu, J. P. Huang, and J. S. Shi. 2010. "Dust Aerosol Optical Properties Retrieval and Radiative Forcing over Northwestern China during the 2008 China-U.S. Joint Field Experiment." *Journal of Geophysical Research: Atmospheres* 115 (D7): n/a–n/a. doi:10.1029/2009JD013263.

Holben, B. N., T. F. Eck, I. Slutsker, D. Tanré, J. P. Buis, A. Setzer, E. Vermote, et al. 1998a. "AERONET—A Federated Instrument Network and Data Archive for Aerosol Characterization." *Remote Sensing of Environment* 66 (1): 1–16. doi:10.1016/S0034-4257(98)00031-5.

Holben, B.N., T.F. Eck, I. Slutsker, D. Tanré, J.P. Buis, A. Setzer, E. Vermote, et al. 1998b. "AERONET—A Federated Instrument Network and Data Archive for Aerosol Characterization." *Remote Sensing of Environment* 66 (1): 1–16. doi:10.1016/S0034-4257(98)00031-5.

Hsu, N.C., Si-Chee Tsay, M.D. King, and J.R. Herman. 2004. "Aerosol Properties over Bright-Reflecting Source Regions." *IEEE Transactions on Geoscience and Remote Sensing* 42 (3): 557–69. doi:10.1109/TGRS.2004.824067.

Kaufman, Y. J., D. Tanré, L. A. Remer, E. F. Vermote, A. Chu, and B. N. Holben. 1997. "Operational Remote Sensing of Tropospheric Aerosol over Land from EOS Moderate Resolution Imaging Spectroradiometer." *Journal of Geophysical Research: Atmospheres* 102 (D14): 17051–67. doi:10.1029/96JD03988.

Li, Fuyu, Paul Ginoux, and V. Ramaswamy. 2008. "Distribution, Transport, and Deposition of Mineral Dust in the Southern Ocean and Antarctica: Contribution of Major Sources." *Journal of Geophysical Research: Atmospheres* 113 (D10): n/a–n/a. doi:10.1029/2007JD009190.

McNeal, Fred. 2008. "Back Trajectory Analysis: Air Parcel Histories and Forest Pollutant Exposure". Working Paper. http://deepblue.lib.umich.edu/handle/2027.42/62027.

Queface, Antonio J., Stuart J. Piketh, Harold J. Annegarn, Brent N. Holben, and Rogerio J. Uthui. 2003. "Retrieval of Aerosol Optical Thickness and Size Distribution from the Cimel Sun Photometer over Inhaca Island, Mozambique." *Journal of Geophysical Research: Atmospheres* 108 (D13): n/a–n/a. doi:10.1029/2002JD002374.

R. C. Levy, L. A. Remer. 2005. "Evaluation of the MODIS Aerosol Retrievals over Ocean and Land during CLAMS." *Journal of The Atmospheric Sciences - J ATMOS SCI* 62 (4): 974–92. doi:10.1175/JAS3391.1.

Seinfeld, John H., and Spyros N. Pandis. 1998. *Atmospheric Chemistry and Physics: From Air Pollution to Climate Change*. Wiley.

Shi, Y., J. Zhang, J. S. Reid, E. J. Hyer, and N. C. Hsu. 2012. "Critical Evaluation of the MODIS Deep Blue Aerosol Optical Depth Product for Data Assimilation over North Africa." *Atmos. Meas. Tech. Discuss.* 5 (5): 7815–65. doi:10.5194/amtd-5-7815-2012.

Smithson, Peter A. 2002. “IPCC, 2001: Climate Change 2001: The Scientific Basis. Contribution of Working Group 1 to the Third Assessment Report of the Intergovernmental Panel on Climate Change, Edited by J. T. Houghton, Y. Ding, D. J. Griggs, M. Noguer, P. J. van Der Linden, X. Dai, K. Maskell and C. A. Johnson (eds). Cambridge University Press, Cambridge, UK, and New York, USA, 2001. No. of Pages: 881. Price £34.95, US$ 49.95, ISBN 0-521-01495-6 (paperback). £90.00, US$ 130.00, ISBN 0-521-80767-0 (hardback).” *International Journal of Climatology* 22 (9): 1144–1144. doi:10.1002/joc.763.

Chapter 5 Single Scattering Albedo, Asymmetry Parameter and Radiative Forcing Case Studies

5.1 Introduction

The single scattering albedo (*SSA*) and asymmetry parameter (*ASY*) are key parameters for the assessment of aerosol radiative forcing contributions of absorption to the extinction (Alam et al. 2012). The *SSA* is the fraction of the energy removed from the incident wave that reappears as scattered radiation. The wavelength dependent *SSA* is important in understanding the climatic effects of the aerosols. The value of the *SSA* strongly depends on the aerosol composition and size distribution (Dubovik et al. 2002, More et al; 2013). Lower values of the *SSA* indicate the presence of absorbing aerosols such as certain types of biomass burning, vehicular emission and industrial pollutants, whereas higher values of *SSA* indicates the dominance of scattering aerosols such as sulfate, nitrate and some organic aerosols and certain types of the dust in the atmosphere (Dickerson et al. 1997).

The *ASY* is the average value of the cosine of the scattering angle for the scattered radiation. The values of the *ASY* can range from -1 for backwards scattering to +1 for forward scattering, with a value of 0.7 commonly used in radiative transfer models for aerosols. For Rayleigh scattering, i.e. equal forward and backward scattering, the asymmetry parameter is zero. As the forward scattering dominates over the backward scattering the asymmetry parameter increases. The *SSA* and *ASY* both are important for radiative forcing calculations.

5.2 California Rim Fire, August-September 2013

5.2.1 Solar Irradiance Measurements

The solar irradiance and energy fluxes play an important role of the atmospheric circulation. The determination of the solar irradiation and its interaction with the atmosphere and the Earth's surface is important since solar irradiation accounts for almost all the energy available to the Earth (Queface, 2013). The solar irradiance can reach the Earth’s surface by two ways. The first is direct solar irradiation, where solar irradiation is directly transmitted through the atmosphere and second is via diffuse solar irradiation due to gases, aerosols, and clouds where the incoming solar irradiation is scattered or reflected (Queface, 2013).

We measured three parameters of radiation fluxes at UNR: global, diffuse and direct. The global, diffuse and direct normal irradiances were measured by using MFRSR and also retrieved by using the 2-stream model. These measurements were obtained during the Rim fire for the period of mid-August to mid-September, 2013. Fig. 5.1 and Fig. 5.2 are the time series of diffuse, normal direct and global solar irradiance measurements at wavelengths 500 nm and 870 nm (10 nm bandwidths) taken at UNR during the Rim fire on August 23, 2013. From MFRSR observed data for August 23, 2013, the maximum values of the diffuse, normal direct and global irradiances for the 500 nm channel were found to be 0.85, 0.29 and 1.05 $\mathrm{Wm^{-2}nm^{-1}}$, respectively.

A 2-stream model was used to compare with the observed irradiances for all wavelengths. The *ASY* and *SSA* values used were from the retrievals as discussed in Chapter 3. The model calculations give the diffuse, normal direct and global irradiances as 0.83, 0.28 and 1.02 $\mathrm{Wm^{-2}nm^{-1}}$, respectively at 500 nm. For 870 nm, the values of the diffuse, normal direct and global irradiances were found to be 0.28, 0.54 and 0.69 $\mathrm{Wm^{-2}nm^{-1}}$, respectively using MFRSR, and 0.29, 0.53 and 0.68 $\mathrm{Wm^{-2}nm^{-1}}$, respectively using the 2-stream model for August 23. It is found that the percent difference between the MFRSR observed and 2-stream model (diffuse, normal direct and global irradiance) values are less than 5% for both wavelengths.

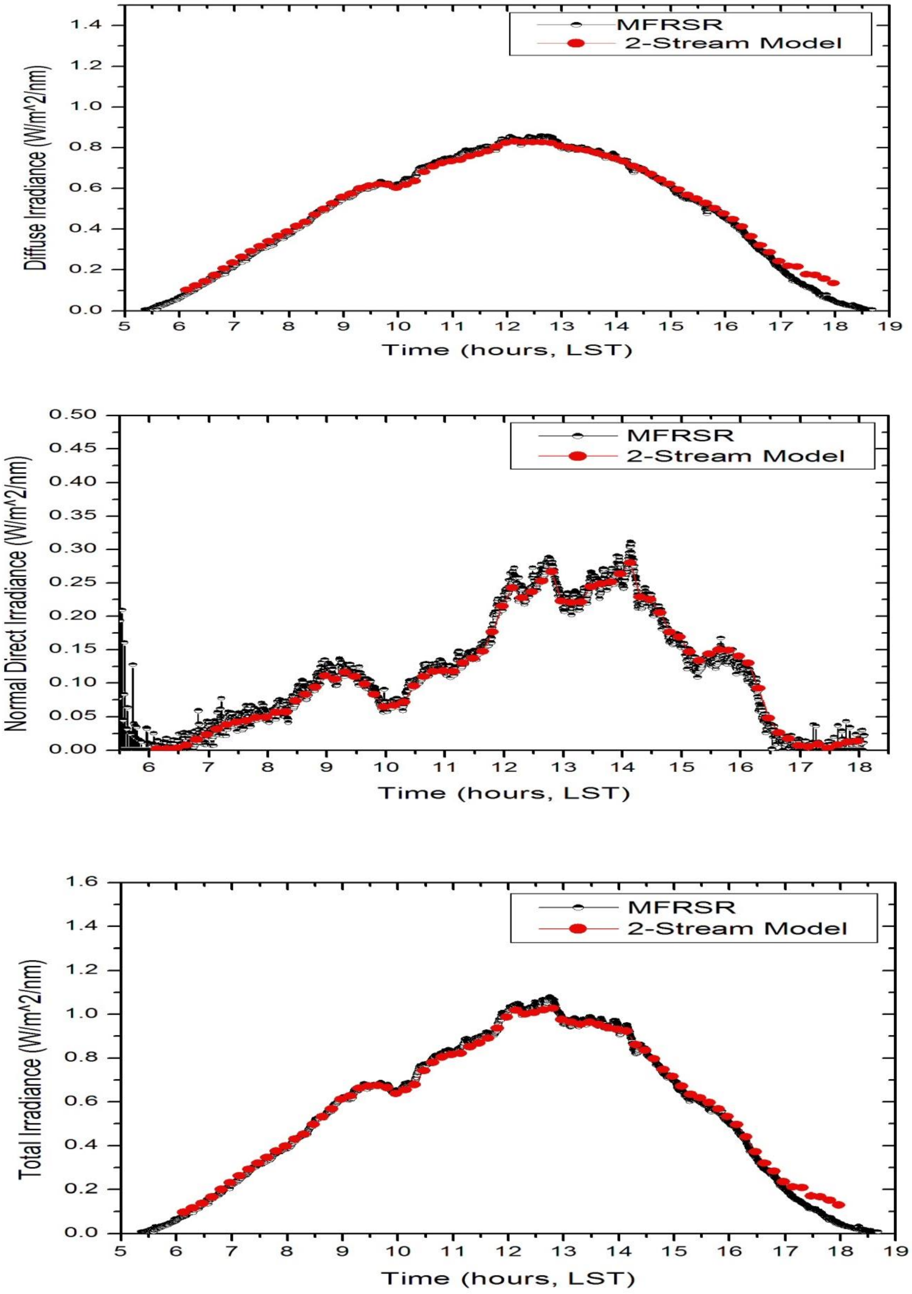

Figure 5.1 Diffuse irradiance (top), normal direct irradiance (middle) and total irradiance (bottom) for 500 nm during the Rim fire on August 23, 2013 using MFRSR observed values and 2-stream model.

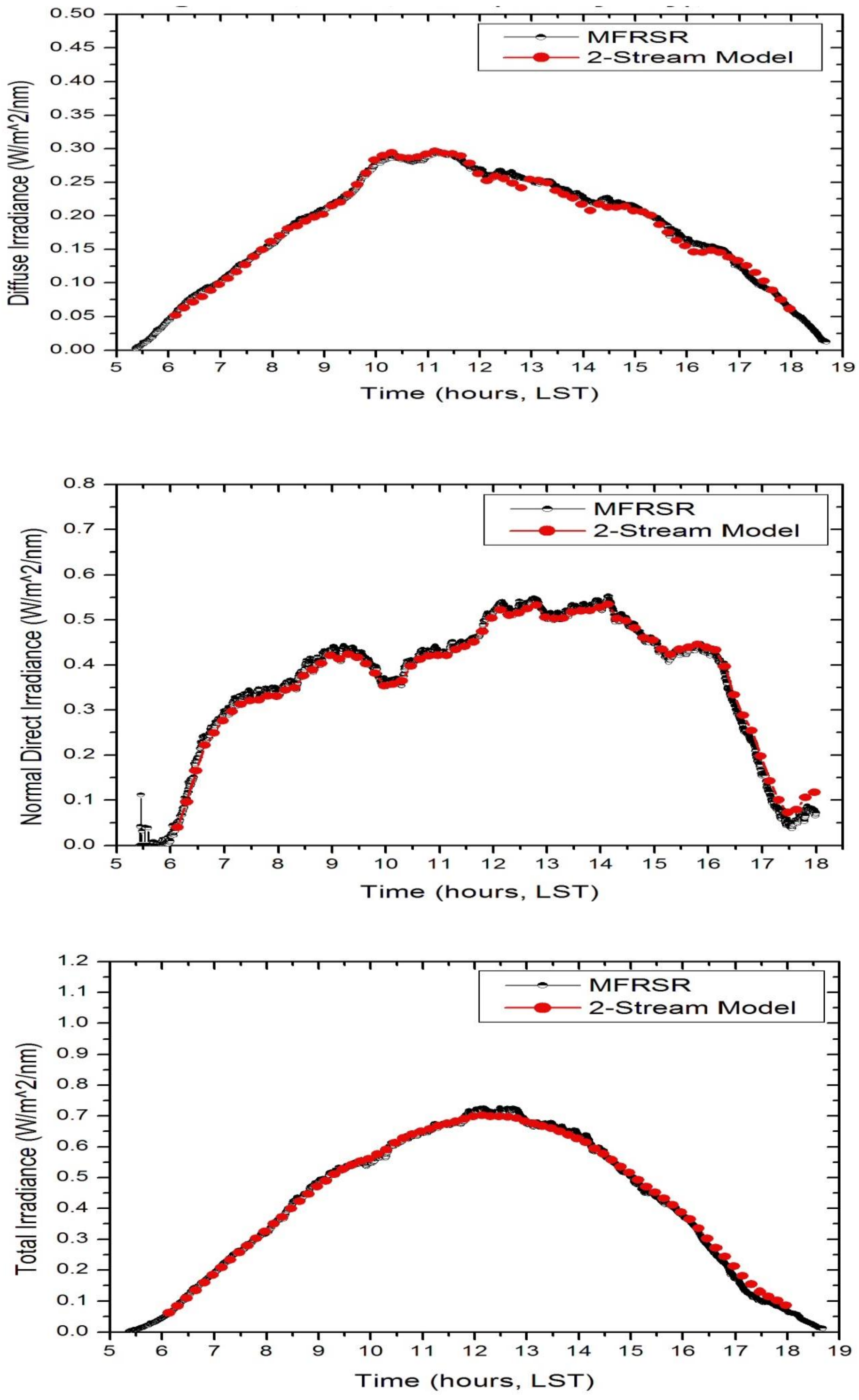

Figure 5.2 Diffuse irradiance (top), normal direct irradiance (middle) and total irradiance (bottom) for 870 nm during the Rim fire on August 23, 2013 using MFRSR observed values and 2-stream model.

The MFRSR measured global, diffuse and direct normal radiative fluxes with respect to low polluted, medium polluted and highly polluted atmospheric conditions during the Rim fire, 2013 are shown in Table 5.1. The reduction in the global irradiance and direct normal irradiance during the highly polluted days is due to high aerosol (smoke) loading. The increase in the diffuse irradiance during highly polluted atmospheric conditions is due to scattering of solar radiation by high aerosol loading.

Date	**Aerosol loading classes**	**Maximum Diffuse Irradiance $\mathbf{Wm^{-2}nm^{-1}}$**	**Maximum Normal Direct Irradiance $\mathbf{Wm^{-2}nm^{-1}}$**	**Maximum Global Irradiance $\mathbf{Wm^{-2}nm^{-1}}$**
August 23	High aerosol (smoke)	0.85	0.29	1.05
August 24	Medium aerosol (smoke)	0.76	0.75	1.31
August 26	Medium aerosol (smoke)	0.56	0.88	1.35
August 27	High aerosol (smoke)	0.80	0.19	0.96
August 28	High aerosol (smoke)	0.81	0.47	1.23
August 29	Low aerosol (smoke)	0.41	1.39	1.47
August 30	Medium aerosol (smoke)	0.58	0.99	1.34
August 31	Low aerosol (smoke)	0.36	1.43	1.51
September 1	High aerosol (smoke)	0.75	0.22	0.91
September 3	Medium aerosol (smoke)	0.48	1.21	1.47
September 5	Low aerosol (smoke)	0.37	1.41	1.55
September 7	Medium aerosol (smoke)	0.51	0.96	1.26

Table 5.1: Maximum diffuse, normal direct and total irradiances at 500 nm using MFRSR observed values during 12 selected days of Rim fire 2013.

5.2.2 Single Scattering albedo (*SSA*)

The *SSA* is an important parameter specifying the impact of aerosols on radiative forcing, particularly for absorbing aerosols such as those generated from biomass burning (Kaufman et al. 1997). Fig. 5.3 shows the spectral dependence of *SSA* between 440 and 1020 nm wavelengths using Cimel, and between 415 and 870 nm using MFRSR. The decreased *SSA* with wavelength is due to the absorption of radiation by small black carbon (*BC*) particles in a mixture of non-absorbing particles (Eck et al. 2001, Dubovik et al. 2002). In general, biomass burning aerosols are known to be an absorbing aerosol, due to black carbon produced by combustion during flaming combustion. Low *SSA* values may induce warming because of absorption of the solar radiation by absorbing aerosols (Queface, 2013).

The value of *SSA* varies significantly for smoke due to the presence of black carbon in the combustion products. The highest absorption of the solar radiation with the strong spectral dependence was observed for the African savanna regions and the lowest absorption was observed for North America boreal forest (Dubovik et al. 2002). However, the different in absorption may also be due to the different factors such as impact of the moisture content of the fuel, the degree of the aging of the particles, relative humidity, ambient temperature and fire intensity (Jacobson 2001). In this study, we compare values of the *SSA* from MFRSR and Cimel retrievals. The MFRSR retrieved *SSA* values decreased from 0.91 to 0.86 for the wavelength range 415 to 870 nm, at 9:01 AM local time for August 23, 2013 during the highest smoke concentration in Reno of the Rim fire. Similarly, by using Cimel, the *SSA* values decreased from 0.92 to 0.88 for wavelength 440 to 869 nm (Fig. 5.3 (top)). However, at 4:36 PM, the *SSA* values decreased from 0.93 to 0.90 using MFRSR and 0.94 to 0.92 using Cimel for the same wavelength range (Fig. 5.3 (bottom)). The uncertainty in the MFRSR or Cimel derived *SSA* is about ± 0.03 (Kassianov et al. 2007).

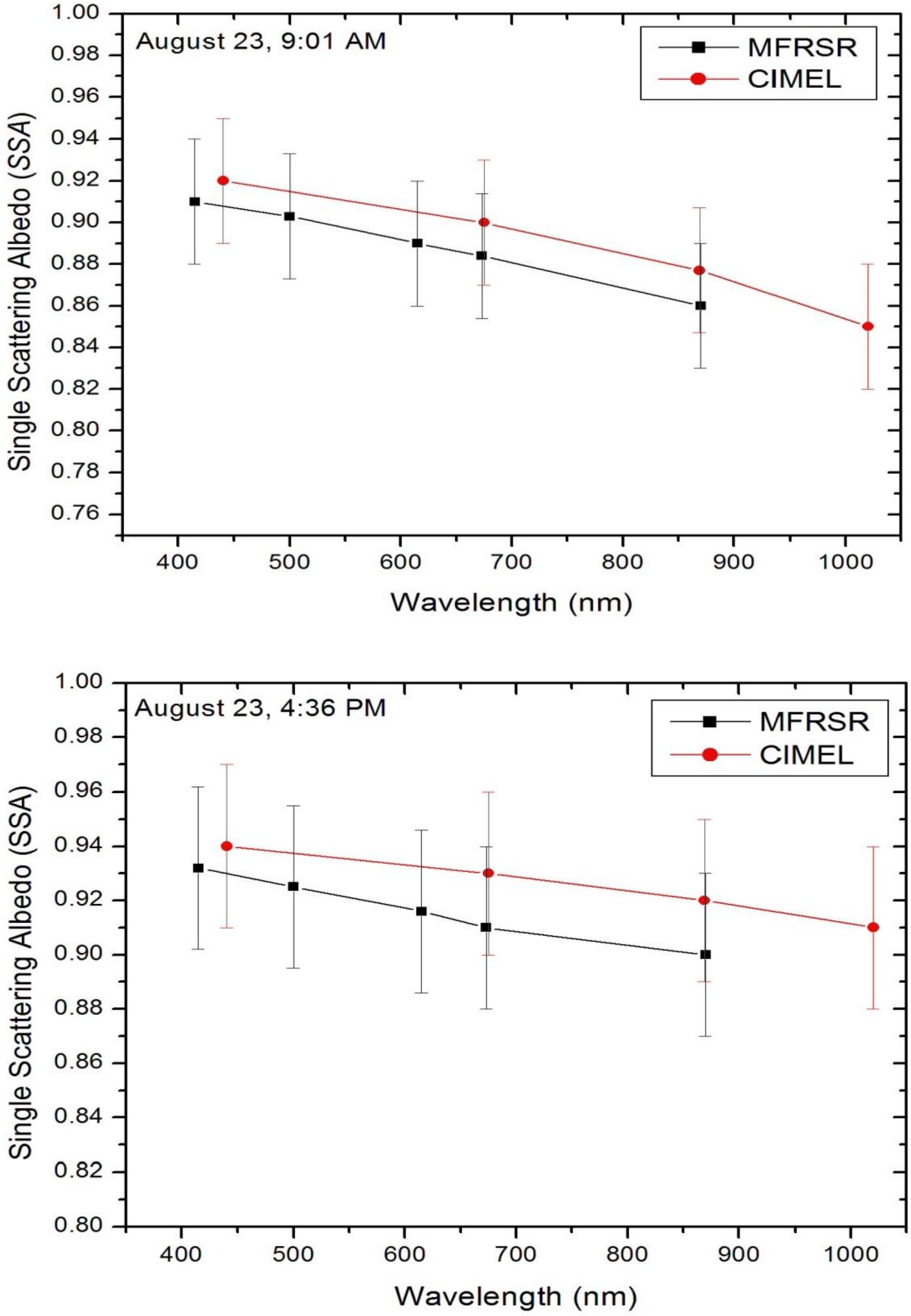

Figure 5.3 Variation of the *SSA* with wavelength using MFRSR and Cimel during the Rim fire on August 23, 2013.

5.2.3 *SSA* Comparison between Photoacoustic (PA) and MFRSR measurements

Fig. 5.4 and Fig. 5.5 compare the *SSA* calculations from PA and MFRSR retrievals for two different days. Fig. 5.4 is for a smoky day, August 23, 2013 and Fig 5.5 is for a clear day, October 24, 2013.

It is interesting to note from Fig. 5.4 that, for the smoky day, the *SSA* values from PA measurements and from the MFRSR retrievals are comparable. For PA measurements the air is sampled relatively close to the ground while the MFRSR measures a columnar value of the *SSA*. It is noteworthy that the PA and MFRSR measurements give similar values of the *SSA* for the smoky day, suggesting well-mixed smoke in the atmosphere near ground level. For both instruments, *SSA* decreases slightly from 0.88 (at 6 AM) to 0.87 (at 8 AM) due to the emissions of BC from the vehicles during the morning rush hour. As the day progresses, the *SSA* for both instruments increases continuously and reaches a maximum value of 0.89 at 6 PM local time. For comparison, Gyawali et al., 2009 reported a *SSA* value of around 0.91 (at 6 PM) during California wildfires of summer 2008 at 405 nm. Also apparent from the Fig. 5.4 is the absence of a strong diurnal cycle on the *SSA*. The nearly constant values of *SSA* (around 0.88) from 6 AM to 6 PM suggest the consistent dominance of the smoke throughout the day.

In contrast to Fig. 5.4, Fig. 5.5 depicts the considerable variations of *SSA* calculations from PA and MFRSR for a clean day, October 24, 2013. This perhaps is as expected, for a not well mixed day, like this, the *SSA* obtained from the PA is more representative of the ground level air sample while those obtained from MSRSR are representative of the entire column above the instrument. It is noteworthy that, unlike Fig. 5.4, Fig. 5.5 shows the strong diurnal cycle on *SSA* for both PA and MFRSR, with minima on the morning rush hour and maxima on either side. The *SSA* obtained from the MFRSR is considerably higher than that of the PA implying the very different optical nature of the air close to the ground and the air above the surface. It can be seen from the plot that in comparison to the PA measurements, the rush hour emissions have little but slightly noticeable effect on the MFRSR retrievals.

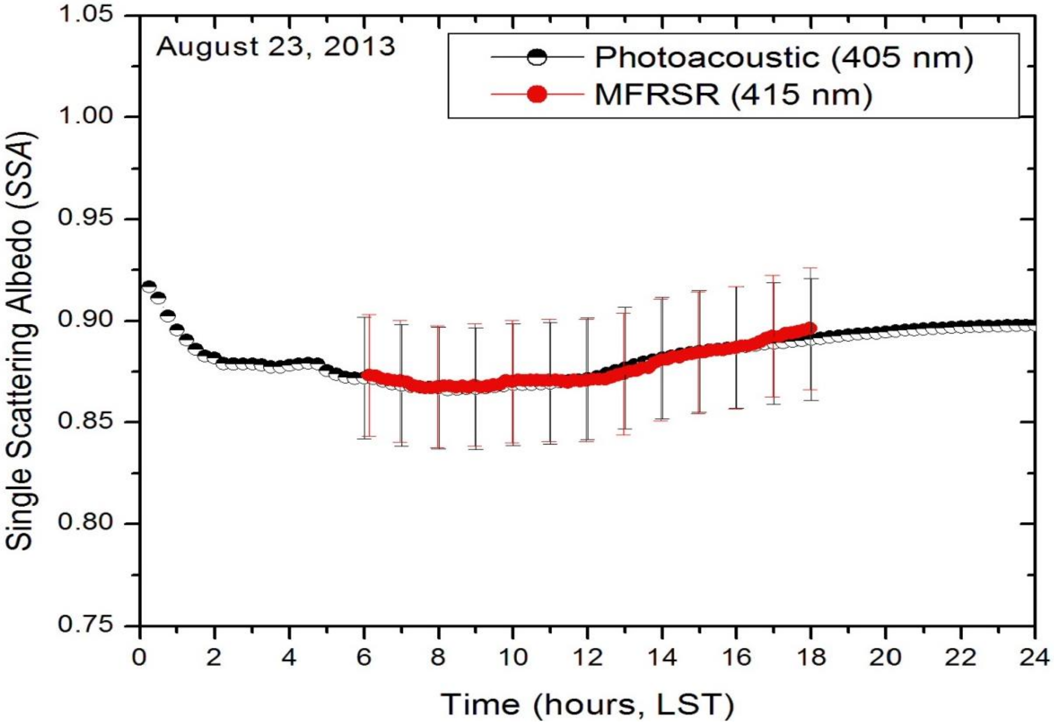

Figure 5.4 Comparison of the SSA using MFRSR at 415 nm and Photoacoustic (PA) measurements at 405 nm during the Rim fire on August 23, 2013

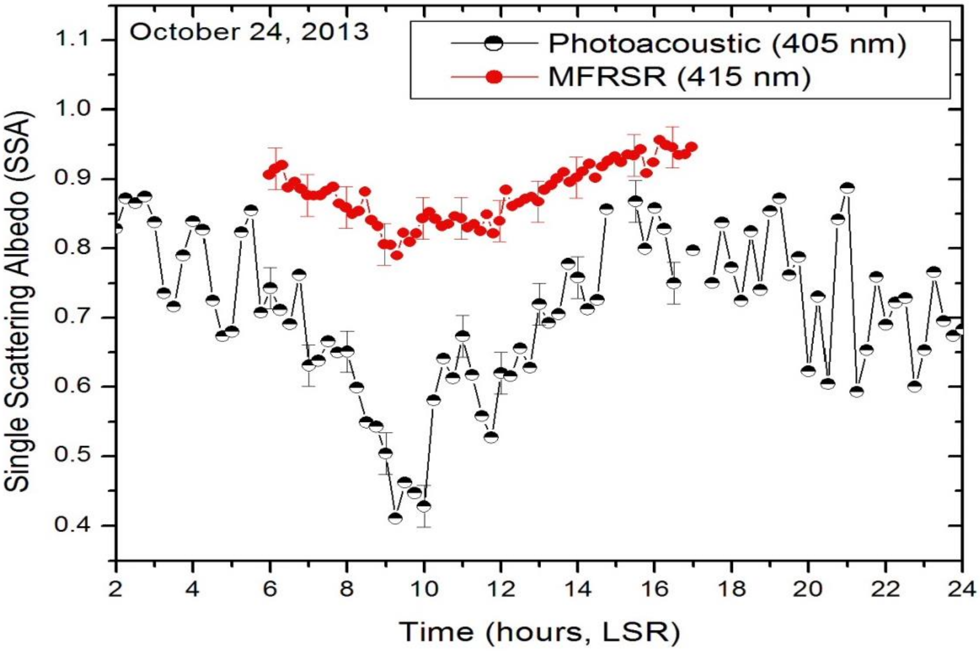

Figure 5.5 Comparison of the SSA using MFRSR at 415 nm and Photoacoustic at 405 nm during the clear sky day on October 24, 2013.

5.2.4 Asymmetry parameter and imaginary part of refractive index

The *ASY* ranges from a maximum 0.68 at 415 nm to a minimum of 0.52 at 870 nm during high aerosol (smoke) loading by using MFRSR on August 23, 2013. Also by using Cimel, the asymmetry parameter varies from a maximum 0.67 at 440 nm to a minimum 0.43 at 1020 nm on the same day (Fig. 5.6). The uncertainty in MFRSR or Cimel derived *ASY* is about ± 0.03 (Kassianov et al. 2007). Similarly, Fig. 5.7 shows that daily variation of the wavelength dependence of the *ASY*. It can be seen from the plot that the value of asymmetry parameter decreases with an increase in wavelength and varies from 0.50 to 0.72. The *ASY* for all wavelengths decreases slightly as the day progresses and remains constant thorough the day. The higher values of the *ASY* at the shorter wavelengths (415 and 500 nm) suggest more forward scattering by the smoke aerosols at these wavelengths compared to at the 870 nm. The mean daily values (± standard deviations) of the *ASY* for wavelengths 415, 500 and

870 nm are 0.69±0.01, 0.65±0.01 and 0.52±0.02, respectively. The values of the *ASY* reported in Fig. 5.7 are comparable with the *ASY* values reported for a strong wildfire event over Valencia (Spain) during the summer 2012 (Gómez-Amo et al. 2013).

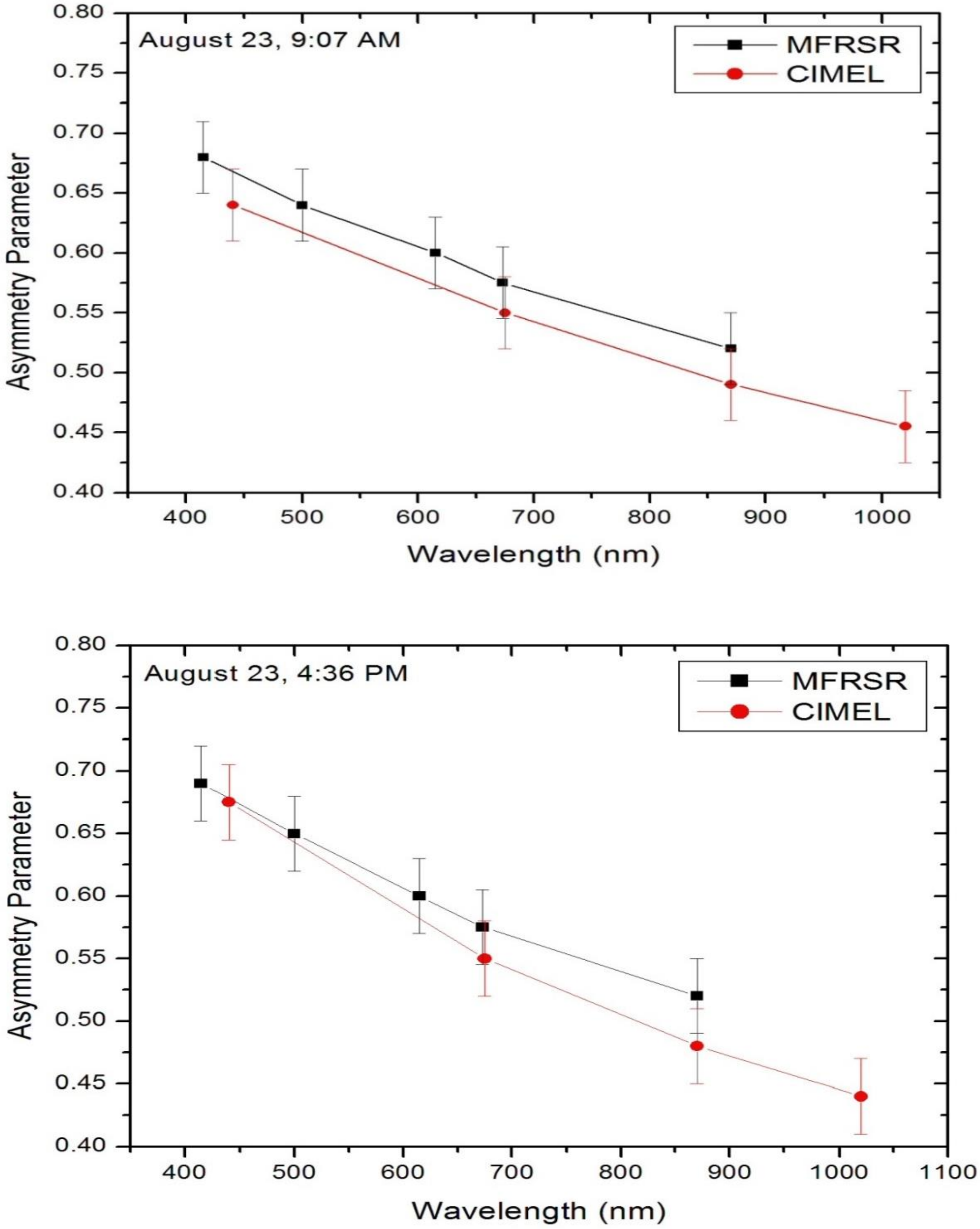

Figure 5.6 Variation of the asymmetry parameter with wavelength using MFRSR and Cimel during the Rim fire on August 23, 2013.

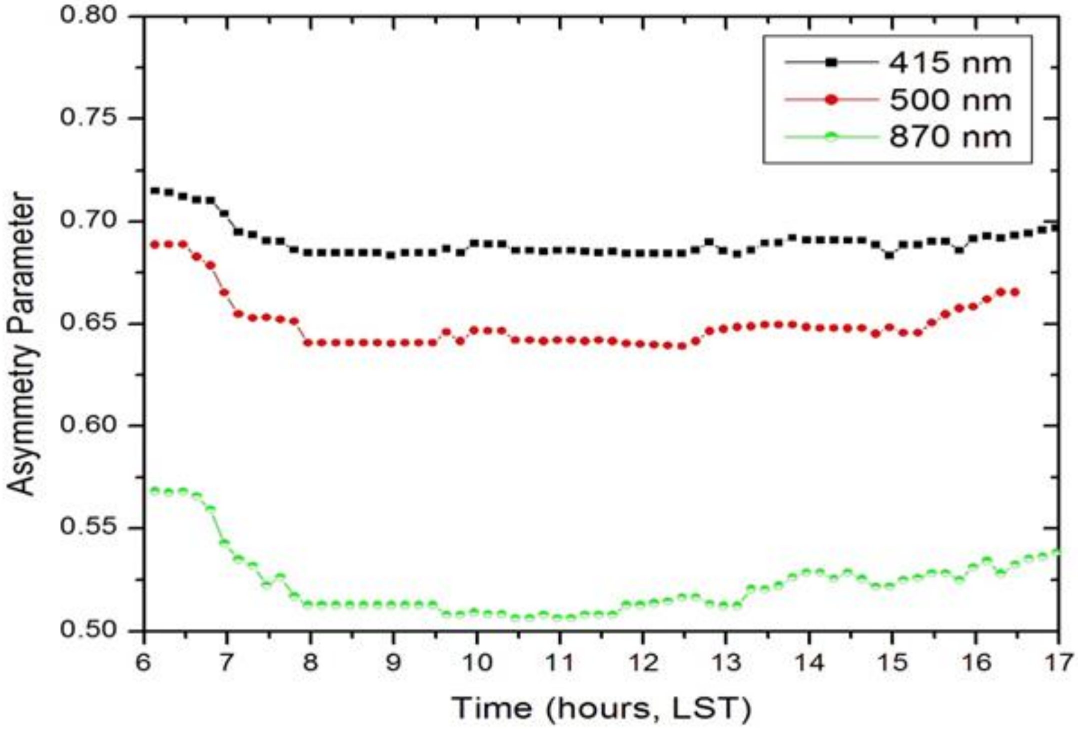

Figure 5.7 The asymmetry parameter for different channels (415, 500 and 870 nm) during the Rim fire on 23 August, 2013 retrieved from the MFRSR measurements.

Fig. 5.8 shows the retrieved imaginary part of the refractive index (*RI*) values as a function of wavelength by using MFRSR and Cimel for August 23, 2013. The imaginary part of the refractive index decreases from 0.022 to 0.013 as wavelength increases from 415 nm to 870 nm (Fig.5.8). Similarly, by using the Cimel, the imaginary part of the refractive index decreases from 0.015 at 440 nm to 0.005 at 1020 nm. Fig. 5.9 shows that daily values of the wavelength dependence of the *RI* for the same smoky day. The *RI* values increase slightly during the morning rush hour due to emission of BC from vehicles and decrease continuously to reaches minimum values at evening time. The average daily values of the *RI* (± standard deviation) for 415, 500 and 870 nm were 0.020±0.002, 0.014±0.002 and 0.011±0.002, respectively. The values of the *RI* are higher for shorter wavelengths than for the longer wavelengths for the smoke implying the enhanced light absorption by smoke at shorter wavelengths (Alam et al. 2012). The uncertainty in MFRSR or Cimel derived *RI* is about ± 0.004 (V Estelles, 2012).

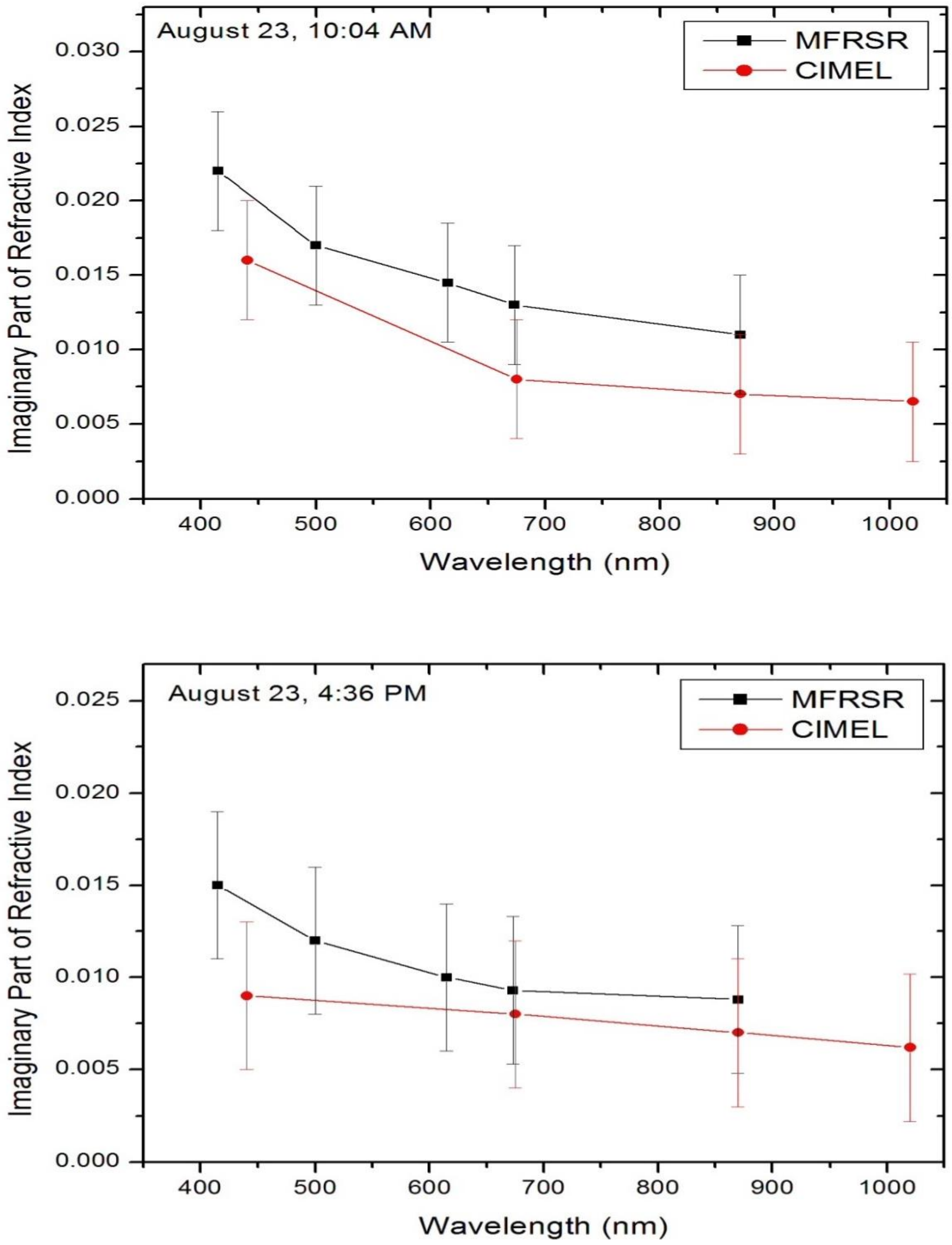

Figure 5.8 Variation of the imaginary part of refractive index with wavelength using MFRSR and Cimel during the Rim fire on August 23, 2013.

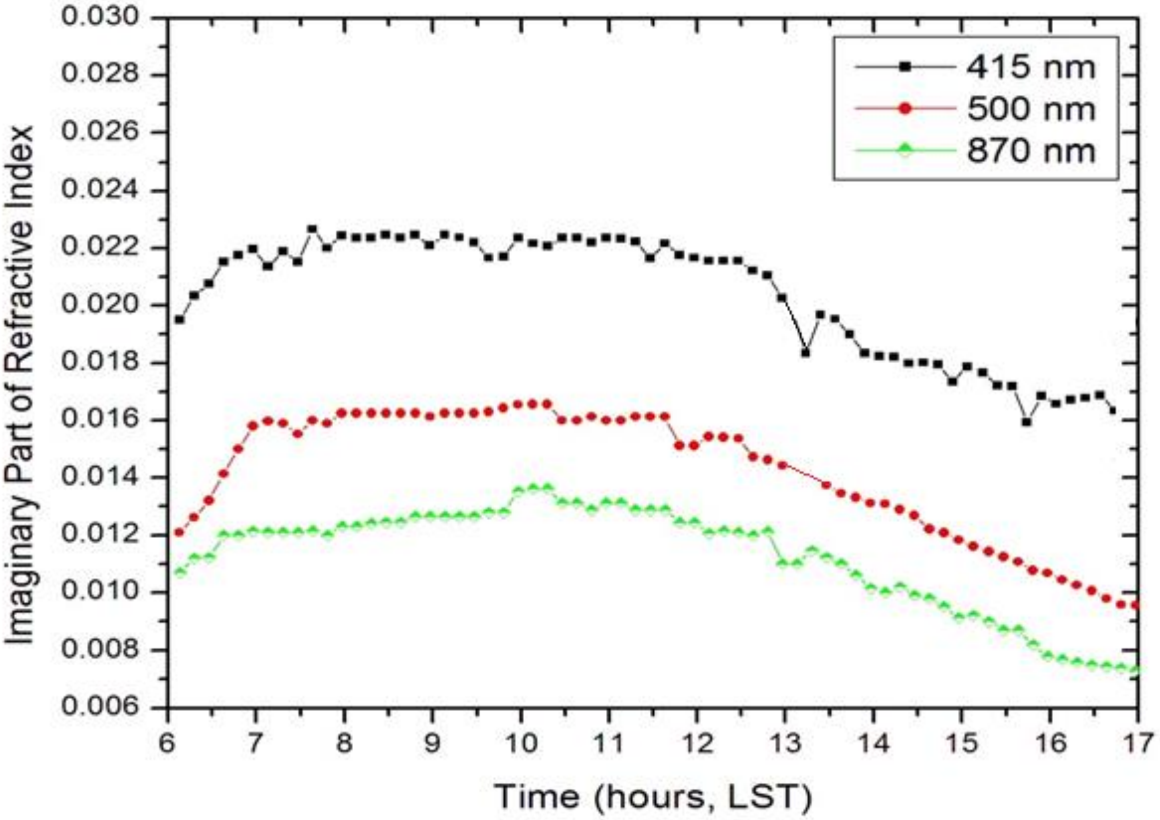

Figure 5.9 The imaginary part of the refractive index for different channels (415, 500 and 870 nm) during the Rim fire on August 23, 2013 using the MFRSR.

5.3 Dust Storm on April 24, 2013 in Reno

5.3.1 Solar Irradiance Measurements

For given aerosol properties, we can calculate the global, direct normal and diffuse irradiances by using the 2-stream radiative transfer model. The most important input variables for the 2-stream radiative transfer model are the wavelength dependent aerosol properties such as *AOD*, *SSA*, *ASY* and *RI*. Good agreement between the calculated and observed (MFRSR) radiative fluxes demonstrates that these input parameters, particularly the retrieved aerosol properties, are an appropriate representation of the atmospheric conditions (Ge et al. 2010).

The observed global, diffuse and direct normal irradiances at 500 nm are compared with model-simulated irradiances for April 24, 2013 during the dust storm are shown in Fig. 5.10. During the dust storm on April 24, at evening time, the diffuse irradiance increases and the direct normal irradiance decreases due to the scattering of the solar radiation by dust aerosol whereas the global irradiances were uniform. From MFRSR observed data for April 24, 2013, the maximum values of the diffuse irradiance at 500 nm was found to 0.34 $\mathrm{Wm^{-2}nm^{-1}}$. However, at the same time, the direct normal irradiance decreased to 1.18 $\mathrm{Wm^{-2}nm^{-1}}$ during the dust storm. The 2-stream radiative model calculations give the diffuse and direct normal irradiances as 0.35 and 1.17 $\mathrm{Wm^{-2}nm^{-1}}$, respectively (Figure 5.11). The percent difference between the MFRSR observed and 2-stream model (diffuse, normal direct and global irradiance) values are below 5%.

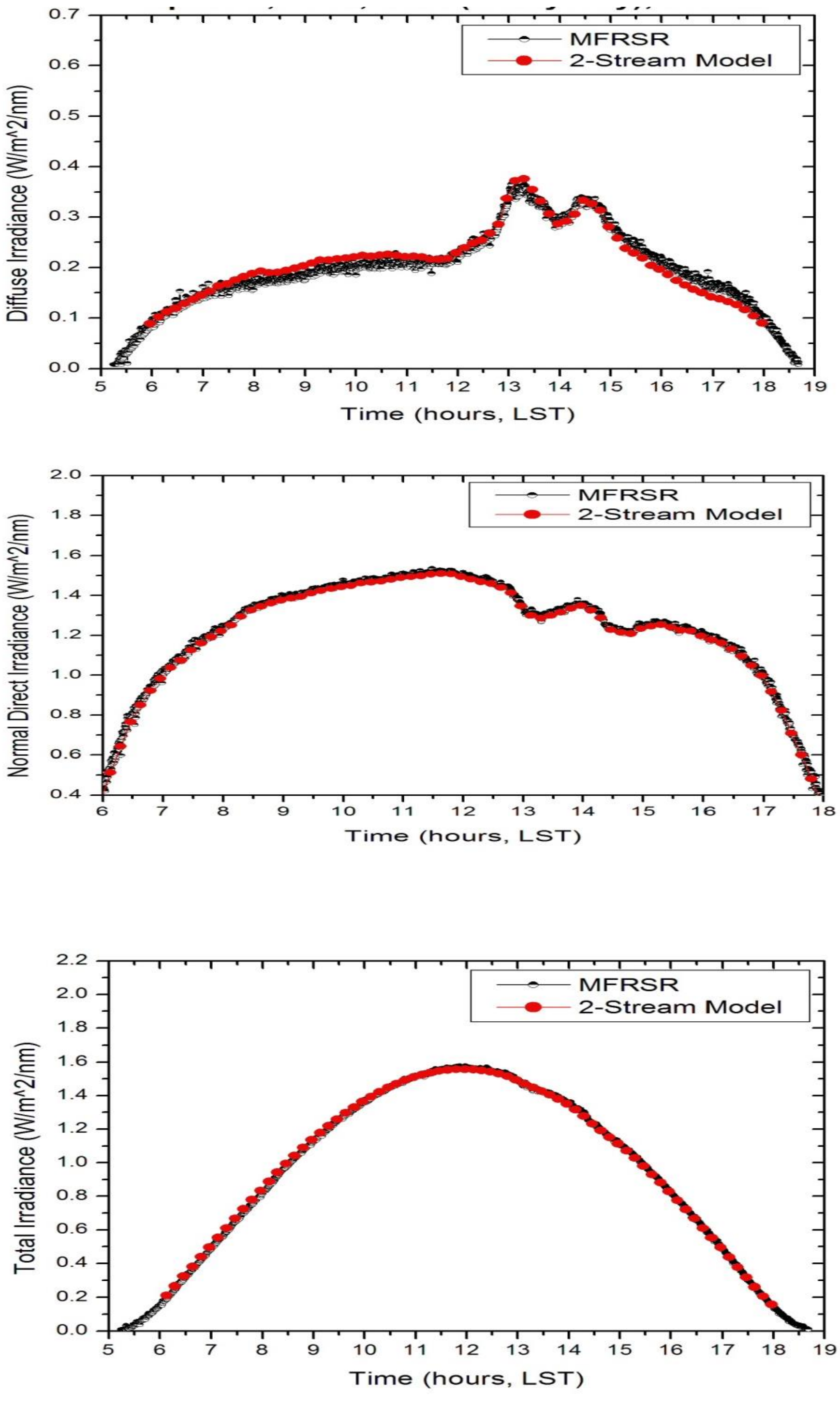

Figure 5.10 Diffuse irradiance (top), normal direct irradiance (middle) and total irradiance (bottom) for 500 nm during the dust storm on April 24, 2013 using MFRSR observed values and 2-stream model.

5.3.2 Single Scattering albedo (*SSA*)

The *SSA* in Reno increased with wavelength due to presence of the large dust particles on April 24, 2013 in evening time (Fig. 5.11). The *SSA* for dust increases with wavelength in the range of 300 nm to 1000 nm. This is because of significantly higher absorption in the UV and visible wavelengths (less than 600 nm), and lower absorption at longer solar wavelengths (675-1000 nm) (Bergstrom, Russell, and Hignett, 2002). The magnitude of the *SSA* in the wavelength range 415 to 870 nm varied between the values 0.88 to 0.94 at 1:15 PM local time and 0.86 to 0.93 at 2:30 PM local time for April 24, 2013 during the dust storm (Fig.5.11). The *SSA* increased rapidly with increasing wavelength, which reflected the dominance of scattering dust particles over the absorbing particles. For comparison, the values of *SSA* at 550 nm for Saharan dust was 0.88 (Hess at. el 1998) and 0.99 (Haywood et al. 2003).

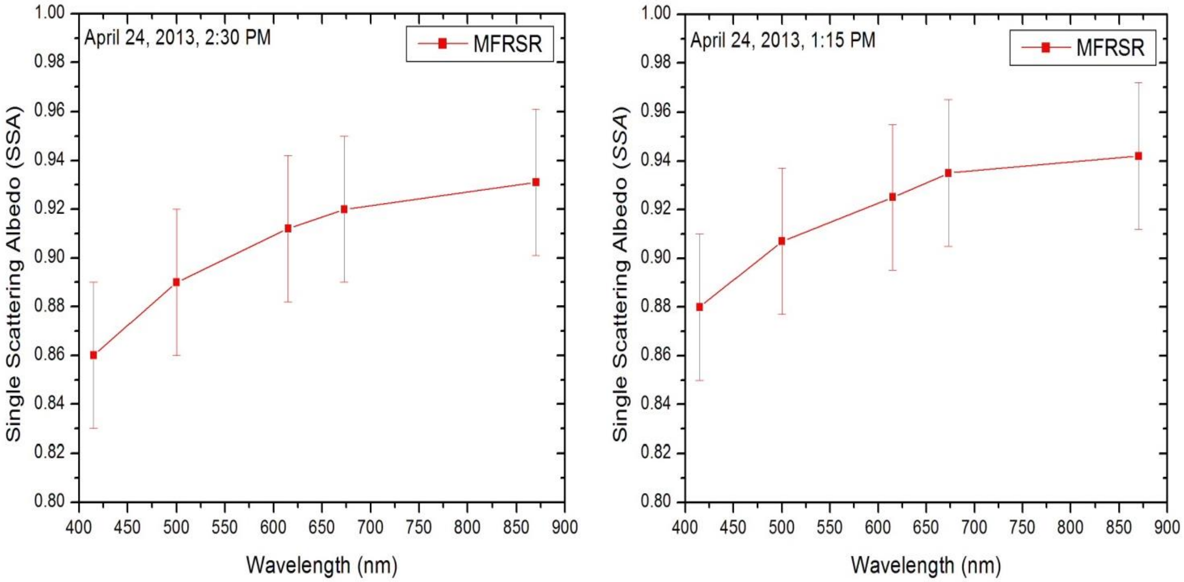

Figure 5.11 Variation of the *SSA* with wavelength using MFRSR during the dust storm on April 24, 2013**.**

5.3.3 Asymmetry parameter and imaginary part of refractive index

Fig. 5.12 shows the retrieved *ASY* values as a function of wavelength using MFRSR for April 24, 2013. The asymmetry parameter ranges from a maximum 0.74 at 415 nm to a minimum of 0.68 at 870 nm during dust aerosol loading at 1:15 PM. Fig. 5.13 shows the retrieved imaginary part of the refractive index values as a function of wavelength by using MFRSR for August 24, 2013. The imaginary part of the refractive index decreases from 0.019 to 0.01 as wavelength increases from 415 nm to 870 nm.

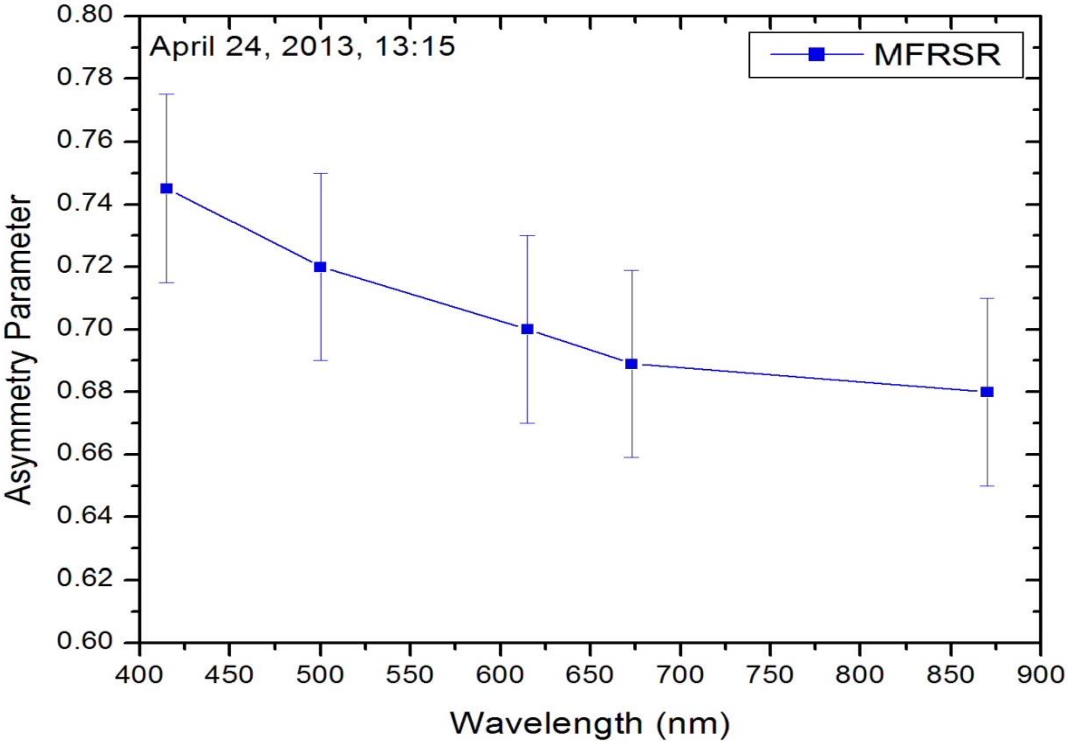

Figure 5.12 Variation of the asymmetry parameter with wavelength using MFRSR retrievals during the dust storm on April 24, 2013.

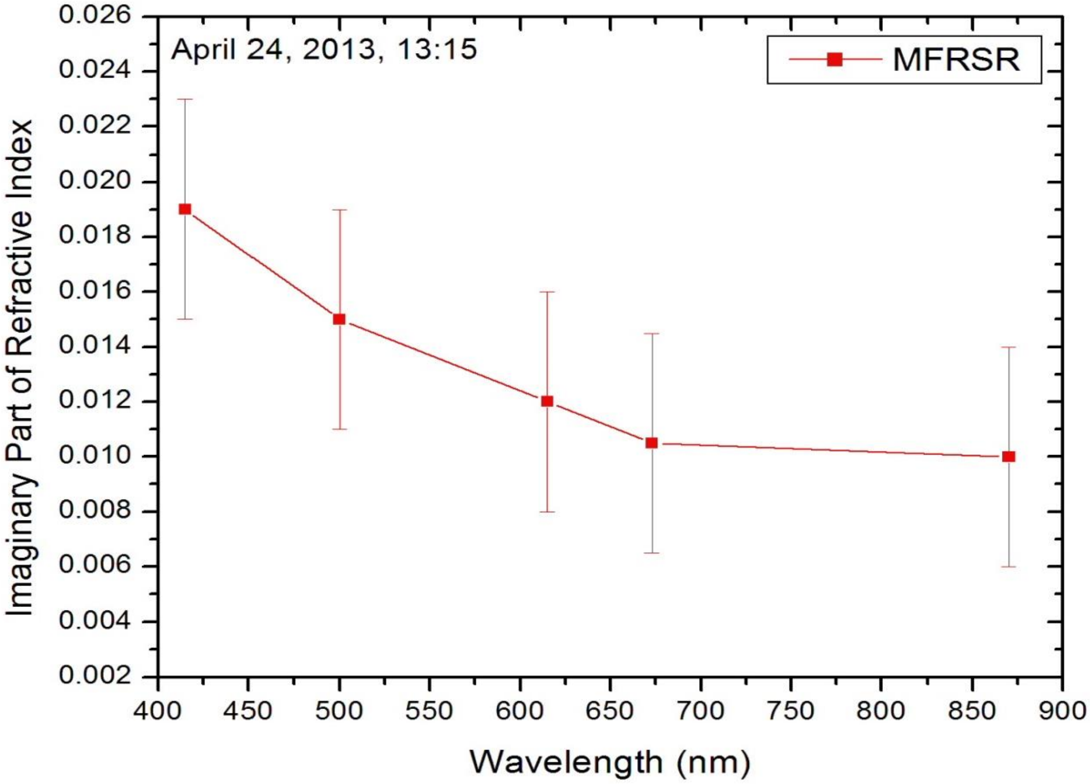

Figure 5.13 Variation of the imaginary part of refractive index with wavelength using MFRSR during the dust storm on April 24, 2013.

5.4 Clear Sky Days in Reno

5.4.1 Solar Irradiance Measurements

Solar radiation fluxes are often influenced by broken cloud fields, making it difficult to assess the direct aerosol radiative forcing (Queface, 2013). The radiative forcing by aerosols in the atmosphere can be better evaluated in the absence of clouds. Therefore correct identification of clear sky conditions is essential for studying aerosol radiative forcing and this exercise may need the use of multiple instruments (Antonio Joaquim Queface, 2013) . The daily time series of global and direct solar radiation measurements, obtained from MFRSR data and 2-stream radiative transfer model at UNR, allowed the identification of the probable clear sky days during the daytime. We select some of the clear sky days for our study of global, diffuse and direct normal irradiances using MFRSR observed values and provide comparisons with the values calculated by using the 2-stream model.

The upper panels of Fig. 5.14 show the global solar irradiances near 500 nm (10 nm bandwidth) measurement for both a cloudy and a clear sky day. A noisy time series curve was observed for a cloudy day on May 27, 2013; on the other hand, a smooth curve was found during the cloud-free (clear sky) day on August 1, 2013. On clear sky days, the reduction of solar radiation can be due to the presence of the aerosols and gas constituents of the atmosphere. The changes of solar radiation fluxes from one clear sky day to another can be mainly due to the changes on aerosol loading in the atmosphere. The lower panels of the Fig. 5.14 are the sky images corresponding to the observation during the cloudy and clear sky days.

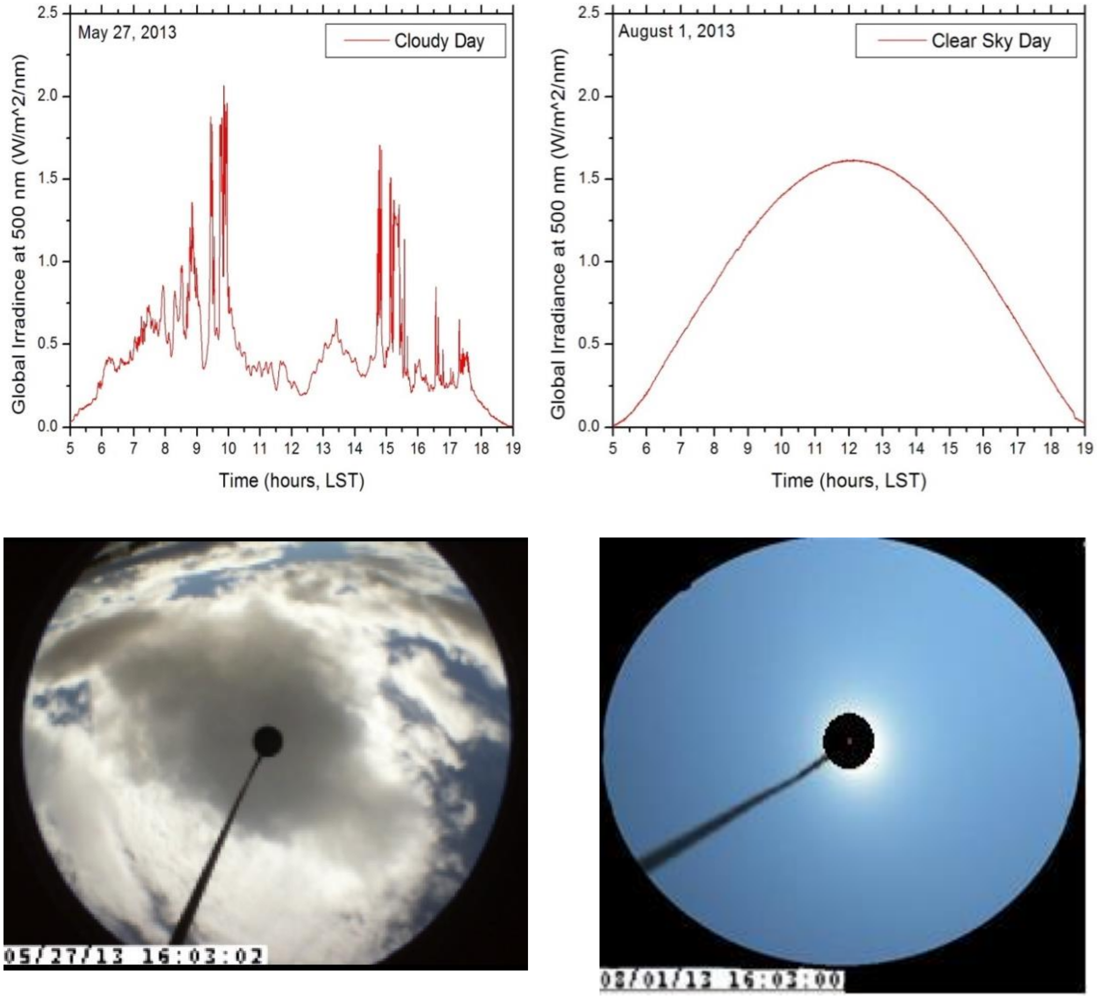

Figure 5.14 The global solar irradiances during the cloud on May 27, 2013 (left panel) and during the clear sky on August 1, 2013 (right panel).

For our study we select 12 clear sky days. Table 5.2 shows that the MFRSR measured global, diffuse and direct normal radiative fluxes at 500 nm for some selected clear sky days. Figs. 5.15 and 5.16 are time series of diffuse, direct normal and global solar irradiance measurements at wavelengths 500 nm and 870 nm taken at UNR during the clear sky on August 1, 2013. From MFRSR observed data for August 1, 2013, the maximum values of the diffuse, normal direct and global irradiances at 500 nm were found to be 0.15, 1.54 and 1.61 $\mathrm{Wm^{-2}nm^{-1}}$, respectively (Fig. 5.15). For 870 nm, the diffuse, direct normal and global irradiances were found to be 0.02, 0.88 and 0.84 $\mathrm{Wm^{-2}nm^{-1}}$, respectively (Fig. 5.16). The MFRSR observed values and 2-stream radiative transfer model values (diffuse, normal direct and global irradiance) are in good agreement for both wavelengths.

Date	**State of the Atmosphere**	**Maximum Diffuse Irradiance $\mathbf{Wm^{-2}nm^{-1}}$**	**Maximum Normal Direct Irradiance $\mathbf{Wm^{-2}nm^{-1}}$**	**Maximum Global Irradiance $\mathbf{Wm^{-2}nm^{-1}}$**
1 August	Low aerosol (clear sky)	0.15	1.54	1.61
2 August	Low aerosol (clear sky)	0.15	1.52	1.31
19 September	Low aerosol (clear sky)	0.15	1.52	1.33
20 September	Low aerosol (clear sky)	0.21	1.45	1.32
23 September	Low aerosol (clear sky)	0.155	1.52	1.31
4 October	Low aerosol (clear sky)	0.16	1.46	1.19
5 October	Low aerosol (clear sky)	0.15	1.47	1.20
15 October	Low aerosol (clear sky)	0.15	1.44	1.11
23 October	Low aerosol (clear sky)	0.17	1.39	1.03
25 October	Low aerosol (clear sky)	0.14	1.44	1.01
26 October	Low aerosol (clear sky)	0.155	1.41	1.00
27 October	Low aerosol (clear sky)	0.15	1.41	0.99

Table 5.2: Maximum diffuse, normal direct and total irradiances at 500 nm using MFRSR observed values during 12 selected clear sky days.

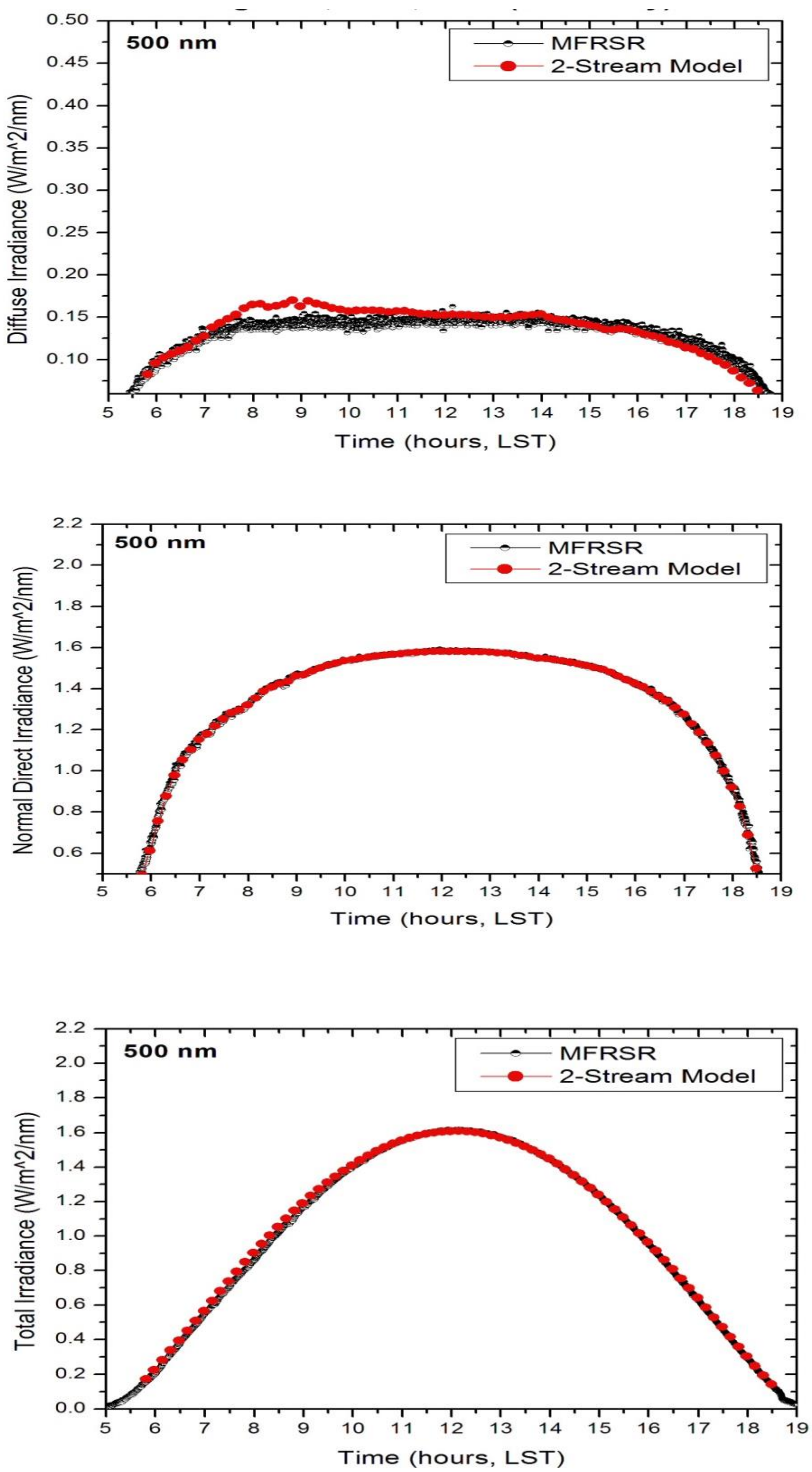

Figure 5.15 Diffuse irradiance (top), normal direct irradiance (middle) and total irradiance (bottom) for 500 nm during the clear sky on August 1, 2013 using MFRSR observed values and 2-stream model.

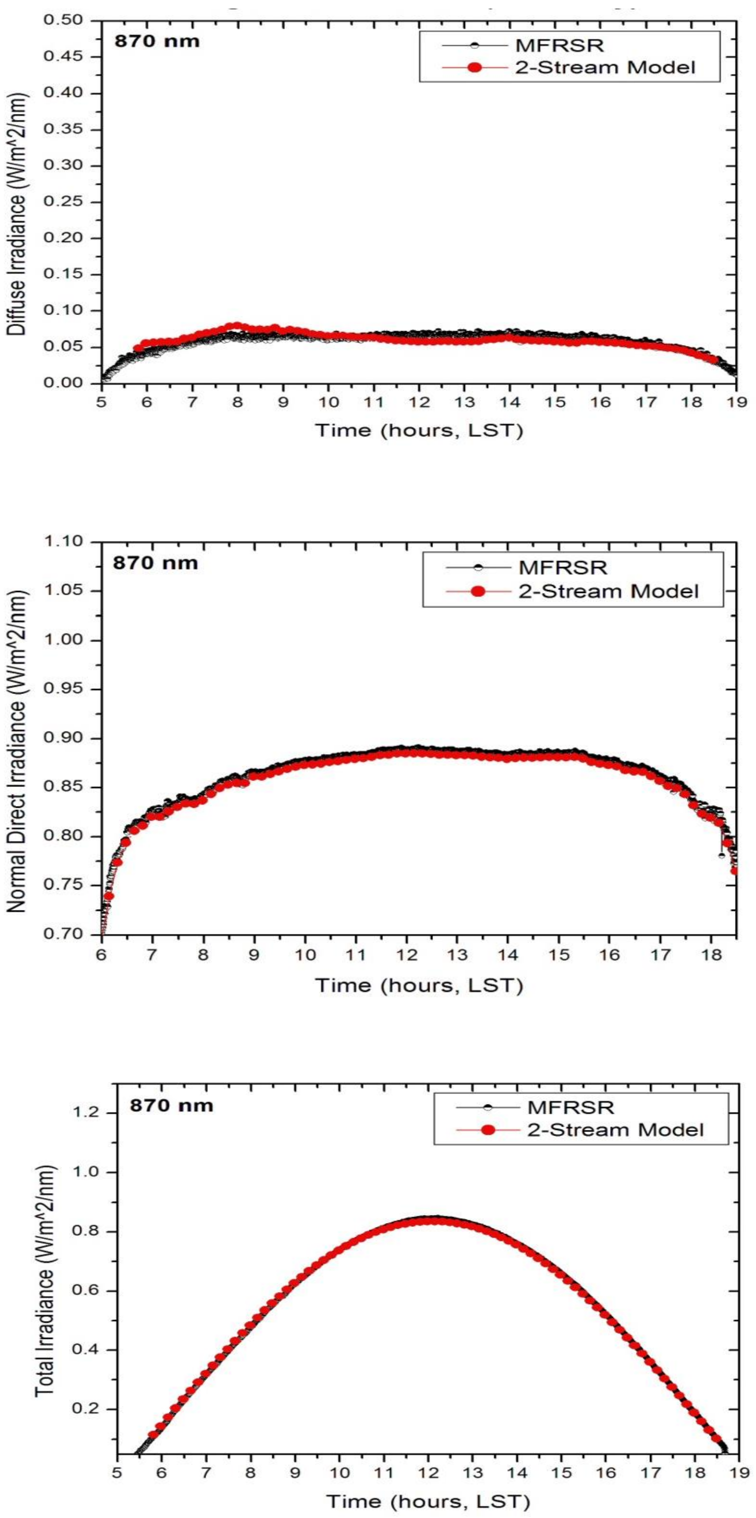

Figure 5.16 Diffuse irradiance (top), normal direct irradiance (middle) and total irradiance (bottom) for 870 nm during the clear sky on August 1, 2013 using MFRSR observed values and 2-stream model.

5.4.2 Single Scattering albedo (*SSA*)

The *SSA* values were obtained for the five wavelengths of the MFRSR for ten clear sky days from August 1 to October 25 of 2013. The value of *SSA* ranged from 0.73 - 0.94 at 415 nm, 0.69 - 0.92 at 500 nm, 0.66 - 0.91 at 615 nm, 0.65 - 0.89 at 675 nm, and 0.63 - 0.87 at 870 nm using MFRSR. Fig. 5.17 illustrates the comparison of *SSA* from MFRSR and Cimel for August 1, 2013 during a clear-sky day. It was found that the *SSA* for clear sky decreases with wavelength. The magnitude of the *SSA* in the wavelength range 415 to 870 nm varied between the values 0.92 to 0.84 at 9:15 AM local time by using MFRSR. Similarly by using Cimel, the retrieved *SSA* values were from 0.87 to 0.83 for increase in wavelength from 440 to 769 nm at 9:15 AM local time (Fig. 5.17).

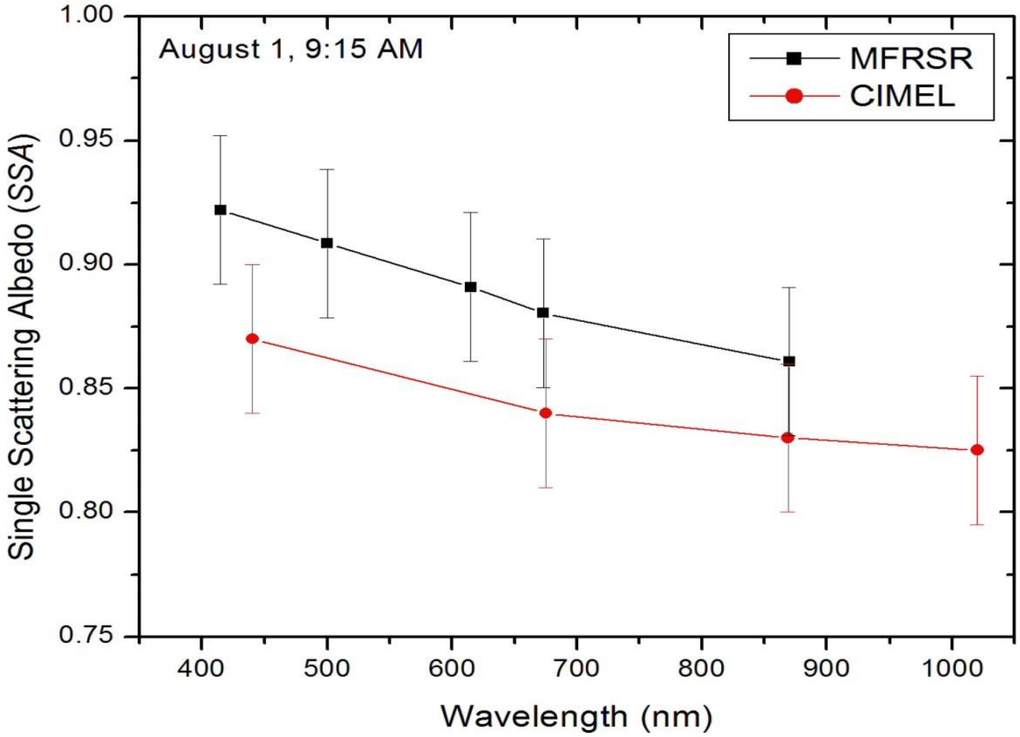

Figure 5.17 Variation of the SSA with wavelength using MFRSR and Cimel during the clear sky on August 1, 2013.

5.4.3 Asymmetry parameter and imaginary part of refractive index

Fig. 5.18 shows the *ASY* values as a function the wavelength using MFRSR and Cimel for August 1, 2013 during clear sky day. The *ASY* ranges from a maximum 0.64 at 415 nm to a minimum of 0.61 at 870 nm at 9:15 AM local time by using MFRSR. Also by using Cimel, the *ASY* varies from a maximum 0.68 at 440 nm to a minimum 0.66 at 869 nm at 9:15 AM local time on same day. The uncertainty of retrieved values of the *SSA* and *ASY* using MFRSR or Cimel is about ± 0.03 (Kassianov et al. 2007).

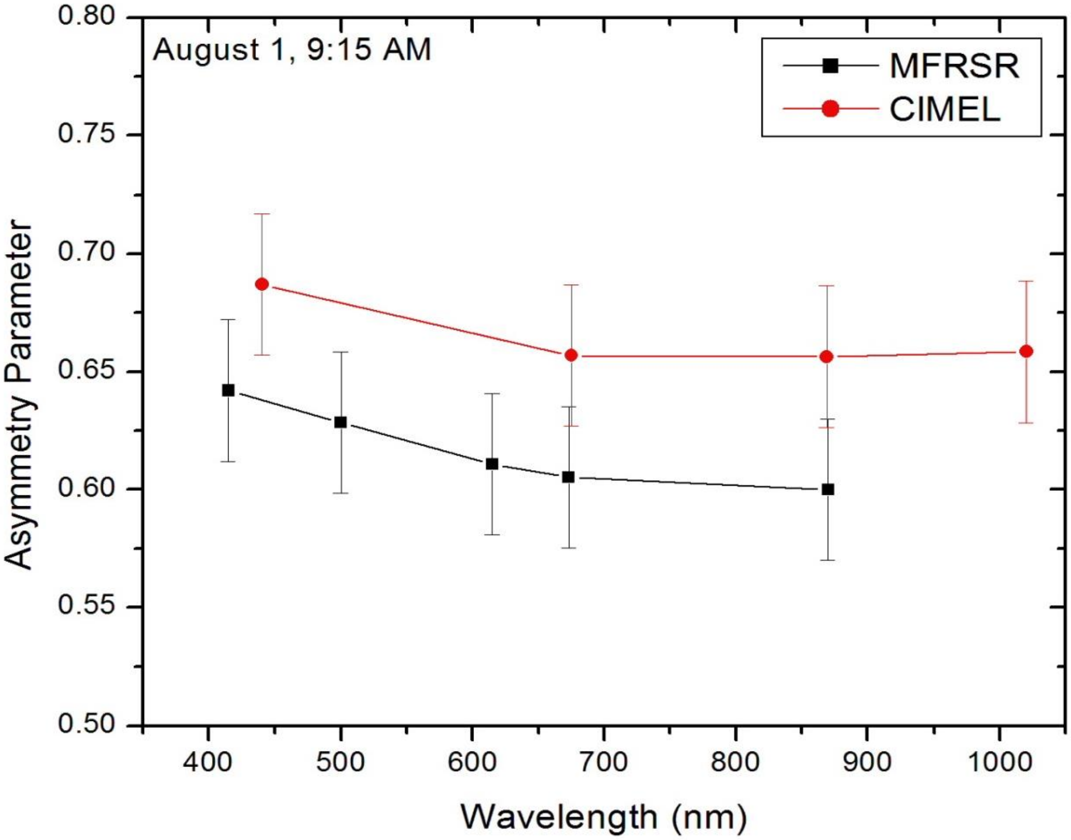

Figure 5.18 Variation of the asymmetry parameter with wavelength using MFRSR and Cimel during the clear sky on August 1, 2013.

Fig. 5.19 shows the retrieved *RI* values as a function of wavelength by using MFRSR and Cimel for August 1, 2013. The *RI* varies from 0.008 to 0.007 as wavelength increases from 415 nm to 870 nm by using MFRSR. Similarly, by using the Cimel, the *RI* varies from 0.0039 at 440 nm to the 0.0040 at 1020 nm. The uncertainty in *RI* measured by using MFRSR or Cimel is about ± 0.004 (V Estelles, 2012).

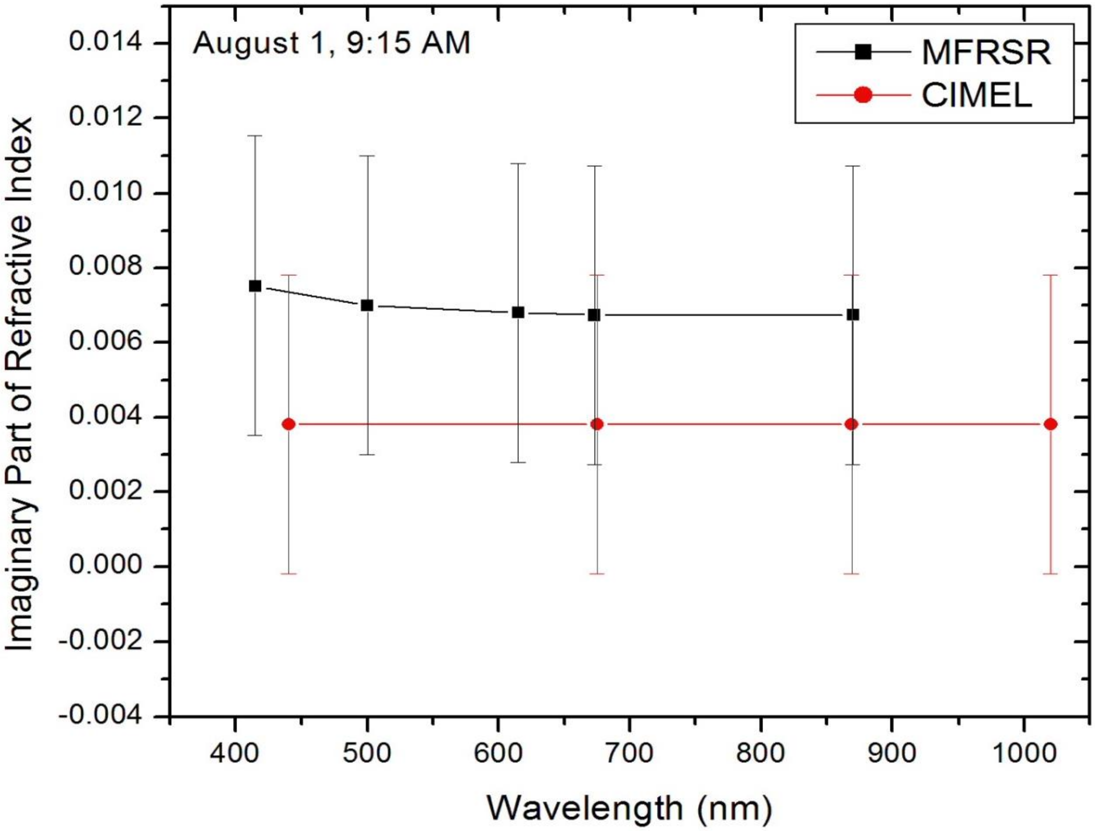

Figure 5.19 Variation of the imaginary part of refractive index with wavelength using MFRSR and Cimel during the clear sky on August 1, 2013.

5.5 Aerosol Radiative Forcing Comparison

The top of the atmosphere aerosol radiative forcing (*ARF*) is defined as the difference between the net (i.e. incoming – outgoing) atmospheric radiative fluxes when aerosols are present and when they are absent (Vogelmann et al. 2003). The total *ARF* can be broken down into the direct effect and indirect effect. The direct effect is due to the actual interactions of the aerosols with solar radiation and the indirect effect is due to the aerosol induced changes in the radiative properties of clouds. For the purpose of this study, the direct effect will be the focus for analysis of the radiative forcing. The scattering of the solar radiation may result in a cooling effect of the atmosphere called negative forcing. Absorption of solar radiation may lead to warming the atmosphere, called positive forcing. This heating and cooling of the atmosphere due to radiative forcing directly effects the monsoon circulation (Prasad et al. 2007). Since the optical properties play an important role in determining the radiative forcing of the atmosphere. In modeling of aerosol effects on atmospheric radiation, the following aerosol optical properties like *AOD*, *SSA*, *ASY* and surface-albedo are important input parameters. In this work, the *AOD*, *SSA*, *ASY* values were obtained from MFRSR and AERONET site that and surface albedo value is taken to be 0.08 for 550 nm wavelength.

The radiative forcing at the top of the atmosphere (*TOA*) has been estimated during the California Rim fire 2013. We used Eq. 3.47 from chapter 3 to calculate radiative forcing. Fig. 5.20 shows that the variation of the radiative forcing at the *TOA* by using MFRSR and Cimel retrieved aerosol optical properties for August 23, 2013. The plot indicates that the aerosol radiative forcing at TOA varies between $-38\ \mathrm{W/m^2}$ to $-65\ \mathrm{W/m^2}$ by using MFRSR data. These values are comparable with the radiative forcing values derived from the

Cimel. By comparison, the radiative forcing by all CO_2 is about 20 $\mathrm{W/m^2}$ and CO_2 increased since the industrial revolution is about 1.5 $\mathrm{W/m^2}$ (Forster et al. 2007).

Fig. 5.21 is the MFRSR retrieved aerosol radiative forcing during the desert dust on April 24, 2013. The radiative forcing at TOA ranges between $-2.0\ \mathrm{W/m^2}$ to $-4.5\ \mathrm{W/m^2}$ during the dust storm. Fig. 5.22 is the comparison of the MFRSR and Cimel retrieved aerosol radiative forcing during the clear sky on August 1, 2013. The radiative forcing at TOA ranges between $-0.45\ \mathrm{W/m^2}$ to $-1.75\ \mathrm{W/m^2}$ by using MFRSR. From these three plots, it is clear that the highest negative values of direct aerosol radiative forcing were observed during the peak of the biomass burning period during the Rim fire and lowest negative values were observed during the clear sky period.

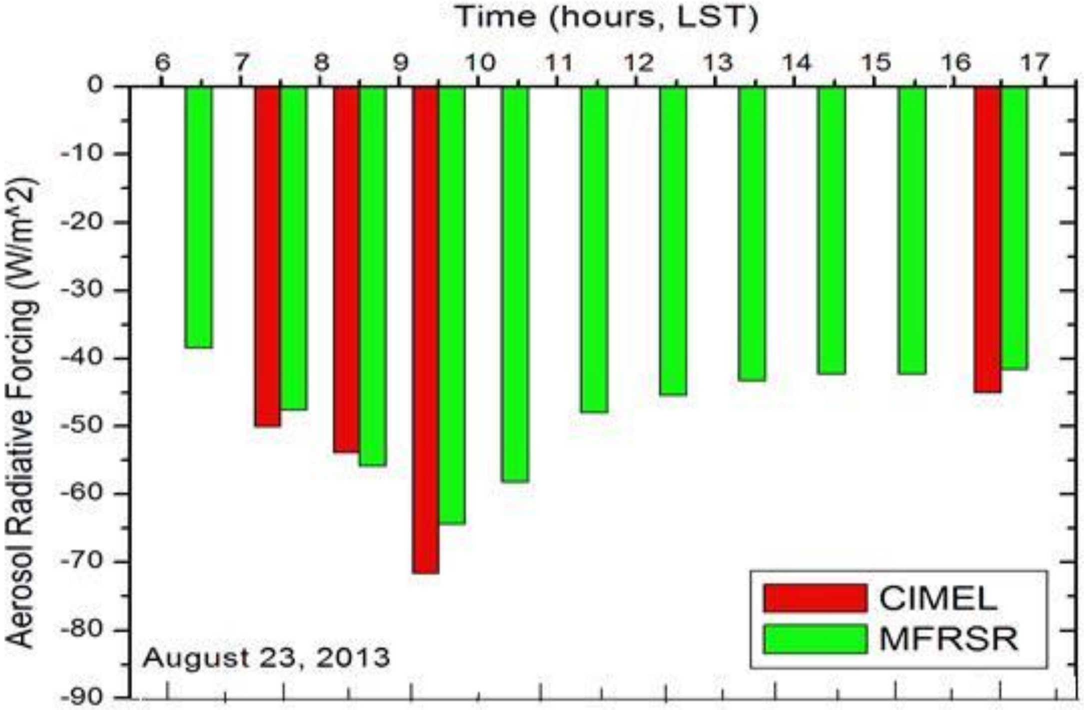

Figure 5.20 The aerosol radiative forcing at top of atmosphere during the Rim fire on August 23, 2013.

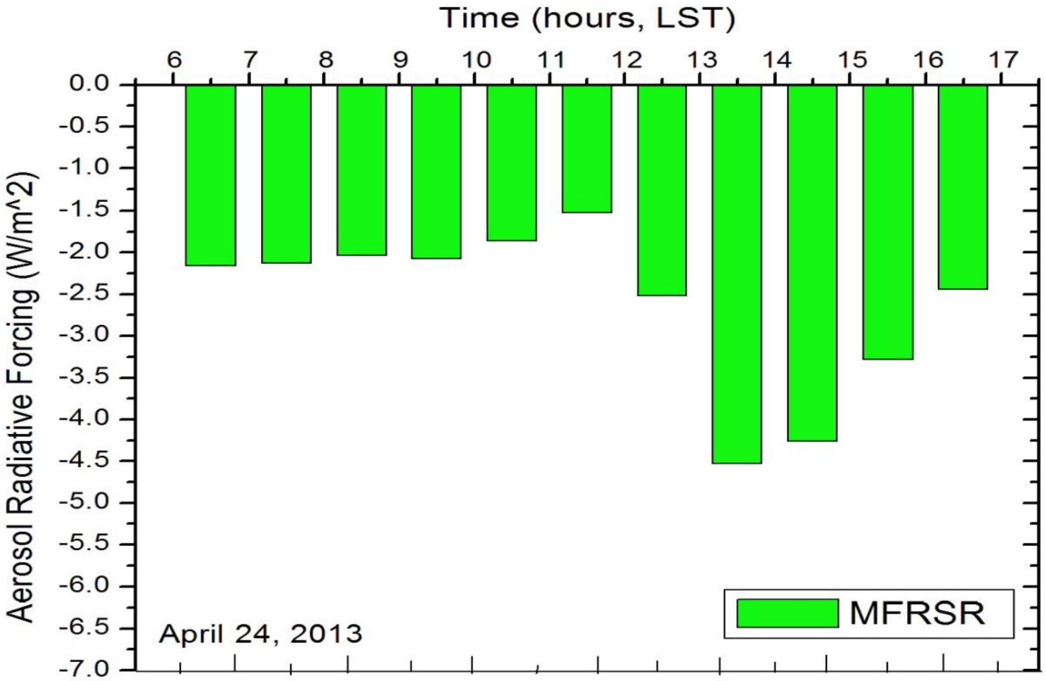

Figure 5.21 The aerosol radiative forcing at top of atmosphere during the Dust storm on April 24, 2013.

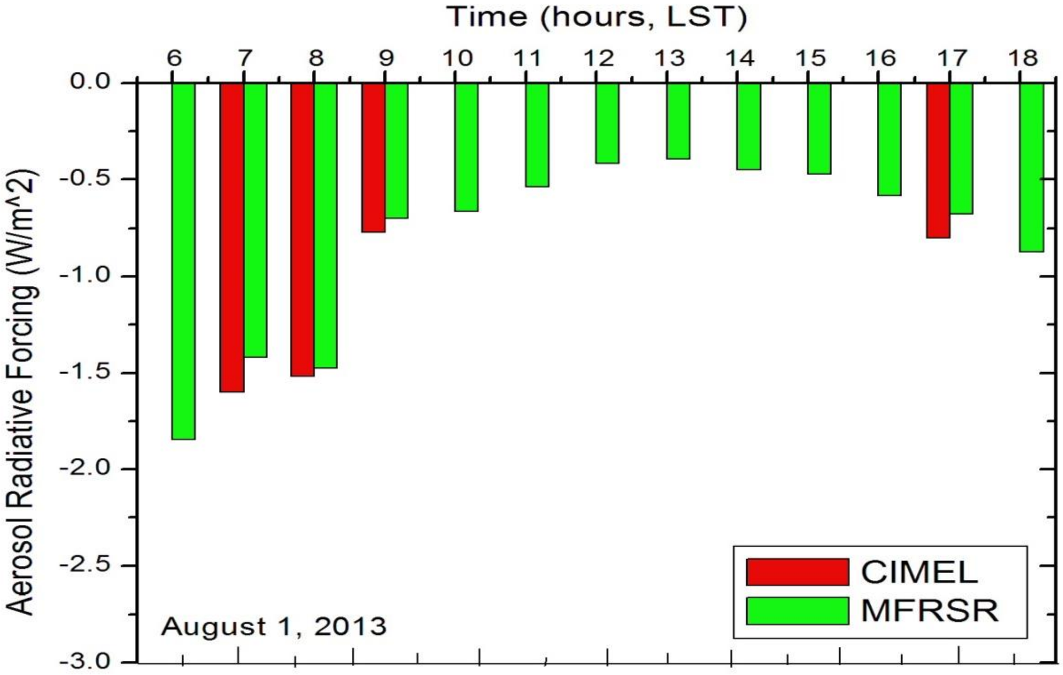

Figure 5.22 The aerosol radiative forcing at top of atmosphere during the clear sky on August 1, 2013.

5.6 References for Chapter 5

Alam, Khan, Thomas Trautmann, Thomas Blaschke, and Hussain Majid. 2012. “Aerosol Optical and Radiative Properties during Summer and Winter Seasons over Lahore and Karachi.” *Atmospheric Environment* 50 (April): 234–45. doi:10.1016/j.atmosenv.2011.12.027.

Bergstrom, Robert W., Philip B. Russell, and Phillip Hignett. 2002. “Wavelength Dependence of the Absorption of Black Carbon Particles: Predictions and Results from the TARFOX Experiment and Implications for the Aerosol Single Scattering Albedo.” *Journal of the Atmospheric Sciences* 59 (3): 567–77. doi:10.1175/1520-0469(2002)059<0567:WDOTAO>2.0.CO;2.

Dickerson, R. R., S. Kondragunta, G. Stenchikov, K. L. Civerolo, B. G. Doddridge, and B. N. Holben. 1997. “The Impact of Aerosols on Solar Ultraviolet Radiation and Photochemical Smog.” *Science* 278 (5339): 827–30. doi:10.1126/science.278.5339.827.

Dubovik, Oleg, Brent Holben, Thomas F. Eck, Alexander Smirnov, Yoram J. Kaufman, Michael D. King, Didier Tanré, and Ilya Slutsker. 2002. “Variability of Absorption and Optical Properties of Key Aerosol Types Observed in Worldwide Locations.” *Journal of the Atmospheric Sciences* 59 (3): 590–608. doi:10.1175/1520-0469(2002)059<0590:VOAAOP>2.0.CO;2.

Eck, T. F., B. N. Holben, D. E. Ward, O. Dubovik, J. S. Reid, A. Smirnov, M. M. Mukelabai, N. C. Hsu, N. T. O’Neill, and I. Slutsker. 2001. “Characterization of the Optical Properties of Biomass Burning Aerosols in Zambia during the 1997 ZIBBEE Field Campaign.” *Journal of Geophysical Research: Atmospheres* 106 (D4): 3425–48. doi:10.1029/2000JD900555.

Forster, Piers, Venkatachalam Ramaswamy, Paulo Artaxo, Terje Berntsen, Richard Betts, David W. Fahey, James Haywood, et al. 2007. “Changes in Atmospheric Constituents and in Radiative Forcing.” In *Climate Change 2007: The Physical Science Basis. Contribution of Working Group I to the 4th Assessment Report of the Intergovernmental Panel on Climate Change*, edited by S. Solomon, D. Qin, M. Manning, Z. Chen, M. Marquis, K. B. Averyt, M. Tignor, and H. L. Miller. Cambridge University Press, Cambridge, United Kingdom and New York, USA. http://elib.dlr.de/51416/.

Ge, J. M., J. Su, T. P. Ackerman, Q. Fu, J. P. Huang, and J. S. Shi. 2010. “Dust Aerosol Optical Properties Retrieval and Radiative Forcing over Northwestern China during the 2008 China-U.S. Joint Field Experiment.” *Journal of Geophysical Research: Atmospheres* 115 (D7): n/a–n/a. doi:10.1029/2009JD013263.

Gómez-Amo, J. L., V. Estellés, S. Segura, C. Marcos, A. R. Esteve, R. Pedrós, M. P. Utrillas, and J. A. Martínez-Lozano. 2013. “Analysis of a Strong Wildfire Event over Valencia (Spain) during Summer 2012 – Part 1: Aerosol Microphysics and Optical Properties.” *Atmos. Chem. Phys. Discuss.* 13 (8): 22639–85. doi:10.5194/acpd-13-22639-2013.

Gyawali, M., W. P. Arnott, K. Lewis, and H. Moosmüller. 2009. “In Situ Aerosol Optics in Reno, NV, USA during and after the Summer 2008 California Wildfires and the Influence of Absorbing and Non-Absorbing Organic Coatings on Spectral Light Absorption.” *Atmos. Chem. Phys.* 9 (20): 8007–15. doi:10.5194/acp-9-8007-2009.

Haywood, Jim, Pete Francis, Simon Osborne, Martin Glew, Norman Loeb, Eleanor Highwood, Didier Tanré, Gunnar Myhre, Paola Formenti, and Edwin Hirst. 2003. “Radiative Properties and Direct Radiative Effect of Saharan Dust Measured by the C-130 Aircraft during SHADE: 1. Solar Spectrum.” *Journal of Geophysical Research: Atmospheres* 108 (D18): n/a–n/a. doi:10.1029/2002JD002687.

Hess, M., P. Koepke, and I. Schult. 1998. “Optical Properties of Aerosols and Clouds: The Software Package OPAC.” *Bulletin of the American Meteorological Society* 79 (5): 831–44. doi:10.1175/1520-0477(1998)079<0831:OPOAAC>2.0.CO;2.

Jacobson, Mark Z. 2001. “Strong Radiative Heating due to the Mixing State of Black Carbon in Atmospheric Aerosols.” *Nature* 409 (6821): 695–97. doi:10.1038/35055518.

Kassianov, E. I., C. J. Flynn, T. P. Ackerman, and J. C. Barnard. 2007. “Aerosol Single-Scattering Albedo and Asymmetry Parameter from MFRSR Observations during the ARM Aerosol IOP 2003.” *Atmospheric Chemistry & Physics* 7 (June): 3341–51.

Kaufman, Y. J., D. Tanré, H. R. Gordon, T. Nakajima, J. Lenoble, R. Frouin, H. Grassl, B. M. Herman, M. D. King, and P. M. Teillet. 1997. “Passive Remote Sensing of Tropospheric Aerosol and Atmospheric Correction for the Aerosol Effect.” *Journal of Geophysical Research: Atmospheres* 102 (D14): 16815–30. doi:10.1029/97JD01496.

More, Sanjay. 2013. “Comparison of Aerosol Products Retrieved from AERONET, MICROTOPS and MODIS over a Tropical Urban City, Pune, India.” *Aerosol and Air Quality Research*. doi:10.4209/aaqr.2012.04.0102. http://www.aaqr.org/Doi.php?id=11_AAQR-12-04-OA-0102.

Prasad, A, S Singh, S Chauhan, M Srivastava, R Singh, and R Singh. 2007. “Aerosol Radiative Forcing over the Indo-Gangetic Plains during Major Dust Storms.” *Atmospheric Environment* 41 (29): 6289–6301. doi:10.1016/j.atmosenv.2007.03.060.

Queface, Antonio Joaquim. 2013. “Direct Radiative Forcing by Aerosols over Southern Africa”. Thesis. http://wiredspace.wits.ac.za/handle/10539/13007.

V Estelles, Monica Campanelli. 2012. “Comparison of AERONET and SKYRAD4.2 Inversion Products Retrieved from a Cimel CE318 Sunphotometer.” *Atmospheric Measurement Techniques*, 569–79. doi:10.5194/amt-5-569-2012.

Vogelmann, Andrew M. 2003. “Observations of Large Aerosol Infrared Forcing at the Surface.” *Geophysical Research Letters* 30 (12). doi:10.1029/2002GL016829. http://adsabs.harvard.edu/abs/2003GeoRL..30.1655V.

Chapter 6 Summary, Conclusion and Future Work

6.1 Summary and Conclusion

Successful ground-based (MFRSR and Cimel) and satellite (MODIS and Deep Blue) measurements are used for monitoring and characterization of the aerosol in the atmosphere. The optical and physical properties of aerosols were measured during various cloud free days at UNR. The measurements were made by using MFRSR, Cimel and satellite results have been presented in this dissertation. The observation periods include the major Rim fire smoke period of summer 2013 (August-September), a dust storm in Reno on 24 April, 2013 and some selected clear sky (May-October) days in Reno.

The *AOD*s were determined from measurements with the MFRSR at various wavelengths, and the Ångström coefficients (*AE)* were calculated. These results were compared with *AOD*s determined from a co-located Cimel sun photometer and satellite measurements. During Rim fire of August 2013, the MFRSR and Cimel *AOD*s derived at different wavelengths were very large compared with the *AOD*s found in other normal days. The values of *AOD* at 500 nm remained larger than 1 during the most intense period of the Rim fire event, and reached an extremely unusual maximum of 5 on 27 August. The *AE* values increased up to 2.5 due to the smoke particles. During the dust storm in Reno on April 24, the *AOD* at 500 nm increased to 0.2 that was 10 times higher than that we had in clear sky day (August 1, 2013). However the values of *AE* decreased to 0.2 due to dust in atmosphere, which was lower than that we found in other clear sky days.

Our MFRSR *AOD* retrievals agree well with Cimel *AOD* retrievals but the satellite aerosol retrievals are complicated by the fact that the upward radiance received by the satellite is composed of light scattered by the surface as well as atmospheric constituents, such as molecules and particles. Accurate satellite determination of *AOD* requires separation of radiation reflected by the surface from the total radiation (scattered from the surface and atmospheric constituents). This procedure is very difficult over land because land surface reflectances vary with location and time. The relative error between MFRSR and MODIS (Terra and Aqua) dark-target *AOD*s are found to be very high over Reno during the Rim fire and dust storm. The MODIS Deep Blue retrieved product performs better for Reno; the relative error between MFRSR and Deep Blue AODs are below 25% during the Rim fire and dusty day. Thus one outcome of this dissertation is to point out continued need for improvement of satellite retrievals of *AOD*.

The size distribution of aerosols is one of the most important parameters for characterizing the behavior of aerosols. The bimodal algorithm was used for the volume size distribution. The size distribution measurements showed that volume concentrations increased significantly during the Rim fire. Aerosol concentrations derived from aerosol size distributions showed that particle numbers were larger on smoky, rather than other normal days, and had a narrower size distribution. Smoke particles drastically enhanced the volume concentration of the fine mode (diameter less than 1 μm) particles. Our measurements showed that fine mode particles dominated over the coarse mode (diameter greater than 1 μm) particles by about 10:1 during the Rim fire. However, during the dust storm, the volume size distribution of the fine mode concentration is constant, while the coarse fraction changes significantly. The percentage of the coarse mode aerosols increased such that coarse mode dominated over the fine mode by about 3:1 in April 24, 2013. In contrast, there is no clear domination of either fine mode or coarse mode particles in the atmosphere during clear-sky days. The aerosol volume size distribution attained lower values for both fine and coarse mode, due to low aerosol loading during clear sky days.

From the HYSPLIT backward trajectories, it was demonstrated that a southerly wind brought the plumes of smoke, which originated at the California Rim fire toward Reno during the August-September, 2013. The back trajectories of the dust storm on April 24, 2013 demonstrated that winds carried the dust from the Humboldt sink towards Reno.

The optical properties such as *SSA* and *ASY* were determined from the combination of the aerosol size distribution retrieval and the Mie theory. A 2-stream radiation transfer model was used to calculate the retrieved values of the diffuse, direct and total irradiances. It was found that, the observed and retrieved values of the solar diffuse, direct and total irradiances agree with each other during the Rim fire, dust storm, and clear sky days. The *SSA*s that we retrieved from MFRSR and Cimel during the Rim fire were lower in comparison with the desert dust storm. The *SSA* decreased with the wavelength due to the absorption of the radiation by the small black carbon presence in the wild fire smoke. However, *SSA* increased with wavelength during the dust storm. This is because of significantly lower absorption of the dust aerosols at longer wavelengths (675-1020 nm) compared to biomass burning aerosols.

We also compared the *SSA* calculations from the photoacoustic instrument (PA) and MFRSR retrievals for smoky and clear sky days. The *SSA* obtained from the PA is more representative for the ground level air sample while those obtained from MSRSR are representative of the air above the instrument. It was interesting to note that the *SSA* values from PA measurements and from the MFRSR retrievals were close to the same value during the days of the Rim fire, suggesting that the smoke was well-mixed in the atmospheric boundary layer. However, on clear days, the *SSA* obtained from the MFRSR was considerably higher than that from PA implying a very different optical nature of the air close to the ground and the air above the surface.

It is notable that the *ASY* decreased with wavelength at 415-870 nm for MFRSR and 440-1020 nm for Cimel during our study (Rim fire, Dust storm and clear sky days). For smoke particles, the higher values of *ASY* at shorter wavelength suggested that more forward scattering by smoke aerosol that compared to longer wavelengths. The *ASY* of the dust was found to be larger than the smoke suggests that dust particles were significantly larger than smoke particles. The imaginary part of the *RI* decreased with increase in wavelength for Rim fire, desert dust storm and clear sky days as determined with both the MFRSR and Cimel. The higher *RI* values at shorter wavelength were associated with larger absorption of solar radiation at that wavelength range.

The aerosol properties such as *AOD*, *SSA*, *ASY* and surface albedo are all-important input parameters for the measurement of the radiative forcing. It was found that during the Rim fire, the radiative forcing at the top of the atmosphere (TOA) varied between $-38\ \mathrm{W/m^2}$ to $-65\ \mathrm{W/m^2}$ suggesting a cooling effect due to scattering of solar radiation by the high aerosol loading. The radiative forcing at TOA ranged between $-0.45\ \mathrm{W/m^2}$ to $-1.75\ \mathrm{W/m^2}$ during clear sky day on August 1, 2013 and between $-2.0\ \mathrm{W/m^2}$ to $-4.5\ \mathrm{W/m^2}$ during the dust storm on April 24, 2013. Agreement of the Cimel and MFRSR retrieved aerosol properties builds confidence in radiative forcing calculations based on experimental inputs.

6.2 Future Work

This dissertation presents the determination of aerosol properties such as *AOD*, aerosol particle size distribution, *SSA*, *ASY* and radiative forcing from the MFRSR, Cimel, and satellite measurements. However, knowledge of aerosol interactions in the atmosphere still remains fairly limited. As such, some suggestions for future work include:

- We can calculate the fine and coarse mode *AOD* values separately by using MFRSR data (Alexandrov 2005), similar to the analysis done with the Cimel data.
- Deep Blue retrieval algorithms are providing useful information about aerosol properties over bright-reflecting land surfaces (Hsu et al. 2013). However, retrieval algorithms for the bright surfaces, such as the Great Basin need improvement. Better treatment of such surface reflection need to be developed.
- The sensitivity of MFRSR retrievals to non-spherical particle scattering and absorption could be studied, especially for the case of dust particles.
- The vertical distribution of aerosol over Reno needs to be known to better understand the comparison of the in-situ and column measurements.
- Based on the single scattering approximation, we can estimate the phase function as a function of the scattering angle by using MFRSR data (Wang and Min 2008).
- The SBDART (Santa Barbara DISORT Atmospheric Radiative Transfer) multi-stream accurate radiative transfer model (Ricchiazzi et al. 1998) could be used to calculate the radiative forcing, instead of the 2-stream radiation transfer model (Liou, 2002).

6.3 References of Chapter 6

Alexandrov, Mikhail D. 2005. "Separation of Fine and Coarse Aerosol Modes in MFRSR Data Sets." *Journal of Geophysical Research* 110 (D13). doi:10.1029/2004JD005226. http://pubs.giss.nasa.gov/abs/al09200l.html.

Hsu, N. C., M.-J. Jeong, C. Bettenhausen, A. M. Sayer, R. Hansell, C. S. Seftor, J. Huang, and S.-C. Tsay. 2013. "Enhanced Deep Blue Aerosol Retrieval Algorithm: The Second Generation." *Journal of Geophysical Research: Atmospheres* 118 (16): 9296–9315. doi:10.1002/jgrd.50712.

Liou, Kuo-Nan. 2002. *An Introduction to Atmospheric Radiation*. Amsterdam; Boston: Academic Press.

Ricchiazzi, Paul, Shiren Yang, Catherine Gautier, and David Sowle. 1998. "SBDART: A Research and Teaching Software Tool for Plane-Parallel Radiative Transfer in the Earth's Atmosphere." *Bulletin of the American Meteorological Society* 79 (10): 2101–14. doi:10.1175/1520-0477(1998)079<2101:SARATS>2.0.CO;2.

Wang, Tianhe, and Qilong Min. 2008. "Retrieving Optical Depths of Optically Thin and Mixed-Phase Clouds from MFRSR Measurements." *Journal of Geophysical Research: Atmospheres* 113 (D19): D19203. doi:10.1029/2008JD009958.